Hans Rudolf

Increase of Information by Polarimetric Radar Systems

Foreword

Interdisciplinary cooperation of different scientific research domains spurs science and technology, bringing new features and visions in the 21st century. There are a number of candidates for this interdisciplinary science and research, f. e. microsystem engineering, nanotechnology, a.s.o. Another prime candidate are microwaves. Microwaves exhibit a good free space propagation, they are coherent, have a moderate wavelength and are easy to handle since supporting technology is ready available; even microminiaturized and highly integrated. The Ph. D. thesis of Hans Rudolf touches this interdisciplinarity by combining information from radar engineering, communications engineering, microwave measurement techniques and information processing. In a nearly unique manner it characterises the rationalisation of information content in areas where numerous data are fused. It demonstrates, that quite a lot of the information that is being processed is redundant. It also shows, in radar technology, how unique information can be identified and applied to extract otherwise hidden features. As for now, the handling of the type of equipment Hans Rudolf used, is not easy. Nevertheless it can be expected, that in the future trained versatile robots can be equipped with numerous sensors and configured to process information that is gathered to identify unique information. Such robots could then fulfil tasks in many disciplines ranging from medicine to space technology. I wish this thesis thorough distribution and a wide spread application of the recorded ideas.

Prof. Dr.-Ing. Werner Wiesbeck

- Institute Director -

Forschungsberichte aus dem
Institut für Höchstfrequenztechnik und Elektronik
der Universität Karlsruhe (TH)

Herausgeber: Prof. Dr.-Ing. Werner Wiesbeck

Band 1   Daniel Kähny
**Modellierung und meßtechnische Verifikation polarimetrischer, mono-
und bistatischer Radarsignaturen und deren Klassifizierung**

Band 2   Eberhardt Heidrich
**Theoretische und experimentelle Charakterisierung der polarimetri-
schen Strahlungs- und Streueigenschaften von Antennen**

Band 3   Thomas Kürner
**Charakterisierung digitaler Funksysteme mit einem breitbandigen
Wellenausbreitungsmodell**

Band 4   Jürgen Kehrbeck
**Mikrowellen-Doppler-Sensor zur Geschwindigkeits- und Wegmessung
- System-Modellierung und Verifikation**

Band 5   Christian Bornkessel
**Analyse und Optimierung der elektrodynamischen Eigenschaften von
EMV-Absorberkammern durch numerische Feldberechnung**

Band 6   Rainer Speck
**Hochempfindliche Impedanzmessungen an Supraleiter / Festelektro-
lyt-Kontakten**

Band 7   Edward Pillai
**Derivation of Equivalent Circuits for Multilayer PCB and Chip Package
Discontinuities Using Full Wave Models**

Band 8   Dieter J. Cichon
**Strahlenoptische Modellierung der Wellenausbreitung in urbanen Mi-
kro- und Pikofunkzellen**

Band 9   Gerd Gottwald
**Numerische Analyse konformer Streifenleitungsantennen in mehrlagi-
gen Zylindern mittels der Spektralbereichsmethode**

Band 10   Norbert Geng
**Modellierung der Ausbreitung elektromagnetischer Wellen in Funk-
systemen durch Lösung der parabolischen Approximation der Helm-
holtz-Gleichung**

Band 11   Torsten C. Becker
**Verfahren und Kriterien zur Planung von Gleichwellennetzen für den
Digitalen Hörrundfunk DAB (Digital Audio Broadcasting)**

Band 12   Friedhelm Rostan
**Dual polarisierte Microstrip-Patch-Arrays für zukünftige satelliten-
gestützte SAR-Systeme**

Forschungsberichte aus dem
Institut für Höchstfrequenztechnik und Elektronik
der Universität Karlsruhe (TH)

Increase of Information
by Polarimetric Radar Systems

Zur Erlangung des akademischen Grades eines

Doktor-Ingenieurs

von der Fakultät für
Elektrotechnik und Informationstechnik
der Universität Karlsruhe

genehmigte

Dissertation

von

Dipl.-Ing. Hans Rudolf
aus Bochum

Tag der mündlichen Prüfung: 8.11.1999
Hauptreferent: Prof. Dr.-Ing. Werner Wiesbeck
Korreferenten: Dr. rer. nat. habil. ing. Alois J. Sieber
                                     Prof. Dr.-Ing. Gerd Wanielik

to my parents

Acknowledgments

Zusammenfassung

Wachsende Anwendungsmöglichkeiten hatten im letzten Jahrzehnt einen starken Einfluß auf die Entwicklung polarimetrischer Radare. Während die Technologie heutzutage als ausgereift gelten darf, stellt die Datenauswertung potentielle Benutzer noch vor große Probleme. Insbesondere fehlt hier die Möglichkeit einer quantitativen Beschreibung der Information, die in polarimetrischen Radardaten enthalten ist. Dieser Mangel verhindert oft einen operationellen Einsatz polarimetrischer Radare und bereitet Probleme, die einer optimalen Datenauswertung im Wege stehen. Dies führt zu höheren Kosten in der Datenverarbeitung.

Mit der vorliegenden Arbeit wurde zum ersten Mal ein Konzept entwickelt, das es erlaubt, den Informationsgehalt polarimetrischer Radardaten zu quantifizieren. Dieses neuartige Konzept führt zu einem Maß, dem sogenannten *polarimetrischen Gewinn*. Der polarimetrische Gewinn bezieht die Information, die in polarimetrischen Radardaten enthalten ist, auf die Information, die mit einem konventionellen, d. h. einfach polarisiertem Radar gewonnen worden wäre.

Um die Signalverarbeitung, die zur Berechnung des polarimetrischen Gewinnes notwendig ist, zu optimieren, ist ein geometrischer Pfad entwickelt worden, der die Kohärenz zwischen den einzelnen Datenelemente maximiert.

Ein vollpolarimetrisches Radar ist entwickelt worden. Dieses Radargerät dient auch als Prototyp für verschiedene Innovationen, darunter eine zirkulare synthetische Apertur mit einem parallelogrammförmigen Arm. Diese erlaubt eine kosteneffiziente Realisierung dreidimensionaler Auflösung.

Das Konzept des polarimetrischen Gewinnes wird zuerst auf simulierte Daten kanonischer Ziele angewandt. Auch wird der Einfluß des Signal zu Rauschverhältnisses auf den polarimetrischen Gewinn untersucht. Daraufhin wird das Konzept auf Daten verschiedener Experimente angewandt. Diese Testexperimente beinhalten die Detektion von Antipersonenminen, SAR Interferometrie, hochauflösende dreidimensionale Daten einer Nordmanntanne sowie Daten von luft- und weltraumgestützten Systemen.

Sowohl die Simulationen als auch die Experimente bestätigen die Richtigkeit des Konzeptes. Die Ergebnisse unterstreichen auch die Möglichkeiten einer Integration von polarimetrischen Radardaten in data-mining Systeme,

da der polarimetrische Gewinn auch in umfangreichen Datensätzen erlaubt, Gebiete mit erhöhtem polarimetrischen Informationsgehalt hervorzuheben und die polarimetrische Signalverarbeitung auf diese Gebiete zu konzentrieren. Damit führt der polarimetrische Gewinn zu einer systematischen und optimisierten Auswertung der Information polarimetrischer Radardaten.

Executive Summary

Increasing fields of applications have given in the past decade a strong input on the development of polarimetric radar systems. Whereas the technology can be considered proven, the data extraction still causes problems to the user. A quantitative description of the information content in polarimetric radar data is missing. This lack inhibits an operational use of polarimetric radar and causes difficulties in an optimised extraction of the information, hence increasing the costs of data handling.

In this work has been developed for the first time a concept to quantify the information content of polarimetric radar data. This novel concept leads to a measure called *polarimetric gain*. The polarimetric gain relates the additional information obtained by a polarimetric radar to the information obtained by a conventional, single polarisation radar.

In order to optimise the signal processing, necessary for the calculation of the polarimetric gain, a geometrical path, optimising the coherence between the single data elements is presented.

A full polarimetric radar instrument has been developed. This radar serves also as prototype for several innovations, among them a circular synthetic aperture with a parallelogram shaped arm, allowing a cost effective implementation of 3-D capabilities.

The developed concept of the polarimetric gain is first applied to simulated data of canonical targets. The influence of the signal to noise ratio on the polarimetric gain is examined. Thereupon the concept is applied to real data arising from several experiments. These experiments comprise the detection of anti-personal landmines, SAR interferometry, high resolution three dimensional data on a fir-tree and finally space- and airborne data.

Both the simulations and the experiments confirm the validity of the concept. The results underline the possibility of integrating polarimetric radar data into sophisticated systems of data mining, as the polarimetric gain allows in extensive data sets to highlight regions of elevated polarimetric information content and to concentrate the polarimetric signal processing on these regions. The result is a systematic and optimised extraction of the information in full polarimetric radar data.

Contents

List of Figures

List of Tables

Chapter 1

Introduction

During the last decade, radar technology experienced a rapidly growing field of applications. These novel applications are no longer limited to military use or airtraffic-control. Civilian benefits of radar technology arise for instance in remote sensing.

In remote sensing of the Earth's environment, radar complements other sensors, to satisfy the increasing demand for monitoring global and local changes. A whole series of remote sensing satellites are now equipped with radar sensors and there are many more radar satellites to come, as radar offers certain advantages over competing technologies. The unique feature of radar is the ability to take radar images over virtually any region at any time, regardless of weather and sunlight conditions. Under certain conditions, radar waves can also see through vegetation, sea ice or dry sand, thus providing to scientists data of information otherwise inaccessible. One prerequisite to provide this information is the exploitation of the polarimetric properties of the radar waves [vZZ90]. Many of the upcoming satellite missions will therefore have a radar providing multi-polarisation data [Ros96].

Also in the field of humanitarian demining, the idea that radar technology is a valid method for improving the quality and clearing rate meets with universal approval [Sie95]. Again the exploitation of the polarimetric information within the radar signal can contribute to enhance the performance of such a radar, as effects like the Brewster-angle [GKV89] allow a better coupling of the radar system to the ground and the additional information allows a better classification of detected objects.

1.1   Problem Statement

These two potential applications of polarimetric radar are also exemplary for
the data handling problems, that arise when using polarimetric rather than
conventional single polarisation radar. While the technology for exploiting
different polarisations is familiar for a long time and calibration problems are
solved recently [vZ90, RW91, Fre92a, Fre92b] the extraction of the informa-
tion still causes major problems to the user. The following problems arise in
the extraction of information:

- Where does radar polarimetry yield additional information?

- Are there any areas of a particular polarimetric interest?

- How can the polarimetric information be described?

- Is it possible to implement polarimetric radar data in automated data
  extraction systems, like data mining?

A main source for these problems is the lack of a quantitative description
of the information in polarimetric radar data. This lack inhibits a devel-
opment of an operational system, be it for earth observation or demining,
where radar polarimetry can yield a higher grade of information.

A method, that establishes a quantitative measure of the polarimetric
information content in radar data, allows a fast scan of these data with
respect to polarimetric information before other information extraction takes
place. This data-scan results in a map of the data, where regions with a
significant polarimetric information content are highlighted. The successive
information extraction with algorithms based on polarimetric target features
[Kro93, CP97, CP98] can concentrate on these highlighted regions.

Thus, a systematic information extraction is established, and the spatial
information of polarimetric data can be extracted in an optimised way. The
user benefits from this approach not only in terms of an optimised usage of
the polarimetric information, but also in decreased costs of the data handling.

1.2   State of the Art

The increasingly important role polarimetric radar will play in the near future can be documented exemplary with the radar remote sensing satellites as shown in table 1.2.

Mission	Launch Date	Polarisation
Seasat	26. June 1978	hh
Almaz 1A	31. May 1991	hh
ERS-1	17. July 1991	vv
JERS-1	11. February 1992	hh
SIR-C	09. April 1994	hh, hv, vh, vv
	30. October 1994	(L and C-band)
X-SAR	09. April 1994	vv
	30. October 1994	
ERS-2	21. April 1995	vv
Radarsat	4. November 1995	hh
SRTM	11. February 2000	vv
Envisat	June 2001	hh, vv
ALOS	2002	hh,hv or vv,vh

Table 1.1: Polarisation of the radar sensor for past, present and future radar remote sensing satellites

Whereas early missions used only single polarisation radars, a clear trend towards multi-polarisation radars is recognisable. This trend is accompanied by a growing interest of the users of remote sensing information, as a high potential of polarimetric data has been recognised [RW89]. Applications where radar polarimetry has shown results are the mapping of forest growth and biomass [RS94, Dob95, Bea94], crop classification [AH95, DGdGLS94, FMY94], soil moisture measurements [Pri98] and derivation of snow and ice parameters [RNF95].

Despite these examples of a successful use of polarimetric information, many users of the data remain skeptical with regard to radar polarimetry [vdH57, NYKL92, Rud98]. A reason for this scepticism is the fact that the added polarimetric data have only yielded additional information in special cases[MT98].

For a systematic application of polarimetric radar data and the integra-
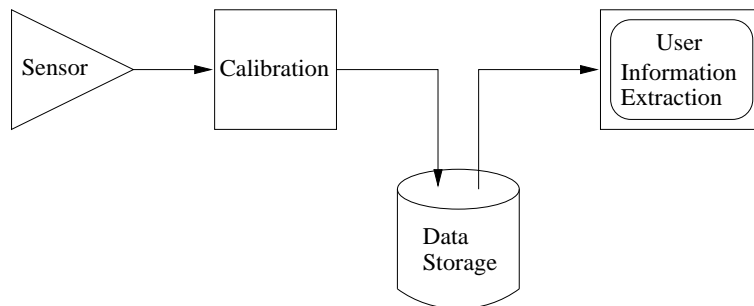
Figure 1.1: Traditional information extraction
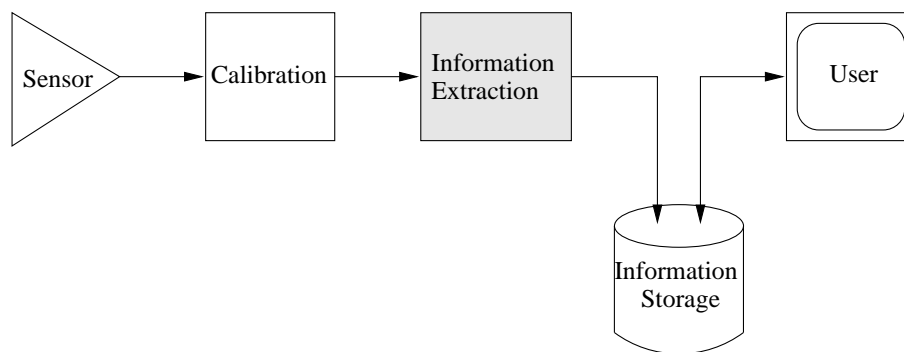
Figure 1.2: Information extraction with a data mining approach and the possibility to quantify the information

tion of such data in advanced information handling concepts, such as data mining, the premise is the existence of a measure of the information in polarimetric radar data. Only the existence of such a measure, and the automated calculation of it, allows an optimised extraction of the information. In contrast to the traditional information extraction approach, an approach where the user receives data and extracts the information, as shown in figure 1.1, the measure above mentioned allows an information extraction according to figure 1.2.

1.3   Outline

In this work a way to calculate the maximum obtainable information of given polarimetric data is developed. This will enable the user to see where or whether polarimetric data gives extra information and how many classes

might be distinguishable with classification of the data, resulting in a more time efficient analysis of the data and in more precise definitions for future sensors.

The solution of the problem described above incorporates three different subjects of electronic engineering. Chapter 2 summarises the basic definitions in electromagnetic wave theory, with a special emphasis on polarimetry, an overview of the required information theory and an introduction into radar systems.

In chapter 3, a concept for a measure of the polarimetric information content is developed. The entropy as a measure of information is applied to polarimetric radar. From the entropy flow, a comprehensive description of the information content in the polarimetric data is deduced. In order to express a relative rather than an absolute measure for the information, the polarimetric gain as a measure for the additional information that is obtained by using a full polarimetric radar instead of a single polarisation radar is introduced. As the developed method, as all methods based on statistics [Gne62, Woo75], is dependent on the way of the calculation of ensemble averages, an optimised scan path is presented. This Hilbert-scan path [Hil91] optimises the coherence of subsequent pixels. Based on this scan path, the concept of the polarimetric gain as defined before is extended towards a local polarimetric gain. This definition of a local polarimetric gain does not only allow an expression of an over-all usefulness of the polarimetric data, but gives the precise location where polarimetric data contains information.

As an increased noise level will increase the entropy, the influence of the signal to noise ratio on the polarimetríc gain is examined. Finally, the importance of a precise calibration for a maximised information content is underlined.

The concept of the polarimetric gain is applied in section 3.6 to various canonical targets. These targets comprise randomly distributed spheres, randomly oriented dihedrals and random scatterers.

In order to verify the concept of the polarimetric gain, a full polarimetric radar sensor has been developed. This sensor is presented in chapter 4. This radar sensor serves also as prototype for several innovations. These innovations comprise a circular synthetic aperture with a parallelogram shaped arm [Rud99b]. In combination with a second linear synthetic aperture, this en-

ables the performance of high resolution three-dimensional full polarimetric measurements.

Several validation experiments that are performed with this polarimetric radar sensor are shown in chapter 5. The scope of these experiments was to analyse how much additional information radar polarimetry yields. These experiments are chosen carefully in order to cover a wide variety of possible applications of polarimetric radar.

The first example is the detection of anti-personnel landmines. These data is analysed with regard to its polarimetric properties. The evaluation of the polarimetric gain for these data leads to an improved data-analysis.

The next experiment is the result of a demonstration experiment for ground based SAR interferometry [Tar99]. This data is chosen for the polarimetric analysis, though the emphasis for the experiment was clearly on interferometry and not on polarimetry. Thus it stands as an example of a target that is not suited for polarimetry. This is also verified by the use of the polarimetric gain.

A high resolution laboratory three-dimensional radar image of a fir tree is the next example. The high resolution of these data allows a very detailed analysis of the polarimetric behaviour of the target. The evaluation of the polarimetric gain reveals to be a fast method for detecting the distribution of polarimetric information for this target.

Data of the only available full polarimetric space-borne earth observation sensor (*SIR-C*) is analysed. The polarimetric gain and the upper limit of polarimetric distinguishable classes is derived. For comparison with traditional tools of polarimetric signal processing, decomposition algorithms [CP96] have been applied to the data. Finally, the concept is applied to high resolution airborne data, arising from DLR's *E-SAR* system. In these data is shown how the combination of high resolution and radar polarimetry can help to increase the information.

Chapter 2

Basic Definitions

2.1 Wave Equation and Polarisation

The mathematical basis of any electromagnetic scattering or transmission are the equations formulated by Maxwell [Max54]

$$\nabla \cdot \vec{D} = \rho \tag{2.1}$$

$$\nabla \times \vec{E} = -\frac{\partial}{\partial t}\vec{B} \tag{2.2}$$

$$\nabla \cdot \vec{B} = 0 \tag{2.3}$$

$$\nabla \times \vec{H} = \vec{J} + \frac{\partial}{\partial t}\vec{D} \tag{2.4}$$

which are completed by the law of the conservation of electric charges

$$\nabla \cdot \vec{J} + \frac{\partial}{\partial t}\rho = 0 \tag{2.5}$$

and the constitutive relations

$$\vec{D} = \varepsilon\vec{E} \tag{2.6}$$

$$\vec{B} = \mu\vec{H} \tag{2.7}$$

$$\vec{J} = \sigma\vec{E}. \tag{2.8}$$

For a homogeneous charge- and sourcefree medium these equations can be combined to a single equation, the wave equation [Sim89, Bal89]

$$\nabla^2\vec{E} + k^2\vec{E} = 0 \tag{2.9}$$

7

with

$$k = \omega\sqrt{\mu\varepsilon}. \tag{2.10}$$

One of the possible solutions for this equation is a transverse electromagnetic wave propagating into z-direction

$$\vec{E}(z) = \vec{E}_0 e^{-jkz} e^{j\omega t}, \tag{2.11}$$

where $z = h \times v$. In this equation the so called Jones-vector [Wan88, Pot95]

$$\vec{E}_0 = E_h \vec{h} + E_v \vec{v} \tag{2.12}$$

with

$$E_h = |E_h| e^{-j\varphi_h} \tag{2.13}$$

and

$$E_v = |E_v| e^{-j\varphi_v} \tag{2.14}$$

can still be chosen arbitrarily without questioning the solution of the equation [Stu93]. The Jones-vector describes the polarimetric character of a monochromatic transverse electromagnetic (TEM) wave. With its knowledge, it is possible to compute the electric field at any point and at any time. Its two complex components which are orthogonal to the direction of propagation are two orthogonal sine oscillations. This is illustrated in figure 2.1.
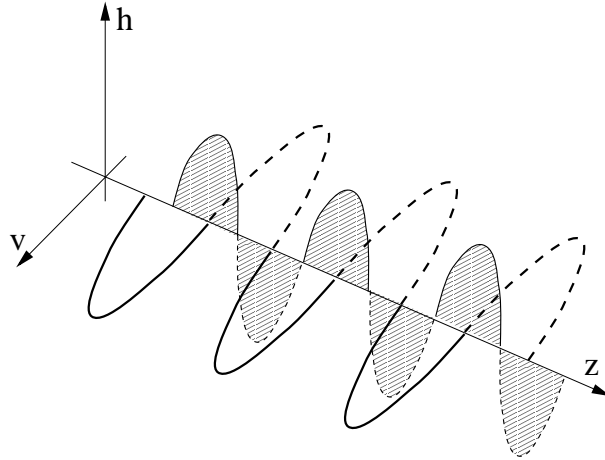
Figure 2.1: Two orthogonal waves propagating in z-direction

The Jones-vector can be described geometrically with the polarisation ellipse [Kon86]. This is the projection in the $z = 0$ plane of the geometrical points of the tip of the electric field vector. Important parameters of this description are the zero-phase (α), phase difference (φ), orientation of the main axis (θ), ellipticity (τ), amplitude (A) and the direction of the tip motion.

The basis $\vec{h}, \vec{v}$ of the Jones-vector can be chosen arbitrarily, any other linear independent basis will do as well. Of special interest are right and lefthand circular basis $(\vec{r}, \vec{l})$, as such antenna are widely available [Bal82]

$$\begin{pmatrix} \vec{h} \\ \vec{v} \end{pmatrix} = \frac{1}{\sqrt{2}} \begin{pmatrix} 1 & 1 \\ j & -j \end{pmatrix} \begin{pmatrix} \vec{l} \\ \vec{r} \end{pmatrix}. \tag{2.15}$$

2.2   Stokes-vector and Poincaré-sphere

Often, especially for the case of non coherent systems, it is convenient to transform the Jones-vector into the Stokes-vector [Wan88, UE90]. Instead of having now a two elements vector with complex elements a four real element vector results

$$\begin{pmatrix} g_0 \\ g_1 \\ g_2 \\ g_3 \end{pmatrix} = \begin{pmatrix} < E_h E_h^* + E_v E_v^* > \\ < E_h E_h^* - E_v E_v^* > \\ < E_h E_v^* + E_v E_h^* > \\ < j \left(E_h E_v^* - E_v E_h^* \right) > \end{pmatrix}. \tag{2.16}$$

The single elements of the Stokes-vector are not independent for a fully polarised electromagnetic wave, as

$$g_0^2 = g_1^2 + g_2^2 + g_3^2. \tag{2.17}$$

This causes also an information loss, as only three out of the previous four independent elements remain. Hence, the inverse transformation from the Stokes-vector back to the Jones-vector is not unique, the zero-phase is lost [Pot95].

The Poincaré-sphere allows a vivid representation of the Stokes-vector. The values of g_1, g_2, g_3 are applied to cartesian coordinates (h, v, z)[1]. De-

---

[1]Often it is also found the stereographic projection of the complex amplitude quotient

scribing the Poincaré-sphere in spherical coordinates $(2\theta, 2\tau, r)$, the following definitions are obtained:

$$
\begin{aligned}
r &= E_h E_h^* + E_v E_v^* \\
&= g_0 \tag{2.18} \\
2\theta &= \tan^{-1} \frac{E_v}{E_h} + \tan^{-1} \left(\frac{E_v}{E_h} \right)^* \\
&= \tan^{-1} \frac{g_2}{g_1} \tag{2.19} \\
2\tau &= \sinh^{-1} \frac{E_h E_v^* - E_v E_h^*}{E_h E_h^* + E_v E_v^*} \\
&= \sin^{-1} \frac{g_3}{g_0}. \tag{2.20}
\end{aligned}
$$

Points of particular interest on the Poincaré-sphere are the equator and the poles. The equator represents all points with linear polarisation, whereas the north pole represents lefthand circular and the south pole righthand circular polarisation. One advantage of the Poincaré-sphere over the polarisation ellipse description is the possibility of describing one polarisation with exactly one point and not with a set of points as it is needed to construct an ellipse. Similar polarised waves appear close to each other, noisy signals spread in a cloud of points around the mean polarisation. Figure 2.2 shows a Poincaré-sphere with the co-ordinate system.

2.2.1   Scattering and Mueller-Matrices

If a polarised electromagnetic wave is scattered by an object, a vector with two complex components is necessary to describe the behaviour [RBSK70]. This arises from the fact, that the wave will be scattered partly with the same polarisation and partly with the orthogonal polarisation. For describing the far-field plane-wave scattering completely, a matrix with four elements is needed, as the response for either of the transmitting polarisations has to be

---

$\rho = \frac{E_y}{E_x}$ on the unity sphere. In this case information about the amplitude of the wave is lost.
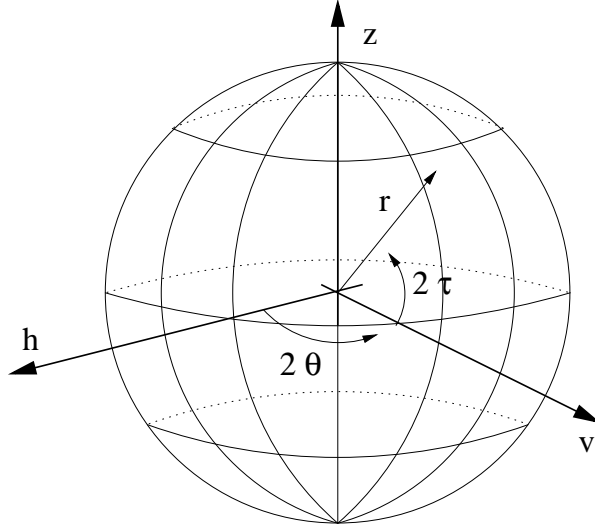
Figure 2.2: Visualisation of the Stokes-vector space: the Poincaré-sphere

taken into account[2]. This matrix is called scattering matrix.

$$
\begin{aligned}
\begin{pmatrix} E_h^s \\ E_v^s \end{pmatrix} &= \frac{e^{-jk_0 R}}{R} \, \mathbf{S} \, \begin{pmatrix} E_h^i \\ E_v^i \end{pmatrix} \\[2mm]
&= \frac{e^{-jk_0 R}}{R} \begin{pmatrix} S_{hh} & S_{hv} \\ S_{vh} & S_{vv} \end{pmatrix} \begin{pmatrix} E_h^i \\ E_v^i \end{pmatrix}.
\end{aligned}
\tag{2.21}
$$

Similar to the scattering matrix for the electromagnetic field vector, the Mueller-matrix gives the linear relation between the incoming and scattered Stokes-vectors [Käh92]

$$
\mathbf{M} = \left(\mathbf{R}^{\mathrm{T}}\right)^{-1} \cdot \mathbf{W} \cdot \mathbf{R}^{-1}
\tag{2.22}
$$

with a

$$
\mathbf{W} = \begin{pmatrix}
S_{hh}S_{hh}^* & S_{hv}S_{hv}^* & S_{hh}Shv^* & S_{hv}S_{hh}^* \\
S_{vh}S_{vh}^* & S_{vv}S_{vv}^* & S_{vh}Svv^* & S_{vv}S_{vh}^* \\
S_{hh}S_{vh}^* & S_{hv}S_{vv}^* & S_{hh}Svv^* & S_{hv}S_{vh}^* \\
S_{vh}S_{hh}^* & S_{vv}S_{hv}^* & S_{vh}Shv^* & S_{vv}S_{hh}^*
\end{pmatrix}
\tag{2.23}
$$

---

[2]In the case of backscattering there are only three independent elements in this matrix. Due to the reciprodicity theorem [RBSK70] $S_{ij} \equiv S_{ji}$ holds for $i \neq j$.

and a

$$\mathbf{R} = \begin{pmatrix} 1 & 1 & 0 & 0 \\ 1 & -1 & 0 & 0 \\ 0 & 0 & 1 & 1 \\ 0 & 0 & -j & j \end{pmatrix}. \tag{2.24}$$

Generally, as the scattering matrix contains complex elements of a voltage, it is used for coherent systems and the Mueller-matrix containing power-elements only for incoherent systems [Wan88].

In order to be able to separate different scattering mechanisms, many approaches exist that decompose either the scattering or the Mueller-matrix [Huy70, CP96, Kro93].

2.2.2   Coherence Matrix and Polarimetric Entropy

An approach to classify polarimetric data was shown by S. Cloude and E. Pottier [CP97]. They used two parameters which they call polarimetric entropy (H) and dominant scattering mechanism or anisotropy (α). The average coherence matrix $< \mathbf{T} >$[3]

$$< \mathbf{T} > = < \vec{S} \cdot \vec{S^*}^T > \tag{2.25}$$

with $\vec{S} = (S_{hh} + S_{vv}, S_{hh} - S_{vv}, 2S_{hv})^T$ has three eigenvalues, $\lambda_1, \lambda_2, \lambda_3$. The entropy of these eigenvalues is a measure for the polarimetric disorder of the averaged image pixels

$$H = \sum_{i=1}^{3} -P_i \log_3 P_i \tag{2.26}$$

with

$$P_i = \frac{\lambda_i}{\sum_{j=1}^{3} \lambda_j}. \tag{2.27}$$

The anisotropy α can be determined [CP97] by a parameterisation of $\mathbf{T}$ in the form:

$$\mathbf{T} = \mathbf{U}_3 \begin{pmatrix} \lambda_1 & 0 & 0 \\ 0 & \lambda_2 & 0 \\ 0 & 0 & \lambda_3 \end{pmatrix} \mathbf{U}_3^{\mathrm{T}} \tag{2.28}$$

---

[3]In the appendix an explicit expression of the coherence matrix is given in (B.5).

with

$$\mathbf{U}_3 = \begin{pmatrix} \cos\alpha_1 & \cos\alpha_2 & \cos\alpha_3 \\ \sin\alpha_1\cos\beta_1 e^{j\delta_1} & \sin\alpha_2\cos\beta_2 e^{j\delta_2} & \sin\alpha_3\cos\beta_3 e^{j\delta_3} \\ \sin\alpha_1\cos\beta_1 e^{j\gamma_1} & \sin\alpha_2\cos\beta_2 e^{j\gamma_2} & \sin\alpha_3\cos\beta_3 e^{j\gamma_3} \end{pmatrix} \qquad (2.29)$$

and a

$$\alpha = \sum_{i=1}^{3} P_i\alpha_i. \qquad (2.30)$$

Based on the knowledge of H and α, the data can be separated into eight classes. These classes correspond to different scattering events (α) and to different entropies (H).

2.2.3   Polarimetric Decomposition into Pauli-Matrices

Another approach to process and to classify polarimetric radar data is the decomposition of the scattering-matrix or the Mueller-matrix into a matrix with a different basis. The basis for these decomposition techniques corresponds to certain physical scattering mechanisms. Decompositions based on the scattering-matrix are usually coherent decomposition techniques, whereas decompositions based on the Mueller-matrix are incoherent. Examples of such a decomposition is the decomposition into Pauli-matrices according to [CP96], the decomposition into rotation-invariant Krogager-matrices [Kro93] or the decomposition into Huynen-parameters [Huy70].

The decomposition into Pauli-matrices divides the scattering matrix into four matrices. These four orthogonal matrices correspond to the scattering of an iso-surface, an iso-dihedral, a 45º rotated iso-dihedral and an iso-crosspolariser

$$\mathbf{S} = a\begin{pmatrix} 1 & 0 \\ 0 & 1 \end{pmatrix} + b\begin{pmatrix} 1 & 0 \\ 0 & -1 \end{pmatrix} + c\begin{pmatrix} 0 & 1 \\ 1 & 0 \end{pmatrix} + d\begin{pmatrix} 0 & -i \\ i & 0 \end{pmatrix}. \qquad (2.31)$$

In the case of calibrated backscatter data, the iso-crosspolariser part of the data d is equivalent to zero.

With this decomposition, the data can be separated into the single and odd bounce part a and into the even bounce parts b and c.

2.3   Information Theory

The basic element of information theory is the concept of entropy [CT91, Mac98, Mac99]. Entropy in information theory is a measure of the uncertainty of a random variable [SG96]; it is a measure of the amount of information required on the average to describe the random variable. This definition is in concordance with the definition of entropy in thermodynamics [Gri77]. This entropy should not be confused with the definition of polarimetric entropy [CP97] of (2.26).

Let X be a discrete random variable with an alphabet $\mathcal{X}$ and a probability density function $p_X(x), x \in \mathcal{X}$. Then the entropy of X is defined as

$$H(X) = - \sum_{x \in \mathcal{X}} p_X(x) \, \log_2 \left(p_X(x) \right). \tag{2.32}$$

The base of the logarithm can be chosen arbitrarily, choosing the base 2 results in the expression of the entropy in bits[4]. The definition is equivalent to the interpretation of the entropy as the expected value of $- \log_2 p(X)$

$$H(X) = - E[\log_2 p(X)]. \tag{2.33}$$

Extending the definition for the entropy from a single random variable to a pair of discrete random variables (X, Y) with a joint distribution $p_{X,Y}(x, y)$, $x \in \mathcal{X}$ and $y \in \mathcal{Y}$, the joint entropy $H(X, Y)$ of a pair of discrete random variables can be defined [CT91] as

$$H(X, Y) = - \sum_{x \in \mathcal{X}} \sum_{y \in \mathcal{Y}} p_{X,Y}(x, y) \, \log_2 \left(p_{X,Y}(x, y) \right). \tag{2.34}$$

Furthermore, the conditional entropy of a random variable, given another random variable can be calculated [CT91] as the expected value of the entropies of the conditional distributions, averaged over the conditioning random variable

$$H(Y|X) \;\; = \;\; \sum_{x \in \mathcal{X}} p_X(x) \, H(Y|X = x)$$

---

[4]The addition of terms with zero probability does not effect the entropy as $\lim_{x \to 0} \left(x \log_2 x \right) = 0$.

$$
\begin{aligned}
&= - \sum_{x \in \mathcal{X}} p_X(x) \sum_{y \in \mathcal{Y}} p_{Y|X}(y|x) \log_2 p_{Y|X}(y|x) \\
&= - \sum_{x \in \mathcal{X}} \sum_{y \in \mathcal{Y}} p_{X,Y}(x,y) \log_2 p_{Y|X}(y|x).
\end{aligned}
\tag{2.35}
$$

The mutual information is the relative entropy between the joint distribution and the product distribution. It describes the reduction of uncertainty of X, with the knowledge of Y [Mac99]

$$
I(X;Y) = \sum_{x \in \mathcal{X}} \sum_{y \in \mathcal{Y}} p_{X,Y}(x,y) \log_2 \frac{p_{X,Y}(x,y)}{p_X(x)\, p_Y(y)}.
\tag{2.36}
$$

The mutual information may also be re-written as

$$
I(X;Y) = H(X) - H(X|Y).
\tag{2.37}
$$

The mutual information may not be negative, for any two random variables X,Y follows $I(X;Y) \geq 0$ with equality if and only if X and Y are independent.

The mutual information of two random variables X and Y, that may observed at the location of Y, corresponds to the information content, that was transmitted from X to Y. The maximum of the mutual information $I(X;Y)$ is the maximum possible rate of error free transmission. This maximal mutual information is also called the capacity of the channel. The channel capacity [Sha49, Sha48] can be expressed explicitly for channels of a bandwidth Δf disturbed by gaussian noise with a signal to noise ratio of $\frac{S}{N}$

$$
C = \Delta f \log_2 \left(1 + \frac{S}{N} \right) \quad [\text{bit/s}].
\tag{2.38}
$$

The information of a single message X being transmitted on this channel is equivalent to the scarcity value of its occurrence

$$
I(X) = - \log_2 P(X) \quad [\text{bit/s}].
\tag{2.39}
$$

Figure 2.3 serves to illustrate the various entropies for a transmission channel.

For the ease of calculations with entropies, the chain rule [CT91]

$$
H(X_1, X_2, \ldots, X_n) = \sum_{i=1}^{n} H(X_i | X_{i-1}, \ldots, X_1)
\tag{2.40}
$$
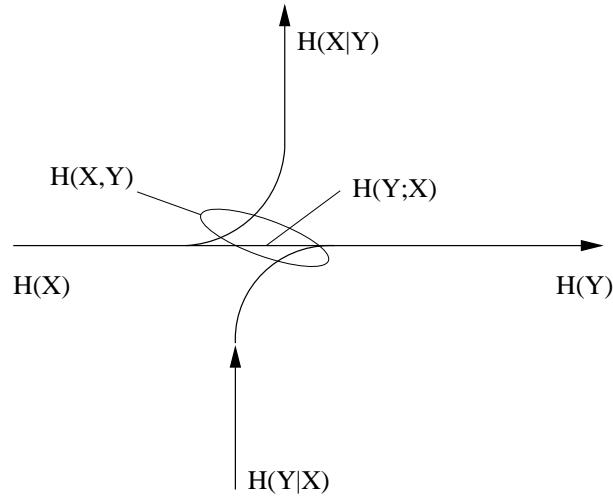
Figure 2.3: Context between the entropies

and corollary [CT91]

$$H(X,Y|Z) = H(X|Z) + H(Y|X,Z) \tag{2.41}$$

may be applied. Not only entropy, but also mutual information satisfies a chain rule [Mac98]

$$I(X_1, X_2, \ldots, X_n; Y) = \sum_{i=1}^{n} I(X_i; Y|X_{i-1}, \ldots, X_1). \tag{2.42}$$

This chain rule gives also the basis for the data processing inequality theorem, describing the loss of information in a data processing chain $X \to Y \to Z$

$$I(X;Y) \geq I(X;Z). \tag{2.43}$$

The entropy fulfills a couple of conditions, the most important may be summarised as:

- it is non-negative: $H(X) \geq 0$, with equality if and only if X is not random,

- the entropy is reduced by conditioning, $H(X|Y) \leq H(X)$, with equality if and only if X and Y are independent,

- the joint entropy is smaller than the sum of the individual entropies $H(X_1, X_2, \ldots, X_n) \leq \sum_{i=1}^{n} H(X_i)$, with equality if and only if all X_i are independent,

- the entropy has an upper bound: $H(X) \leq \log_2 |X|$, with equality if and only if X is uniformly distributed over X. Hence, the perfect information content in a data set is $\log_2 |X|$,

- $H(X)$ is concave in X.

2.4 Basics of Radar Systems

Radar (*RAdio Detection And Ranging*) is "a device for transmitting electromagnetic signals and receiving echoes from objects of interest (targets) within its volume of coverage" [IEE90].

2.4.1 The Radar Equation

The quality of a radar to detect the echoes is bounded by several limits [Sko81]. Among those limits, power constraints play a central role. The radar signal power may not be sufficient to illuminate a target such that signal that is reflected from the target can still be detected at the receiver. This is illustrated in the radar equation [Sko81]:

$$P_r = \frac{P_t \, G}{4\pi R^2} \, \sigma \, \frac{A_e}{4\pi R^2}. \tag{2.44}$$

The radar equation tells that, in order to detect a target of radar cross section σ at a given distance R using a radar with average transmit power P_t, transmit antenna gain G and effective area of the receiving antenna A_e, the received signal power P_r needs to sufficient for detection. As radars usually use the same antennas for transmission and reception, the radar equation may also be written, taking the relationship between antenna gain and effective area

$$G = \frac{4\pi A_e}{\lambda^2} \tag{2.45}$$

into account as

$$P_r = \frac{P_t \, G^2 \, \lambda^2 \, \sigma}{(4\pi)^3 R^4}. \tag{2.46}$$

By use of this equation also the maximum detection range of a radar can be determined,

$$R_{\mathrm{max}} = \sqrt[4]{\frac{P_t G^2 \lambda^2 \sigma}{(4\pi)^3 S_{\mathrm{min}}}} \tag{2.47}$$

with $S_{\min} = P_r$ as the minimum detectable signal power.

Since noise is the main limiting factor for the radar sensitivity, the introduction of noise figures for the receiver gives a relationship for the maximum detection range of a radar, that is closer to the specifications of the components:

$$R_{\max} = \sqrt[4]{\frac{n\,P_t\,G^2\,\lambda^2\,\sigma}{(4\pi)^3 k T_0 \Delta f \tau f_p F_n \left(\frac{S}{N}\right)_1}} \qquad (2.48)$$

where F_n is the noise figure of the receiver, $T_0 = 290\,[\mathrm{K}]$ the standard temperature according to the IEEE specification, Δf the receiver bandwidth and $k = 1.38 \cdot 10^{-23}\,[\mathrm{J/K}]$ Boltzmann's constant. In this equation effects of averaging are taken into account, n is the number of integrated coherent looks and $\frac{S}{N}_1$ is the signal to noise ratio required at the receiver output, based on a single look detection. Finally the effects of a pulsed radar operation are taken into account, τ is the pulse length and f_p the pulse repetition frequency.

Distributed Targets

In all considerations above, the target was a point scatterer with a radar cross section σ. This assumption is only valid for simple cases, such as the detection of an aircraft. As soon as the target is more complex, or when more than one target is involved in the scattering mechanism, the average value of the scattering cross section per unit area, also known as the differential scattering coefficient σ^0, is a suited description [UMF82]

$$\overline{P_r} = \frac{\lambda^2}{4\pi^3} \int_A \frac{P_t\,G^2\,\sigma^0}{R^4} dA. \qquad (2.49)$$

It can be noted, that in this case, the power is no longer decreasing with a R^4, but as the illuminated area is increasing approximately with R, the power dissipation is reduced to a factor of R^3 for surface targets and even further reduced for volume targets to a factor of R^2.

In order to apply this form of the radar equation, two main restrictions must be fulfilled:

- many individual point scatterers need to be in the area over which the antenna gain, the transmitted power and the range are essentially constant,

- many more scatterers need to exist in the total illuminated area.

2.4.2 Resolution of a Radar

The resolution of a radar can be divided into two different cases. Resolution in range direction, depending only on the bandwidth of the signal, and resolution in cross-range direction, depending on the available antenna aperture [Sti83].
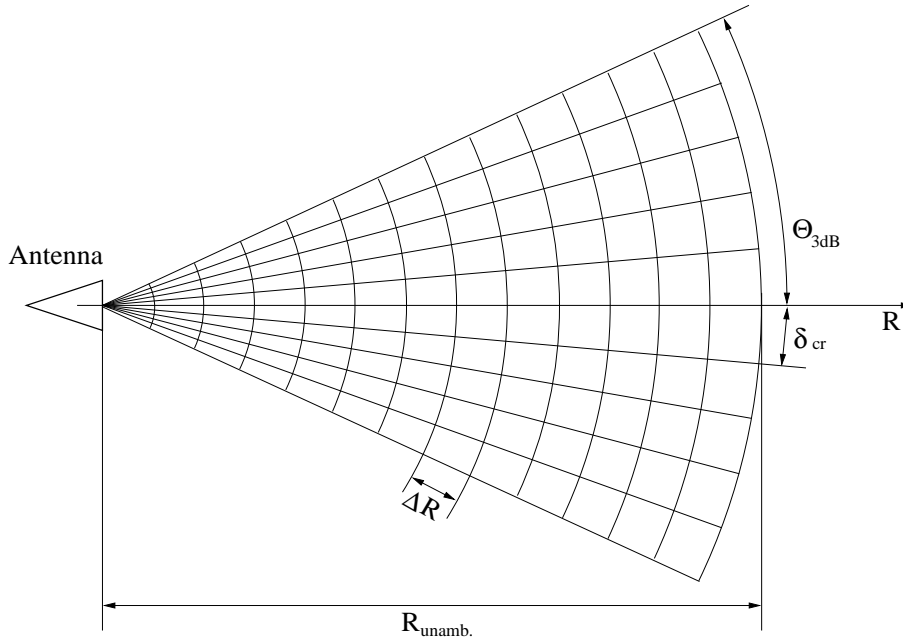
Figure 2.4: Range- and cross-range resolution of a radar

Resolution in Range Direction

For pulsed radar systems, the determination of range in a radar system is done by measuring the time delay between the transmission and the reception of a signal [Men91]. Having a target at distance R the round-trip propagation delay is $T = 2\frac{R}{c}$, thus a pulse of length τ corresponds to a range increment of:

$$\Delta R = c\frac{\tau}{2}. \tag{2.50}$$

This means that two targets separated at greater distances than ΔR are distinguishable. Hence, narrowing the pulse length will enhance the resolution,

but also increase bandwidth Δf of the radar, as $\Delta f\ \tau \simeq 1$. Apart from the maximum range limit calculated in (2.48), a pulsed radar has a range limit due to the repetition of the pulses[5]. This unambiguous range depending on the pulse repetition frequency should be chosen higher than the maximum detection range or the presence of objects after the unambiguous range needs to be excluded

$$R_{\text{unamb.}} = \frac{c}{f_p}. \tag{2.51}$$

In contrast to the direct method of a pulsed radar, in which all the spectral components of the signal are present simultaneously, it is also possible with synthetic methods to collect sequentially the spectral components. A typical example of such a radar type is a stepped frequency CW radar [UE90]. In the simple case of high range resolution by synthetic means, several narrow band measurements are executed at discrete frequencies. Although the single narrow band responses have insignificant resolution potential, the coherent combination of all the responses provides a resolution equal to the resolution of a pulsed radar system of the total bandwidth. The required signal processing for the synthetic range resolution can be determined with linear system theory by a simple inverse Fourier transformation [KK92]. The resolution in range is

$$\Delta R = \frac{c}{2\,\Delta f}. \tag{2.52}$$

Also the synthetic generation of range resolution suffers ambiguity problems. These are caused by the finite number of frequency steps n_f used for the inverse Fourier transform. The unambiguous range in this case is:

$$R_{\text{unamb.}} = \frac{n_f\,c}{2\,\Delta f}. \tag{2.53}$$

Resolution in Cross-range Direction

For simple radars the resolution in cross-range directions, depends on the radiation pattern of the antennas [Sti83]. Two characteristics of the radiation pattern are crucial for the resolution, the 3-dB beamwidth in both azimuth $\Theta_{3\text{dB}}$ and elevation $\Phi_{3\text{dB}}$ and the intensities of the first sidelobes

---

[5]With the use of pseudo random pulse sequences this limit can be widely extended [Kro91].

compared to the main lobe level. As a good approximation, the resolution in cross-range for real aperture antennas can be given as [Bal82]

$$\delta \simeq \Theta_{3\text{dB}}\, R \simeq \frac{\lambda R}{D}, \tag{2.54}$$

where D is the aperture length of the antenna and R the target distance.

Similar to the synthetic processing for range resolution, also in cross-range direction synthetic resolution is achievable. Such methods are used in (inverse) synthetic aperture radars; along a known trajectory many coherent looks are taken, using an antenna without a particularly small beamwidth [CM91, Men91].

Two scatterers can be separated if their phase differs by at least 360°. A differential path length of $\pm\frac{1}{4}\lambda$ causes this minimum phase variation across the aperture. Hence, the resolution in cross range (δ) can be found as

$$\delta^{\text{SAR}} = \frac{\lambda R}{2L}. \tag{2.55}$$

For a given wavelength λ and target distance R, this resolution can be increased by increasing the aperture dimension L. The difficulties caused by large physical apertures can be avoided by synthesizing a synthetic aperture. It has to be noted that the resolution of a synthetic aperture radar is twice as good as the resolution of a real aperture radar. This is due to the fact that the phase differences double for SAR imaging with respect to real aperture imaging. The geometry of this synthetic aperture is in principle of no matter, though circular (spotlight-SAR) and linear (linear SAR) synthetic apertures are preferred as the signal processing is significantly simplified[6] [7]. It has to be noted that the maximum achievable resolution is reached with a physical antenna with a large beamwidth and a long synthetic aperture. This maximum resolution is range independent and depends only on the real aperture D of the antenna [Men91]:

$$\delta \approx \frac{D}{2}. \tag{2.56}$$

---

[6]Also two synthetic apertures in orthogonal directions are possible, in order to create three-dimensional radar images.

[7]The creation of a forward looking, in range-direction, synthetic aperture radar is also possible. Yet, the effects of unambiguousness need to be compensated, e.g. using an array of forward looking antennas

In order to avoid aliasing caused by the limited number of looks [KK92], the number of looks needs to be chosen according to

$$n_{cr} \geq \frac{4\,D\,\sin\frac{\Theta}{2}}{\lambda} + 1 \tag{2.57}$$

with Θ as the beamwidth of the antenna. A detailed description of various synthetic imaging techniques can be found in [CM91, Men91].

Dynamic Range

Beyond the spatial resolutions in all coordinates other resolution limits for the quality of the radar exist [Sko81].

The resolution of the A/D-converter is responsible, whether or not the detection level as indicated in the radar equation may be reached. Usually this is not a major concern, as the resolution of an A/D-converter can be magnified easily. The dynamic range of the signal processing depends on the number of bits n_{bits} used for sampling [Smi99]:

$$\begin{aligned} \delta_{dr} &= 20\,\log_{10}\left(2^{n_{\text{bits}}} - \frac{1}{2} - \frac{1}{\sqrt{12}}\right)\,[\text{dB}] \\ &= 20\,\log_{10}\left(2^{n_{\text{bits}}} - 0.79\right)\,[\text{dB}]. \end{aligned} \tag{2.58}$$

The spectral resolution for a doppler radar determines with what accuracy a velocity difference may be detected. As there exists many ways of constructing such a doppler radar, it is either affected by the accuracy of a bandpass filter, the accuracy of a local oscillator or the speed of an A/D-converter [Sko81, Sch98].

Chapter 3

Information of a Polarimetric Radar

Polarisation diversity in radar has been recognised as a tool to provide more information on the target [vZZ91, Eva88, EvZ90]. Especially natural surfaces and man made targets are theoretically suitable targets [Zeb91]. Recent developments in the field of interferometric polarimetry [CP98] widen the set of suitable target features also towards such parameters as vegetation height [LSFSC98] and distinction of more than one well defined scattering center in one resolution cell [CP96, Kro93]. These applications are all based on various theoretical models and application of real data has shown promising results. However, the increase in information has not been quantified yet, nor has a measure for the usefulness of polarisation diversity in radar technology been developed.

In this chapter the principle of a polarimetric radar in terms of entropy flows is shown. Hence a method to quantify the additional information that can be obtained by using polarisation diversity.

3.1   Historic Development of Information in Radar Systems

When radar was first used for military applications during World War II, it had been developed for detecting enemy aircraft [Sti83]. In order to detect and to combat these aircraft, their positions in azimuth, elevation and range needed to be known. In this very first phase of radar technology the infor-

mation could be described by the radar equation (2.48). The information was a binary choice of target or no-target in a given resolution cell[1]. Figure 3.1 shows such a situation.
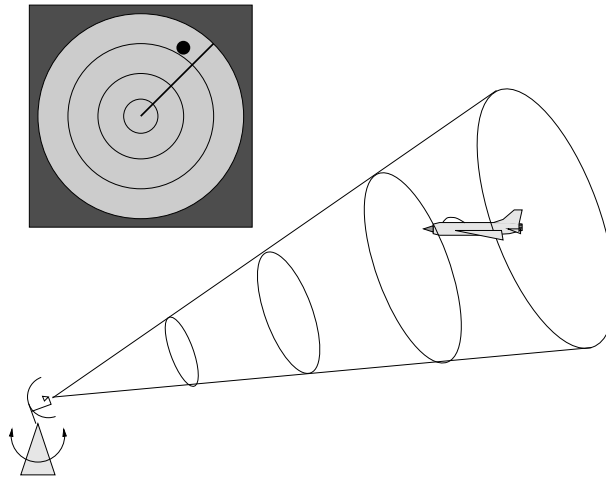
Figure 3.1: The first use of radar: Detection of single targets in the airspace

This binary choice of target or no target implicated the use of statistical methods for the optimisation of the receiver and the waveform [Kro86, Kro88b] rather than for describing the target.

In the years following World War II, many other applications for radar have been found, where this target or no-target information was useful. Examples for these applications are air-traffic control or ship collision warning. Immediately, the application of radar for large distributed targets was recognised. Air-borne and ground based weather radars were used for detecting clouds or thunderstorms. In this case, the targets were much larger than the resolution cell size of the radar. The radar equation for distributed targets was the theoretical basis for these new applications. The information content in the radar data was not anymore described by a binary target or no-target situation, but by the resolution cell size and the signal-to-noise ratio [Woo53].

The next step of radar development was combining the above mentioned detection criteria, the detection of a single target in a clutter environment caused by a much larger target. An aircraft that wanted to detect a ship

---

[1]During the war, no party was able to produce radars with a wavelength smaller than 600 MHz [Sko81]. The use of these relatively low frequencies caused the resolution cells to be significantly larger than the targets.

in the ocean had to face this problem. The ocean surface reflects the signal energy similarly as the ship. The use of radar polarimetry was used to solve this problem. As the scattering matrix (2.21) contains not only a single intensity value, but a matrix of four complex values [RBSK70][2], the possibilities to distinguish between different targets increase dramatically. The optimisation of the contrast of a radar image by choosing a suitable polarisation was one of the results of polarimetric radar [Boe97].
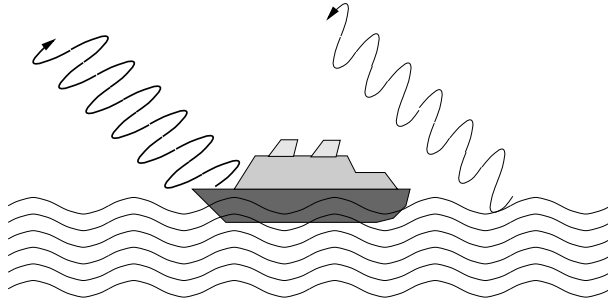
Figure 3.2: Distinction between targets with radar polarimetry

One of the latest applications of radar is remote sensing [UMF81]. Despite the fact that all radars are "remote sensors", in this particular application, this term refers to the remote detection of the environment [UMF86]. Here the description of the target becomes much more complicated, as in spite of improved radar resolution, a single resolution cell comprises many and in most cases many different targets [UMF82]. Radars used for remote sensing are also referred to as "imaging radars", as these radars are meant to create an image of the environment rather than detecting single targets. The information comprised in these radar images is not anymore the information that could be described with the radar equation, but resolution sets now the limit for the information. The development of improved radar imaging techniques, such as sidelooking array radar (SLAR) [Sti83] or synthetic aperture radar (SAR) [Men91], stimulated this trend in radar technology.

Although the resolution of imaging radars has become very high, the polarimetric Shuttle Imaging Radar "SIR-C" [Eva93] had a resolution on the

---

[2]In the case of a monostatic radar, two of these four complex values are equivalent ($S_{hv} \equiv S_{vh}$). The problem of absolute phase measurements further diminishes the dimension of the scattering matrix, such that it contains only five independent values.

order of 12 by 12 meters, the single resolution cell or image pixel still contains generally more than one single target. In order to be able to separate these targets, again polarimetry was used. The scattering matrix of each pixel can be decomposed into several standard scattering matrices [Kro93, CP96, Huy70]. With this approach, basic scattering mechanisms can be separated. These basic scattering mechanisms comprise for example single- and double-bounce scattering, hence sphere- or dihedral-like scattering.

3.2   Principles of a Polarimetric Radar

3.2.1   The Signal Chain of a Polarimetric Radar

The basic datum measured by a polarimetric radar is the complex scattering matrix for each resolution element [RBSK70]. This resolution element can either be defined by the pulse-duration of a pulsed radar or by the band-width for all other radars (FMCW or stepped frequency)[3]. In the following discussion is always assumed that the exchange of bandwidth and resolution has taken place[4]. Because of operational requirements, generally two approaches are being followed for recording the scattering matrix [Käh92]: one is the sequential transmission of a horizontal and vertical polarised signal and the reception of both polarisations contemporaneously, the other concept transmits contemporaneously both polarisations with a small frequency shift and receives contemporaneously four signals. The first approach is usually applied for instrumentation and laboratory equipment, while the second approach is widely used for air- or space borne missions, where the dwell time of the radar on the target is limited. While the first approach has the only constraint of a possible change of the target between the two transmit signals, the frequency shifted signal of the second approach might contain information other than desired.

Describing the signal path of a polarimetric radar signal [WK91], four ele-

---

[3]The pulse-length of a pulsed radar is of course equivalent to the bandwidth of a FMCW or stepped frequency radar with the same resolution [Sko81].

[4]This operation, being basically an inverse Fourier transform, can be applied as long as the target has a linear behaviour in the frequency band of interest. Ultra-wide-band radars require a special treatment, as here the frequency contains information other than spatial resolution [UF98]

ments have to be considered. First the signal passes through the transmitter hardware. Especially the antennas will contribute to a significant distortion of the signal. Thereafter the signal passes through the propagation medium. The propagation medium, in general being air, usually has little contribution to the signal distortion. The main effect is the attenuation depending on range and occasionally on the various absorption bands. This stage will be called "downlink" according to a satellite based radar. The next element in the signal chain is the interaction with the target. Ideally all polarisation dependent effects should take place here. Due to the limited resolution of the radar, usually the information in the scattering matrix is not information on a single target, but the average information of the integrated resolution cell[5]. After the scattering the signal passes again through the propagation medium. For most radars the signal will follow the same track as on its way from the transmitter to the target, only the direction of propagation is reversed. Again, following a satellite radar configuration, this stage will be called "uplink". This "normal" case is called monostatic radar [UMF82]. Radars with the receiver being located at positions different from the transmitter position are called bistatic, radars with receivers at more than one position are called multistatic. As the vast majority of all radars being used today are monostatic radars, the discussion will concentrate on them. Finally, the signal drain is the receiver of the radar, again the antenna will primarily contribute to the distortion of the signal [Sko81].

3.2.2   Entropy Paths for the Polarimetric Radar

Figure 3.3 shows the paths, which the transmitted signal of a polarimetric radar follows. Whereas the desired information is the interaction with the target, many other interactions during the down- and up-link corrupt the information on the receiver side of the radar system. In general, the transmitted signal is no random signal[6] but it is known at each time. For the polarimetric monostatic radar three data paths out of four have to be consid-

---

[5]Resolution cell sizes are on the order of 20 meters for satellite data, for laboratory data centimeter resolution can be achieved.

[6]In contradiction to noise radars or (pseudo-) randomly pulsed radars, where the coherence is obtained by correlation of the received signal and a stored replica of the transmitted signal [Luk98].

ered. This reduction arises from the symmetry of the monostatic scattering matrix [RBSK70]. This symmetry is caused by the reciprocity theorem. The reciprocity theorem states that both cross polarisations are equal for any isotropic and linear medium [Bal89, Sim89][7]. In other words:

$$S_{hv} \equiv S_{vh}. \tag{3.1}$$

Figure 3.3 shows all possible data paths of a full polarimetric radar. Along
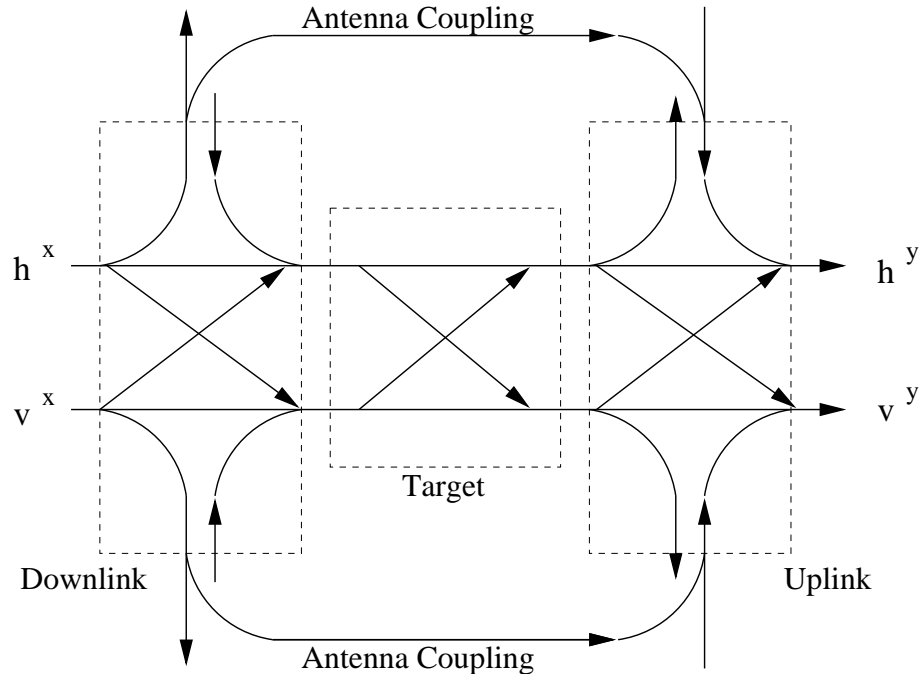
Figure 3.3: Entropy paths for the polarimetric radar

all of these paths only the interaction with the target comprises the desired information for the user, while on all other paths noise or cross-polarised channel data is added to the information. Again, it is obvious that the reduction of decorrelating effects in the down- and uplinks is crucial for the acquisition of polarimetric information on the target. As radar data in general comprises not only the magnitude but also the phase of the signal, the entropy has to take both in-phase and quadrature information into account:

$$H(h) = H(h_I) + H(h_Q|h_I) \tag{3.2}$$

---

[7]For un-isotropic media, the Faraday-rotation is an application of unequal depolarisation in the cross-polarised channels [Wie90].

Furthermore having a target where

$$H(h) + H(v) \leq H(h+v) \tag{3.3}$$

that is a target, where the responses to a stimulus in either of the polari-sations is not independent of the stimulus to the orthogonal polarisation, is reducing the entropy of polarimetric radar data. Finally, the information in any channel will have a certain coherence [UMF86]. This assumption is val-idated for any imaging data, as in order to detect any structure of an object a certain number of pixels are needed [Men91, Sti83].

Recapitulating the above mentioned constraints for the entropy of polari-metric radar data, the following relations can be observed at the receiver side of the radar:

1. all channels contains a certain coherence

$$0 < H(ij) < H(ij)^{max}, \tag{3.4}$$

with a $H(ij)^{max}$ equal to the length in bits of the single data-element.

2. the orthogonal polarisations are not independent

$$H(hh, vv) < H(hh) + H(vv), \tag{3.5}$$

3. the cross polarised part of the signal is not independent from the co-polarised signal

$$H(hh, hv) < H(hh) + H(hv)$$
$$H(vv, hv) < H(vv) + H(hv),$$
$$\tag{3.6}$$

4. both cross polarised signals are equal (backscattering)

$$S_{hv} \equiv S_{vh}. \tag{3.7}$$

Beyond these constrains, the down- and uplink capacity reduces the avail-able signal space due to its noise and depolarisation effects [Sha49, Bro60, KMB59] with a

$$C^{(\text{transmission})} = C^{(\text{downlink})} \cap C^{(\text{uplink})} \tag{3.8}$$

where the capacity of each link can be calculated with the knowledge of the signal S, the noise N and the depolarisation D level [Cov72, Mac99] as

$$C = 2\,\Delta f\;\log_2\left(1 + \frac{S}{N + D}\right).\tag{3.9}$$

This capacity is the capacity of two parallel channels which suffer crosstalk between them. This explains the differences to Shannon's channel as described in (2.38). In order to express the whole information content in terms of entropies in analogy to figure 3.3, the result can be written [CT91] as

$$H\,(\mathbf{S}) = H(hh, hv, vh, vv).\tag{3.10}$$

Due to the symmetry in the backscattering signal, immediately follows a first simplification, as

$$H(hv, vh) = H(hv) = H(vh)\tag{3.11}$$

or $H(hv|vh) \equiv 0$. The remaining information is illustrated in figure 3.4. Using the chain rules for mutual information and entropy [Mac99, CT91], the whole polarimetric radar entropy might also be written in a more understandable way

$$H\,(\mathbf{S}) = H(hh) + H(vv|hh) + H(hv|vv, hh).\tag{3.12}$$

Hence, the total information content in the scattering matrix is the self-information of one channel $H(hh)$ plus the conditional entropies of this channel with respect to the other two remaining channels. The additional information, that has been obtained by using a full polarimetric radar rather than a single polarisation radar is contained in the two last terms of the above formula. It is of course equivalent to write the formula referring the entropies to the vv-channel or any combination of the channels, such as RR or LL. Though this result might seem to satisfy the problem of calculating the information content of polarimetric data, many problems remain with the applicability of this formula, as the calculation of entropies is neither straightforward nor easy to apply to real data.

3.3 Information Content of Polarimetric Data

In section 3.2.2 it was shown that the entropy of polarimetric radar data can be described according to (3.12) and that it can be visualised as shown
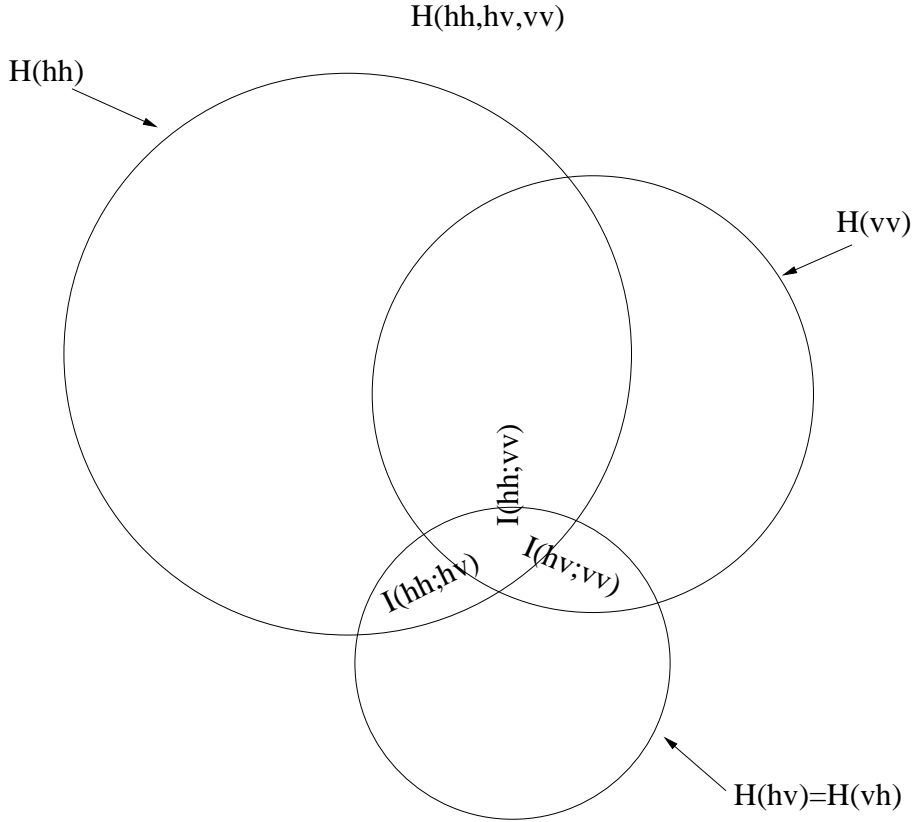
Figure 3.4: Entropy regions for the polarimetric radar information

in figure 3.4. This entropy corresponds to the total information content of polarimetric data.

3.3.1 Gain by Polarimetry

Comparing the result of (3.12) with the information content of a single polarisation channel[8], it is possible to quantify the additional information that has been recorded using a polarimetric radar

$$i^{hh} = H(vv|hh) + H(hv|vv, hh). \qquad (3.13)$$

As the absolute value of the additional information of a radar image does not reflect the characteristics of the imaged area, a better measure for the use

---

[8]The information content of a single polarisation depends of course on the polarisation chosen. For the further considerations, this single polarisation will be chosen as horizontal (hh). Hence, the single polarisation channel has an information of $H(hh)$.

of the polarimetric information is the gain that is obtained by using a full polarimetric radar system instead of using a single polarisation radar. This polarimetric gain, based on the entropy and referred to the entropy of e.g. hh-polarisation, may be defined as

$$
\begin{aligned}
g_{hh} &= \frac{i^{hh}}{H\,(hh)} \\
&= \frac{H(vv|hh) + H(hv|vv, hh)}{H\,(hh)}.
\end{aligned}
\tag{3.14}
$$

In terms of the figure 3.4, this is the total additional entropy area divided by the entropy area of a single polarisation channel.

3.4   Local Gain

Though the calculation of the polarimetric gain according to (3.14) shows how much information is in a polarimetric data set, it does not tell how the information is distributed in these data. Therefore the problem of locating areas with a high polarimetric information content arises. Instead of using all available data for the determination of the entropies involved in the calculation of the polarimetric gain, the data is sub-divided into small areas and the polarimetric gain is evaluated in each of these areas. Thus, the polarimetric gain depends on the position of the sub-area, or

$$
< g_{hh} > = g_{hh}(x, y).
\tag{3.15}
$$

Hence, the polarimetric gain is defined locally. Such a local polarimetric gain would significantly simplify the data analysis, as the processing time can be diminished in areas where polarimetry does not add any information.

Applying the gain definition (3.14) to a local set of the data, a measure of the differences between each of the polarimetric channels is obtained

$$
< g_{hh} > = \frac{< H(vv|hh) > + < H(hv|vv, hh) >}{< H\,(hh) >}.
\tag{3.16}
$$

The calculation of the polarimetric gain as described in this method suffers two problems:

- the number of pixels involved for the calculation of the entropies,

- the dependence of the path along which the entropy is calculated.

The first problem cannot be solved in closed form. The number of pixels involved in the calculation of the entropies should contain all pixels of a single target type. Hence, it depends on the target size and the resolution cell size.

To tackle the second problem, a way is given to maximise the coherence of the data, hence to scan along a path maximising the likelihood to cover a target totally before the path will meet another target in section 3.5.

3.5 Scan Path Maximising the Coherence

As stated in the preceding paragraph, the type of scan that is used to scan the image will influence the outcome of signal processing [PTVF92]. Therefore the scan path has to be chosen with maximum care, as it might be possible to increase the coherence or the auto-correlation of a signal by using an optimised scan. The requirements for such a scan that does not optimise the result for special data, but does so for general data, are:

1. space filling curve without self-intersections,

2. coherence maximisation for the data along the scan path,

3. readily implementable in software,

4. close mathematical description available,

5. easily expandable from two-dimensional data to more dimensions.

3.5.1 The Hilbert-Curve

One curve that will fulfill all the above mentioned criteria is the Hilbert-curve [Hil91] or Peano-Hilbert-curve [Pea90, NP92]. Though it is a curve, hence a one-dimensional object, it covers completely a two-dimensional surface in finite time [PAB68, Gri86]. This is due to its fractal properties, properties which enable also an elegant and easy mathematical description because recursive implementation in software [PJS92]. The original curve is applicable

to any two-dimensional data array, having an edge with a length being a power of two. For more dimensions the curve is readily expandable [Gil58] and preserves all of its properties. The extension for data arrays, not having edges of the required lengths and not being square-arrays by the use of Murray polygons, being a generalisation of Peano-curves are given in [Col91]. An alternative solution for general rectangles is the decomposition of the data array into smaller rectangles from one of a few standard sizes, as described in [WM91].

The Hilbert-curve construction starts with a point in a square ($\mathcal{H}_0$). In the next step, this square is divided into four equal quarters. The centers of each quadrant are connected by three line segments creating a U-shaped curve. Again each quadrant is divided into four segments. The seed is reproduced in four copies, each of them scaled by a factor of $\frac{1}{2}$. In each quadrant is placed a copy of the seed. In the first quadrant the copy is rotated by $-\frac{\pi}{2}$ (counterclockwise), while in the second quadrant the copy is rotated by $\frac{\pi}{2}$ (clockwise). The open ends of the copies are connected. The curve is again scaled and copied and so forth. For an infinite number of copies, the whole surface will be covered by this one-dimensional curve. The procedure is described in figures 3.5 to 3.7. In step n, the curve $\mathcal{H}_n$ contains 4 copies of $\mathcal{H}_{n-1}$, being connected by three lines and it covers an area of 2^{2n} data points.

The seed for the Hilbert-curve, the single point[9] in a square may be placed in the origin of the coordinate system

$$\mathcal{H}_0 = \begin{pmatrix} 0 \\ 0 \end{pmatrix}. \tag{3.17}$$

The recursive construction rule for the Hilbert-curve follows the equation

$$\mathcal{H}_n = \left\{ \begin{pmatrix} 0 & 1 \\ 1 & 0 \end{pmatrix} \mathcal{H}_{n-1}, \left(\mathcal{H}_{n-1} + \begin{pmatrix} 0 \\ 2^{n-1} \end{pmatrix} \right), \left(\mathcal{H}_{n-1} \begin{pmatrix} 2^{n-1} \\ 2^{n-1} \end{pmatrix} \right), \right.$$
$$\left. \left(\begin{pmatrix} 0 & -1 \\ -1 & 0 \end{pmatrix} \mathcal{H}_{n-1} + \begin{pmatrix} 2^n - 1 \\ 2^{n-1} - 1 \end{pmatrix} \right) \right\} \tag{3.18}$$

---

[9]In literature, the seed of the Hilbert-curve is referred as the U-shaped curve [Col83, Gri86, Gol81, WW83], corresponding to the 1st step of the algorithm presented here. The single seed-point seams to be a much more general description, which also simplifies the realisation in code.
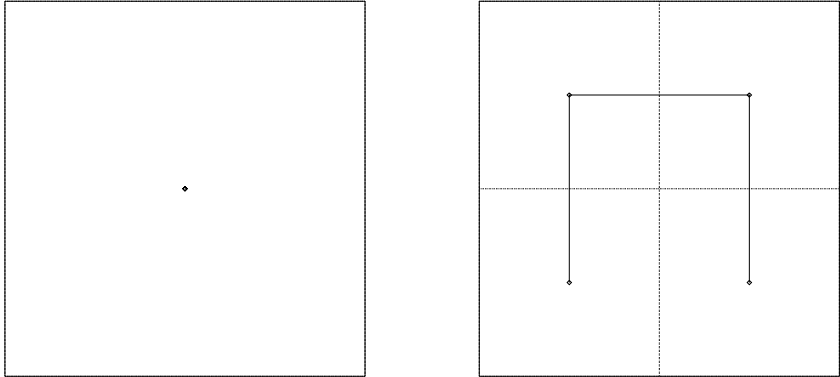
Figure 3.5: Generation of the Hilbert-curve seed and 1st step
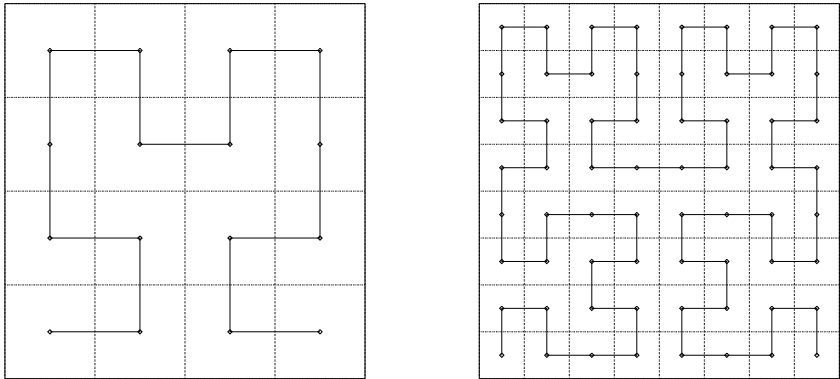
Figure 3.6: Generation of the Hilbert-curve 2nd and 3rd step
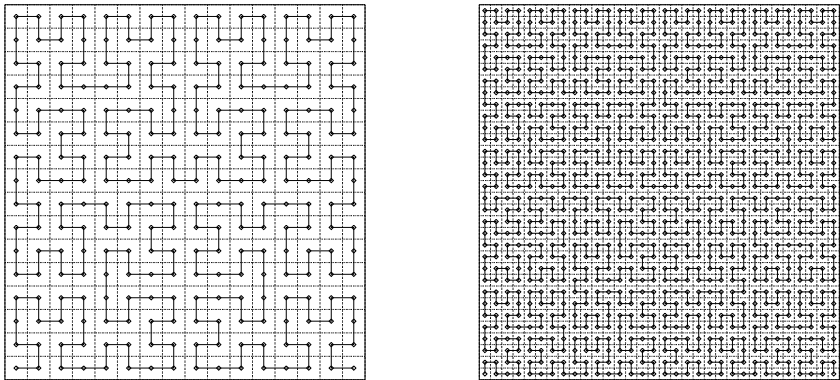
Figure 3.7: Generation of the Hilbert-curve 4th and 5th step

where the matrices turn the preceding Hilbert-curve (anti-) clockwise and the added vectors shift the curve into its new position.

As special characteristic of the Hilbert-curve can be observed, that for each k it covers the sub-array A_{2^k} quadrant by quadrant, in other words it never leaves a quadrant before visiting each of its cells. This behaviour is responsible for the property of maximising the coherence between the single elements of the data matrix [LZ86].

Another important fact that favors the use of the Hilbert-scan with regard to a raster-scan, is the possibility to process the data as a vector instead of a matrix. This allows to reduce significantly the data processing time, for example while using fast-Fourier-transforms, as the dimensionality has shrunk.

3.6   Information of Canonical Targets

Canonical targets are often used for modeling the backscattering of natural targets [Käh92]. This is basically due to the fact that their scattering behaviour can be calculated and that the scattering and RCS matrices can be evaluated in close form [RBSK70]. There are several classes of those targets; a main distinction is the number of bounces that the electromagnetic wave is subject to [CP96, Kro93]. The most important single bounce objects are metallic spheres and metallic discs[10] [WK91]. Double bounce targets are usually made of two metallic plates, the most common example is the dihedral or di-plate reflector.

3.6.1   Distributed Spheres

The RCS matrix for a single perfectly conducting sphere under the condition, that the radius is bigger than the wavelength may be approximated as [RBSK70]

$$\underline{\sigma}_{\text{Sphere}} = \pi r^2 \begin{pmatrix} 1 & 0 \\ 0 & 1 \end{pmatrix}. \qquad (3.19)$$

---

[10]Corresponding to a sphere with a radius $r \to \infty$

Assuming a Rayleigh distribution [BS89, Kro88a] for the radius,

$$
p_{|\mathbf{r}|}(r) = \begin{cases} 0 & \text{if } r < 0 \\ \frac{r}{\sigma^2} e^{-\frac{r^2}{2\sigma^2}} & \text{if } r \geq 0 \end{cases} \tag{3.20}
$$

the distribution for the hh-term of the RCS matrix follows as

$$
p_{\underline{\sigma}}^{hh}(r) = \begin{cases} 0 & \text{if } r < 0 \\ \frac{1}{2\pi\sigma^2} e^{\frac{-r}{2\pi\sigma^2}} & \text{if } r \geq 0 \end{cases} \tag{3.21}
$$

and it is exponentially distributed. Calculating the entropy for such a distribution, the occurring integral can be solved analytically and the entropy is

$$
\begin{aligned}
H(hh) &= \log_2(2\pi e) + 2 \log_2 \sigma \\
&\approx 4.094 + 2 \log_2 \sigma \quad \text{[bit]}.
\end{aligned} \tag{3.22}
$$

The conditional entropies for the polarisation combinations result as

$$
H(vv|hh) \equiv 0 \tag{3.23}
$$

and

$$
H(hv|hh, vv) \equiv 0. \tag{3.24}
$$

Hence, independently of the coherence of the data, the polarimetric gain of this target is

$$
g_{hh} = g_{vv} \equiv 0 \tag{3.25}
$$

whereas the gain with respect to the cross polarised channel is

$$
g_{hv} = \infty. \tag{3.26}
$$

These results show, that for a better understanding of data on spheres, polarimetry is of no use. By the right choice of the single polarisation channel all possible information on the target is already extracted. This phenomenon has already been used for a long time in detecting targets which are hidden by precipitation [UMF81, UMF82, UMF86, Sko81]. Assuming spherical rain drops, a polarimetric radar receives no information on these rain drops in the cross-polarised channels. Hence, all information in the cross-polarised
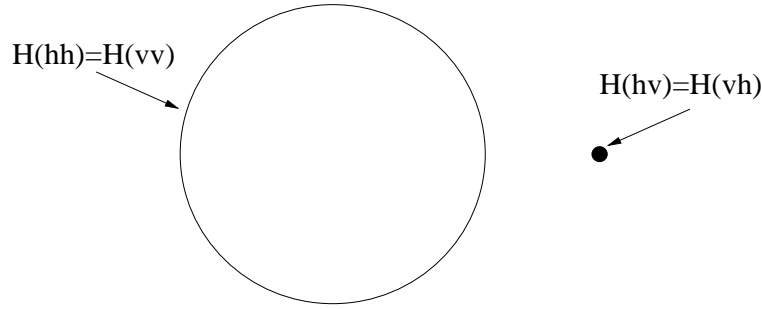
Figure 3.8: Visualisation of the entropy for spheres

channels is information of the target. Whereas in the co-polarised channels, the target may be hidden by rain.

In analogy to figure 3.4, the entropy situation of a target composed of conducting spheres is visualised in figure 3.8. It can be observed, that the whole information content is in either of the co-polarised channels and that none of the cross polarised channels contains any information[11].

3.6.2 Randomly Oriented Dihedrals

Dihedrals are widely used as calibration targets [RW86, WK91]. Beyond this application, many man made structures may be modeled by using dihedral structures [Kro93]. This is due to the fact that 90º angles usually do not appear in nature, whereas most man made targets are composed of them. Typical dihedral like targets to be detected by radar satellites are buildings, where the dihedral is formed by the 90º angle between the ground and the upright walls of the building.

Assuming a target with uniformly distributed dihedrals, the scattering matrix of each dihedral being oriented in α-direction can be approximated as [RBSK70]:

$$\mathbf{S}_{\text{Dihedral}} = \frac{k_0 \, a \, b}{2\pi} \begin{pmatrix} -\cos(2\alpha) & \sin(2\alpha) \\ \sin(2\alpha) & \cos(2\alpha) \end{pmatrix} \tag{3.27}$$

where a is the height of a wing and b is the length of the central axis of the of the dihedral according to figure 3.9. The distribution function for this

---

[11]Identical to this analysis is the analysis for the polarimetric information of a trihedral corner-reflector.
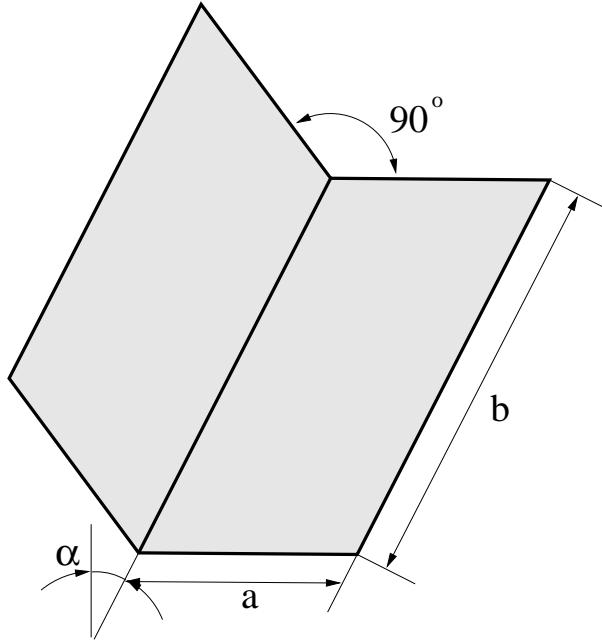
Figure 3.9: Dihedral oriented in α-direction

angle α is

$$p_{|\alpha|}(\alpha) = \begin{cases} \frac{1}{\pi} & \text{if } 0 \leq \alpha \leq \pi \\ 0 & \text{else.} \end{cases} \tag{3.28}$$

This leads to a distribution function of the elements of the scattering matrix[12]

$$p_{\mathbf{s}}(\alpha) = \begin{cases} \frac{1}{\pi\sqrt{1-\alpha^2}} & \text{if } -1 \leq \alpha \leq 1 \\ 0 & \text{else.} \end{cases} \tag{3.29}$$

Calculating the entropy based on this distribution function, an analytical solution cannot be found. The numerical solution yields

$$H(hh) = -\int_{-1}^{+1} \frac{\log_2 \frac{1}{\pi\sqrt{1-\alpha^2}}}{\pi\sqrt{1-\alpha^2}} \, d\alpha \approx 0.651 \, [\text{bit}]. \tag{3.30}$$

The conditional entropies can be calculated in the same manner, the results are

$$H(vv|hh) \equiv 0 \tag{3.31}$$

---

[12]The distribution is equal for each polarisation combination, as $\sin\left(\cos^{-1}(\alpha)\right) = \cos\left(\sin^{-1}(\alpha)\right) = \sqrt{1-\alpha^2}$

and
$$H(hv|hh, vv) = H(hh). \tag{3.32}$$

This allows the determination of the polarimetric gain

$$g_{hh} = g_{vv} = g_{hv} = \frac{H(hv|hh, vv)}{H(hh)} \equiv 1. \tag{3.33}$$
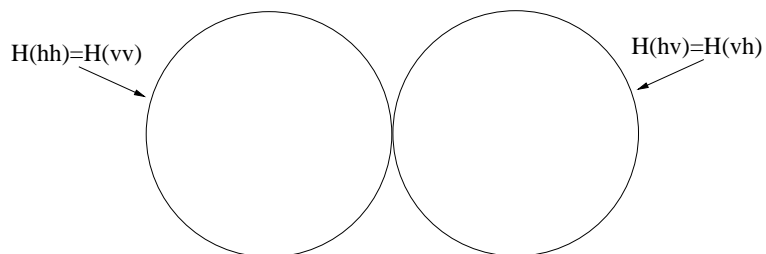
Figure 3.10: Visualisation of the entropy for dihedrals

The entropy situation is visualised in figure 3.10. It can be observed, that half of the information content is in either of the co-polarised channels and that the other half of the information is to be found in the cross polarised channel.

Though this model includes neither any coherence between the single scattering matrices, nor noise that corrupts the signal, the coherence matrices may be calculated. Yet, the outcome of this calculation is not significant due to the above mentioned constraints. From the coherence matrix the eigenvalues can be determined. The result of this calculation is $\lambda_1 = \lambda_2 = \frac{1}{2}$ and $\lambda_3 = 0$. This gives an entropy of $H = \log_3 2 = 0.63$. The coherence for the single channel is $h = \frac{e}{2} \log 2 = 0.94$. Therefore the coherence correction factor is 6.37. This high correction factor is due to the fact that the average signal energy is constant for the whole scattering matrix, whereas it is fluctuant for any single polarisation.

3.6.3 Random Scatterers

Another important class of scatterers are random objects. Scattering from leaves in a tree may be considered as an example of this class. Such random scatterers are widely used in simulations of volume scattering, where a layer

of randomly oriented scatterers represents the orientation of the leaves or needles in a forest.

As no preferred scattering direction is assumed, these random scatterers require reflection symmetries in any direction. Hence, for a description of such a medium, a single value for the density is sufficient. The scattering matrix of such a medium, needs to fulfill the following condition:

$$\underline{\sigma}_{\substack{\text{Random} \\ \text{scatterer}}} \equiv \mathbf{R}^{-1} \cdot \underline{\sigma}_{\substack{\text{Random} \\ \text{scatterer}}} \cdot \mathbf{R} \tag{3.34}$$

where $\mathbf{R}$ is a rotation matrix according to (C.1) In order to fulfill this condition, the scattering matrix needs to be of the form

$$\underline{\sigma}_{\substack{\text{Random} \\ \text{scatterer}}} = \begin{pmatrix} \alpha & 0 \\ 0 & \alpha \end{pmatrix} \tag{3.35}$$

where the scattering value α describes the intensity of the backscattering. This backscattering intensity is assumed to be normal distributed

$$p_{|\alpha|}(\alpha) = \frac{1}{\sqrt{2\pi}\sigma} \, e^{-\frac{(\alpha-\alpha_0)^2}{2\sigma^2}}. \tag{3.36}$$

this leads to an entropy for the co-polarised channels of

$$
\begin{aligned}
H(hh) &= \int_{-\infty}^{\infty} \frac{1}{\sqrt{2\pi}\sigma} \, e^{-\frac{(\alpha-\alpha_0)^2}{2\sigma^2}} \log_2 \left(\sqrt{2\pi}\sigma \, e^{\frac{(\alpha-\alpha_0)^2}{2\sigma^2}} \right) \, d\alpha \\
&= \frac{1}{2} \log_2 \left(2\pi e \right) + \log_2 \sigma \\
&\approx 2.047 + \log_2 \sigma \quad [\text{bit}]
\end{aligned} \tag{3.37}
$$

and to conditional entropies of

$$
\begin{aligned}
H(vv|hh) &\equiv 0 \tag{3.38} \\
H(hv|hh, vv) &\equiv 0. \tag{3.39}
\end{aligned}
$$

As in the previous case of randomly distributed spheres, the polarimetric gain with respect to the co-polarised channels is zero

$$g_{hh} = g_{vv} \equiv 0 \tag{3.40}$$

and the polarimetric gain with respect to the cross-polarised channels is infinity.

$$g_{hv} = \infty. \tag{3.41}$$

These results show, that the use of polarimetry in detecting a layer of random scatterers is of no help. Actually, as a target of randomly distributed scatterers can be described with a single variable only, the density of the distribution, and as this variable already has been extracted with a non-polarimetric (co-polarised) radar, no other information about the target exists. Hence, the use of other polarisations cannot give any additional information. The visualisation for the entropy is analog to figure 3.8.

3.7   Special Cases

In the calculation of the local polarimetric gain, several special cases need to be considered. This special consideration arises from the fact, that entropy is adequate for describing stochastic processes. If the process is deterministic, the entropy is zero, if the process is random, the entropy is maximum.

3.7.1   The Homogeneous Noise-free Area

Considering a homogeneous area without any influence of noise, all individual scattering matrix elements are constant, $S_{hh} = S_{hh}^0$, $S_{hv} = S_{hv}^0$ and $S_{vv} = S_{vv}^0$. Therefore the entropy of all polarimetric channels is equal to zero, $H(hh)^0 \equiv 0$, $H(hv)^0 \equiv 0$ and $H(vv)^0 \equiv 0$. However, this entropy of zero does not imply also a polarimetric gain of zero, a fact that underlines that a homogeneous area might very well have a distinct polarimetric radar signature. Assuming an equal noise level N on all three polarimetric channels, the scattering matrix elements converge with a decreasing noise level according to

$$\lim_{N \to 0} S_{ij} = S_{ij}^0 \quad \forall i, j \in \{h, v\} \tag{3.42}$$

and consequently converge the entropies with

$$\lim_{N \to 0} H(hh) = 0$$
$$\lim_{N \to 0} H(vv|hh) = 0$$

$$\lim_{N \to 0} H(hv|hh, vv) = 0$$

$$(3.43)$$

The calculation of the polarimetric gain results in

$$g^0 = \lim_{N \to 0} \frac{H(vv|hh) + H(hv|hh, vv)}{H(hh)}. \qquad (3.44)$$

In general, this polarimetric gain g^0 is greater than zero[13]. Its value depends on the decreasing rate of the involved entropies, for equally decreasing rates results $g^0 = 2$.

This behaviour can be observed in figure 3.11. This plots is a simulation of the dependency of the polarimetric gain on the signal to noise ratio. As the noise level approaches zero the polarimetric gain clearly converges to 2.

3.7.2 White Noise

The antipode to the above described case of a homogeneous and noise-free area is the of white noise. As white noise maximises the entropy, all the entropies involved in the calculation of the polarimetric gain are maximum, $H(hh)^{max}$, $H(vv|hh)^{max}$ and $H(|hv|hh, vv)^{max}$. At maximum entropy, a data element of length n [bit] as an entropy of n [bit]. Hence the polarimetric gain of white noise results as

$$g^{noise} = \lim_{N \to \infty} \frac{H(vv|hh) + H(hv|hh, vv)}{H(hh)} = 2. \qquad (3.45)$$

This behaviour can be observed as well in figure 3.11. On the left side of the plot, the signal to noise ratio is negative, representing a noise level superior to the signal level. It can be noticed in the simulation, that as the noise level increases, the polarimetric gain approaches 2.

3.7.3 Two Homogenous Areas

Another interesting case is the case of two neighboring homogeneous areas. Each of those areas shall have a distinct polarimetric response. As stated in the subsection 3.7.1, two homogeneous areas have polarimetric gains of g^1

---

[13]Only for $H(vv|hh) \equiv 0$ and $H(hv|hh, vv) \equiv 0$ results $g^0 \equiv 0$
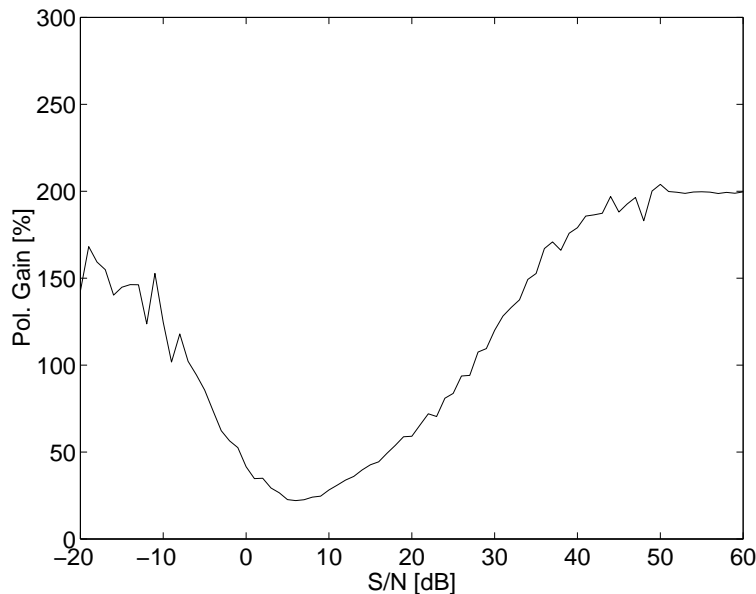
Figure 3.11: Simulation of the influence of noise on the polarimetric gain

and g^2, respectively. In general, but not necessarily g^1 is different from g^2. Each time, the data elements involved in the calculation of the polarimetric gain contain elements of both areas, the entropy will increase, as the data elements are now more different to each other than on the homogeneous area. This leads to a polarimetric gain g^{border}. Usually this gain g^{border} is higher than the gains of the homogeneous areas g^1 and g^2, as the conditional entropies will increase stronger with a higher rate than the reference entropy.

3.8   Calibration Influence

In order to extract the maximum information of polarimetric radar data, the data has to be calibrated thoroughly [Fre92a, DEFvZ92]. Such calibration procedures for polarimetric data differ a lot from non polarimetric calibration, as not only the power level of a single channel must be adjusted, but also the phase differences between three channels. To do so, a variety of calibration procedures do exist, based on three different approaches: cooperative, active targets, passive canonical targets and based on the statistics of the data.

From the information theory point of view, the calibration needs to com-

pensate for the influences of the up- and downlink, as shown in figure 3.3[14] [Pap91].

An important point to stress here is the fact that on all propagation paths, not a two-dimensional vector is transmitted and a four-dimensional vector is received, but sequentially both polarisations are transmitted and a two-dimensional vector is received[15]. Based on this consideration, the propagation may be drawn according to figure 3.12, where the dashed lines
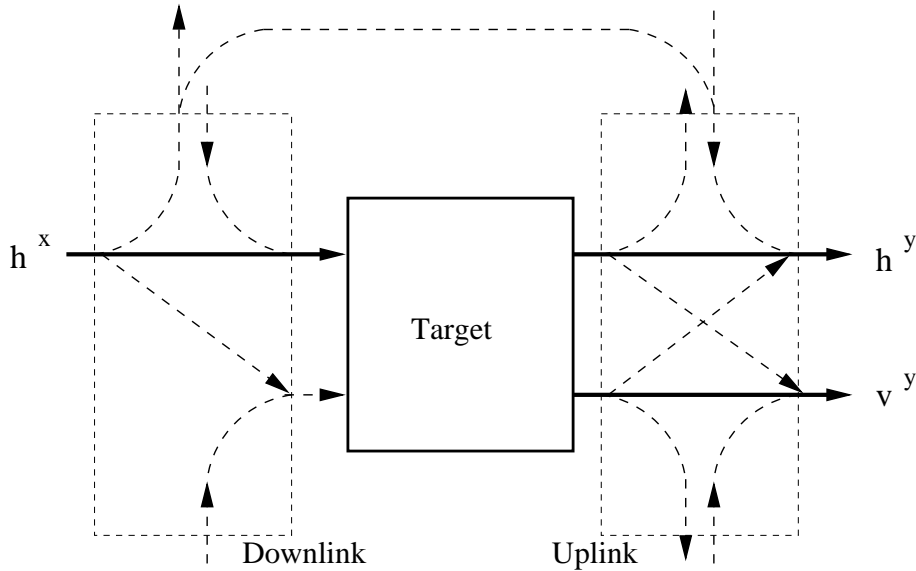
Figure 3.12: Entropy influences during propagation

are noise and depolarisation. The calibration needs to minimise the influences of these effects.

---

[14]For the general case of a not space- or air-borne radar, all propagation influences need to be compensated by the calibration

[15]The separation for the sequence may not only occur in time, but also in frequency

Chapter 4

The Polarimetric Radar Sensor

The theoretic derivation of the concept of the polarimetric gain necessitates an experimental verification. In order to be able to verify the results of chapter 3, a full polarimetric radar sensor has been developed. Beyond this verification, the radar sensor, called *LISA* (*LI*near *SA*r) serves also as prototype for several innovations, such as the K_u-band frontend or the circular synthetic aperture with a parallelogram shaped arm.

4.1 Description of the Radar

The *LISA* radar sensor is a scatterometer with synthetic aperture for outdoor use. It provides radar images of the environment in the upper L-band, S-band, the lower C-band and in K_u-band. These radar images complement the coverage from radar remote sensing satellites (such as ERS 1/2), as the use of *LISA* allows a continuous observation of objects. The technology is a direct application of the knowledge gained in the European Microwave Signature Laboratory (EMSL) of the JRC [Sie93]. Actually, the system concept and the data structure is the same, such that for system operation and signal processing, the existing programs for the EMSL needed only slight modifications. The *LISA* instrument is designed as versatile as possible, in order to provide a prototype instrument for many different applications. This is expressed not only in the large available bandwidth, but also in the fact, that the instrument (having two separate receivers) is able to make measurements in real-time polarimetric-on-receive mode or single polarisation single-pass-interferometric mode.

The instrument comprises two synthetic apertures for the creation of high resolution three-dimensional data. In addition to a conventional linear rail based synthetic aperture, a circular aperture [RTS97] with a special parallelogram shaped arm [Rud99b] has been designed. For the extension of the usable frequency range, a special high frequency frontend is used.

The areas of application for the *LISA* instrument are sub-surface imaging for humanitarian demining, polarimetric imaging of vegetation for biomass measurements, interferometric measurements of natural hazards, such as landslides and avalanches, and the interferometric monitoring of large man-made structures [Tar99].

For the outdoor measurements the instrument is located in a trailer. This trailer also allows the transport on the road and an eventual air-lift. Figure 4.1 shows a design of the trailer.

4.2   Radio Frequency Section

The radar in the *LISA* instrument is a stepped frequency CW-radar. A synthesizer generates a single (CW) frequency, this frequency is transmitted and the scattered response of a target is received. This approach implies a great simplicity for the hardware design. There is no need for a pulse generator, neither for a wide band receiver. The receiver has a very high amplitude sensitivity, as it is very narrow band. The draw-backs of such a radar type are a high level of transmitter signal leakage. As the transmitter and the receiver are always simultaneously active, a strong signal is directly coupled from the transmitter into the receiver. This signal usually exceeds the received signal of any target by several orders of magnitude [UE90]. Though it is possible with range processing [Men91] to discriminate this signal from target echoes, this leakage significantly reduces the dynamic range of the receiver. This is due to the sidelobes of the fast-Fourier-transform [KK92], that is used to convert the signal from frequency-domain into time-domain. Even with the use of sophisticated windowing functions, this sidelobe level is typically on the order of -60 dB with respect to the mainlobe [KK92][1]. In order to reduce the transmitter leakage as far as possible, two separated antennas are used

---

[1]A further reduction would be possible, but is not necessary, as it is sufficient to bring the sidelobe level under the noise level
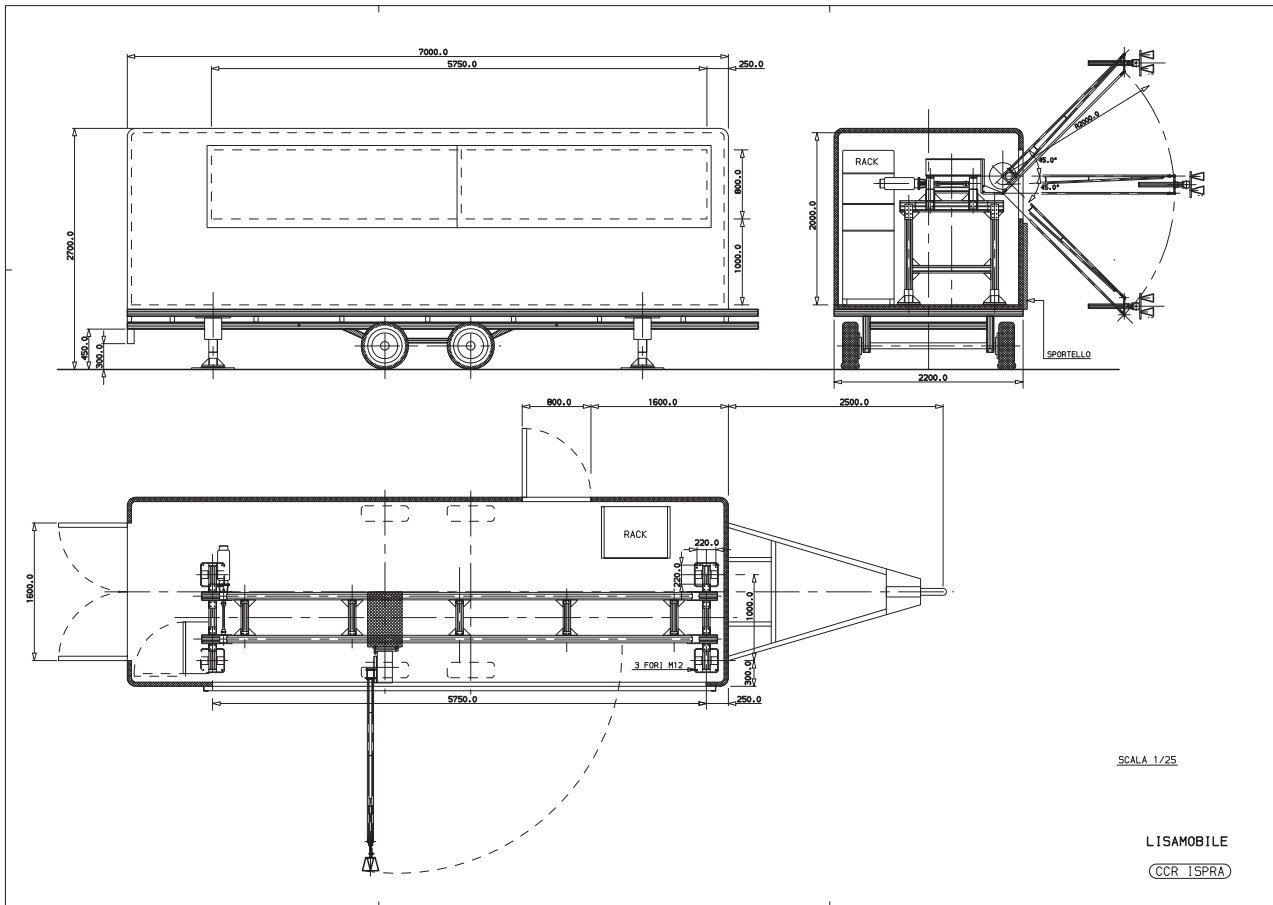
Figure 4.1: Drawing of the *LISA*-instrument

for transmission and reception[2]. Another problem is the time for generating a frequency sweep. As each frequency is generated separately, the sweeper has to wait at each frequency for a phase lock of the signal and to integrate each received single frequency signal for a sufficient time period. Targets that move significantly during the time that is needed to sweep over all frequencies will remain unfocussed after the range processing.

The radio frequency equipment is build with off-the-shelf microwave and standard test components. Figure 4.2 shows a diagram of the RF-equipment.

The heart of the RF-equipment is a Hewlett Packard vector network-analyser (HP-8753D). This vector network-analyser includes a sweeper for

---

[2]For systems with a single antenna only, hence separating transmission and reception with a circulator, the transmitter leakage is caused by the mismatch of the antenna.
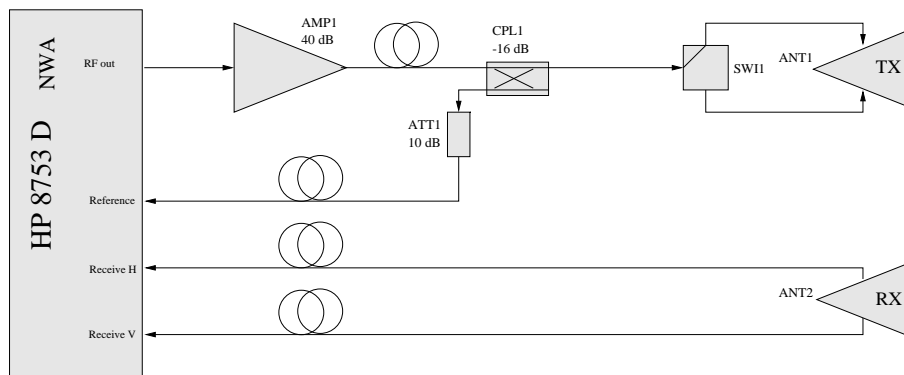
Figure 4.2: Diagram of the RF components
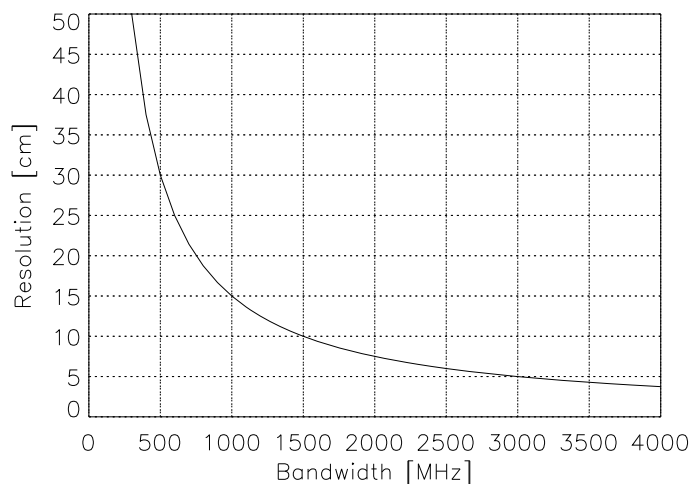
Figure 4.3: Resolution in range

frequency generation and two coherent receivers. The sweeper operates in a frequency range from 30 kHz to 6 GHz. For the *LISA* instrument the range is restricted to a maximum band from 2 GHz to 6 GHz. The frequency range Δf determines the achievable resolution in range as already stated in (2.52). Furthermore the number of points used in the sweep is responsible for the avoidance of aliasing in range according to (2.53). The dependency of the possible resolution in range is shown in figure 4.3.

For ensuring a phase-lock of the synthesizer and for a correct down-conversion of the received signals, a reference signal is fed into the network

Symbol	Explanation	Typical value	Typical Value [dB]
n	Number of averages	1	0
P_t	Transmission power	1 W	0 dBW
G_t	Transmit antenna Gain	6.3	8 dBi
G_r	Receive antenna Gain	6.3	8 dBi
λ	Wavelength	0.05 m	-13 dBm
			-13 dBm
σ	Radar-cross-section	1 m^2	0 dBsm
k	Boltzmann's constant	$1.38 \cdot 10^{-23} \frac{Ws}{K}$	$\left.\begin{array}{l}\\\end{array}\right\}$ $(-204\,\text{dBW/Hz})$
T_0	Standard temperature	290 K	
$(4\pi)^3$		1984	(33 dB)
F_n	Noise figure of the receiver	100	(20 dB)
Δf	Receiver bandwidth	333 Hz	(25 dBHz)
$(S/N)_1$	power-ratio for single-detection	10	(10 dB)
L_s	System losses	4	(6 dB)
	R_{max}^4		100 dBm^4
R_{max}	Maximum detection range	312 m	25 dBm

Table 4.1: Variables in the radar-equation

analyser. This reference signal has the same frequency as the transmitted signal. In the *LISA* setup, this signal is taken directly before the antennas. Thus all influences of the power amplifier on the signal phase stability are compensated.

In order to estimate the efficiency of the instrument, the values for the radar equation (2.48) are given in table 4.2:

The two coherent receivers receive simultaneously two signals, which in our case are the two polarisations (horizontal and vertical). In the non-polarimetric interferometric mode, this allows the creation of single pass interferograms, avoiding decorrelation caused by temporal changes of the target area. Both receivers detect both the in-phase signal and the quadrature signal.

4.2.1 The K$_{\mathrm{u}}$-band Frontend

A K$_{\mathrm{u}}$-band frontend has been developed and realized for the LISA outdoor radar scatterometer. All properties of the *LISA* instrument remain unchanged. It preserves its 3-D imaging capability and the K$_{\mathrm{u}}$-band-data

can be readily processed with the existing signal processing programs. The frontend provides a transmitted frequency from 15 GHz to 16 GHz or from 16 GHz to 18 GHz, depending on the choice of the circulator C1.

This frontend has been realised with off-the-shelf RF components. The sensitivity of the frontend is comparable to the sensitivity of the network-analyser. Compared with the original frequency band, the frontend allows a significantly increased resolution in cross-range.

Figure 4.4 shows a diagram of the frontend. As local oscillator providing a fixed frequency of 14 GHz an existing Hewlett-Packard 8340B synthesizer serves. The network-analyser operates at an intermediate frequency (IF) of 1 to 2 GHz or with a different circulator C1 at an IF from 2 to 4 GHz.

The local oscillator signal is equally divided into four parts, using a cascade of two-way power dividers, then it is used to drive four mixers, one for up-converting the IF output-signal of the network analyser, one for down-converting the reference signal to the IF level and one for down-converting each polarisation of the receive signal to the IF level.

After the up-conversion mixer M1, a high-pass-filter with a cut-off frequency of 14.2 GHz allows only the upper side-band of the up-conversion to pass. The lower side-band and the LO carrier frequency are cut off. This signal is then amplified by an ultra-wideband amplifier to a level of +20 dBm. A reference signal is coupled out and down-converted. This reference signal is needed for ensuring the phase lock of the network-analyser IF signal. The same down-conversion takes place also for the received signals of both polarisations. As the upper side-band after the down-conversion is separated by twice the LO frequency, hence 28 GHz, no filtering is required, as the input filters of the network-analyser will reject such high frequencies. Three circulators are used for guaranteeing the signals to propagate in the desired directions.

The frontend has been realised with two independent receiving channels, in order to preserve the capabilities of a simultaneous reception for two different polarisations or of using the two reception channels for single-pass interferometry.

Figure 4.4: Diagram of the RF components

4.3 Cross-Range Resolution

For providing resolution in cross-range, the *LISA* instrument has two synthetic apertures, a horizontal linear aperture, projecting the radar data onto a horizontal plane and a vertical circular aperture, projecting the data onto a vertical plane. The combined use of both apertures allows the creation of high resolution three-dimensional radar images [RTS97].

4.3.1 The Linear Aperture

The linear synthetic aperture is created by moving the antenna with a sled in a linear motion parallel to the ground. Hereby, the antennas are pointed perpendicular to the motion. A synthetic aperture signal processing [Men91] of the side looking data-takes, allows the creation of a resolution in azimuth, parallel to the motion of the sled.

For moving the sled constantly a rail system exists. The rail system allows a maximum excursion of 5 meters.

The obtainable cross-resolution hereby depends on the transmit wavelength λ, the target distance R and the maximum excursion of the sled, hence the length of the synthetic aperture L, according to (2.55). Figures

Figure 4.5: Resolution of a linear SAR in 100 m distance
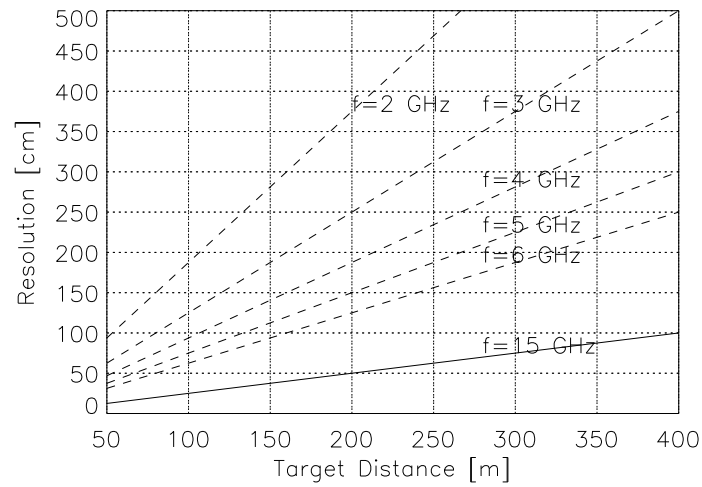
Figure 4.6: Resolution of a linear SAR with 4 m synthetic aperture

4.5 and 4.6 show the obtainable resolutions for the instrument. Hereby the dashed lines indicate the resolution for the radar operating without the K_u-band frontend and the solid lines show the improvement in azimuth resolution obtained by the use of the frontend.
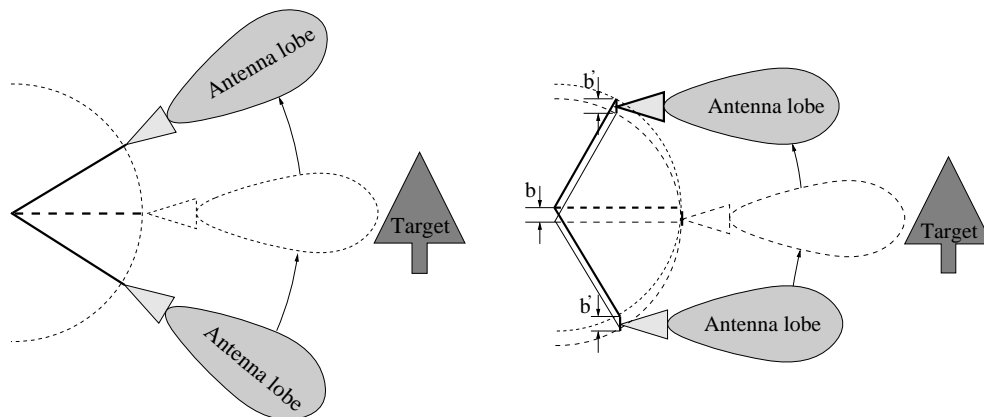
Figure 4.7: Geometry for a conventional circular SAR and a circular SAR with a parallelogram arm

4.3.2 The Circular Aperture

Similar to the linear aperture, the circular aperture is also used to generate resolution in cross-range. As the rotator is mounted upright, the resulting cross-range is perpendicular to the cross-range of the linear aperture. Hence resolution in elevation is generated.

Conventional circular aperture SARs [Kla89, BDPS96] provide several advantages over linear aperture SARs. A first advantage are limited efforts and costs for the mechanical parts, as the linear drive can be replaced by a ordinary stepped motor. A second advantage is the reduced motion of the RF-cables, as they are bended only at the pivot and do not need to be moved with the sled. This improves the phase stability of the measurements. A collateral effect is a reduced cable length with respect to a linear SAR. However, conventional circular SARs suffer a problem as the antenna lobe is being moved relatively fast over the target, causing a severe limit to the usable aperture. This is illustrated in the left side of figure 4.7. For real antennas, this behaviour causes also depolarisation problems, as the polarisation purity of antennas generally fades as the antenna is not directed with the maximum of the main lobe towards the target.

A solution that prevents the migration of the real aperture of the antenna over the target, while preserving a long synthetic aperture and preserving the indubitable advantages of a circular aperture over a linear aperture is the mount of an additional arm of the same length as the arm holding the

antennas, whose pivot is separated by a baseline b. This baseline b gives a reference for a baseline b$^{'}$ at the far end of either arms. The far baseline b$^{'}$ will always be parallel to b. antennas mounted fixed to the far baseline b$^{'}$ will always point in the same direction, no matter what angle β the arms are rotated around the respective pivots. This behaviour is illustrated in the right side of figure 4.7 and a detailed drawing of the mechanical solution is shown in figure 4.8.

In this drawing, the motion of the arms and the fixed pointing of the far baseline b$^{'}$ with the antennas can be detected clearly. The length of the arms is chosen to be two meters and the maximum rotating angle is more than 90°. This allows an excursion of about three meters.

The cross-range resolution of such a parallelogram shaped synthetic aperture radar is

$$\delta^{\|} = \frac{\lambda\,R}{4\,A\,\sin\frac{\beta}{2}} \qquad (4.1)$$

where A is the length of the arm, β is the aperture angle of the circular aperture and R the distance between antenna and target.

It has to be noted, that (4.1) is only applicable for the case of equal excursions of the arm around the line pivot to target $\beta^{+} \equiv \beta^{-} \equiv \frac{\beta}{2}$. With unequal positive β^{+} and negative β^{-} rotation angles the resolution is

$$\delta^{\|} = \frac{\lambda\,R}{2\,A\,(\sin\beta^{+} + \sin\beta^{-})}. \qquad (4.2)$$

In order to avoid aliasing in elevation, the circular aperture has to be sampled according to the theorem of Nyquist [Wen89] with at least

$$n^{\|} \geq \frac{4\,A\,\left(\sin\beta^{+} + \sin\beta^{-}\right)\sin\frac{\Theta}{2}}{\lambda} + 1 \qquad (4.3)$$

points[3], where a Θ is the 3-dB beamwidth of the antennas.

Figures 4.9 and 4.10 show plots of the achievable resolution in elevation. The dashed lines in these plots indicate the resolution for the basic radar configuration, hence the network-analyser only and the solid line indicate the resolution with the K$_{\mathrm{u}}$-band frontend.

---

[3]The formula assumes the stepsize to be smaller than a 90° phase shift per wavenumber k for the worst positioned target.
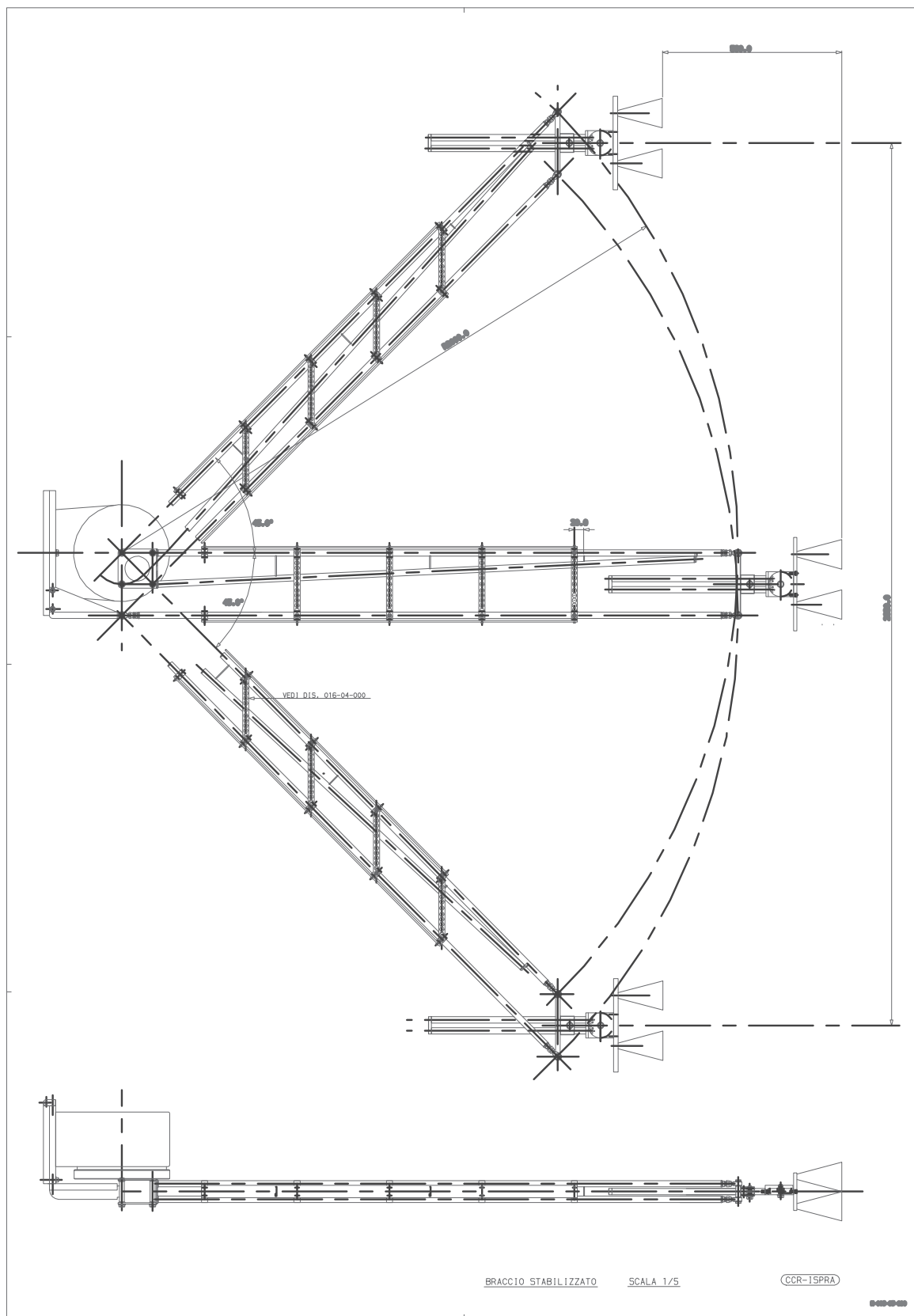
Figure 4.8: Drawing of the parallelogram shaped arm
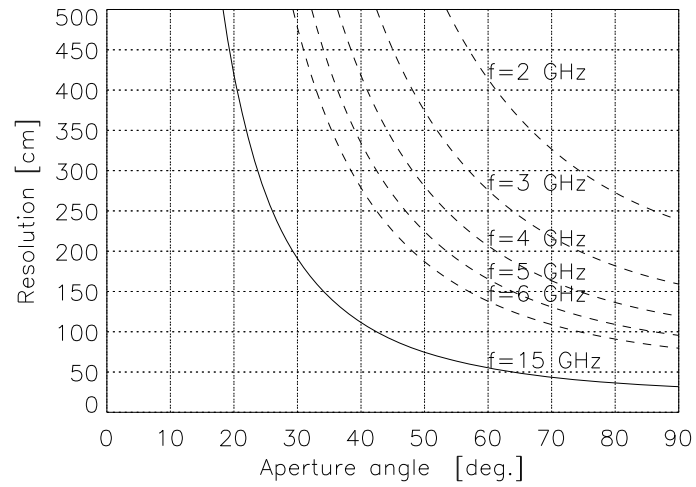
Figure 4.9: Resolution of a SAR with parallelogram shaped arm of 2 m length in 100 m distance
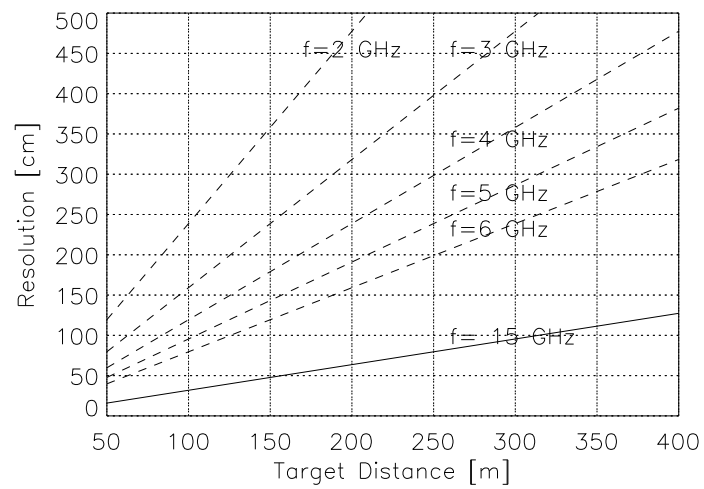
Figure 4.10: Resolution of a SAR with parallelogram shaped arm of 2 m length with a 90° synthetic aperture angle
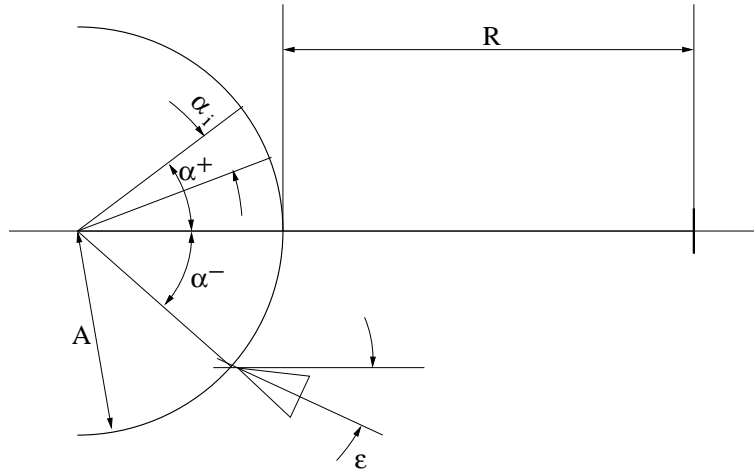
Figure 4.11: Geometry for the resolution

The antenna incidence angle can be adjusted with a joint on the far end of the arms. Thus the angle between the far baseline b' and the antenna pointing direction is changed. An adjustment of the antenna depression angle ε changes the available resolution in cross-range by a factor of

$$\delta^{//} = \delta^{\|} \, \frac{1}{\cos \varepsilon} \tag{4.4}$$

as the effective synthetic aperture is reduced with respect to a perpendicular antenna pointing. This is illustrated in figure 4.11.

Furthermore the antennas can be torn out by another 0.5 m. Such a variation remains without any influence to resolution. It is only of importance, when there are special requirements for the vicinity of the antenna to the target, as it happens for ground penetrating measurements.

Chapter 5

Verification

In this chapter, the concept developed in chapter 3 is applied to polarimetric radar data. With this application is underlined the presented concept of a first evaluation of the polarimetric information content in order to optimise the extraction of polarimetric radar information.

The choice of these data has been made in order to cover a wide range of different applications. These radar data originate from two measurements which have been done with the outdoor scatterometer *LISA*, presented in the preceding chapter. The definitions will also be applied to high resolution three-dimensional laboratory data. Afterwards polarimetric spaceborne data from the *SIR-C* experiment is analysed with regard to the polarimetric information content. Finally, the concept is applied to high resolution airborne polarimetric radar data from the German E-SAR system. In all these data the polarimetric gain of the data is calculated and its results are compared with traditional polarimetric signal processing algorithms.

5.1 Polarimetric SAR Experiment for Land-mine Detection

The detection of anti-personal mines is one problem where radar might play an important role in the near future [Oly98]. This is due to the fact that land-mines are difficult to detect with conventional means [Sie96, Sie98]. Whereas the diminishing metal content of landmines causes metal-detectors to operate at such a low detection threshold that the false-alarm rate becomes unaccept-

ably high, the capability of radar to detect dielectric inhomogeneities makes it theoretically a perfect instrument for detection of buried objects of any material. Radar polarimetry in particular is one of the major hopes for landmine detection, as the generally cylindric form of anti-personal mines causes special polarimetric properties of the backscattered signal [Sie96].

Measurement Set-up

In order to evaluate the information content of such polarimetric SAR measurements, a test series of experiments has been carried out. The experiments were performed at the test ground of the JRC in Ispra. Several types of mines were placed first on the surface. In a second test, these mines were buried to a depth, such that the detonator was just covered by sand. The experiment comprised twenty mines of five different types. The mines were laid down in such a manner that mines of the same type could be seen from the radar under different aspect angles and that the aspect angles were comparable between the different mine types. This was done in order to be able to evaluate the influence varying incidence angles. As reference targets, five metallic spheres were used. The reference targets were needed to compare their return signal with the signal returned by the mines. The surface of the test ground was divided into three different parts: grass, gravel and sand. A sketch of the set-up is shown in figure 5.1.

The experiment was run in a normal SAR-mode. The antennas were moved parallel to the target area while being ca. 2 m above the ground. Such a measurement geometry avoided the occurance of several problems. For instance, the specular reflection that often causes problems for ground penetrating radars can be avoided, also the coupling to the ground with its effects on the antenna pattern is no longer of concern. Furthermore, the creation of a SAR image, hence the compression in cross-range, might improve the detection possibility.

As stated before, one of the objectives of this experiment was to identify a mine by its polarimetric properties. Therefore the experiment was run in a full polarimetric mode. In table 5.1 is given a list of the measurement parameters.
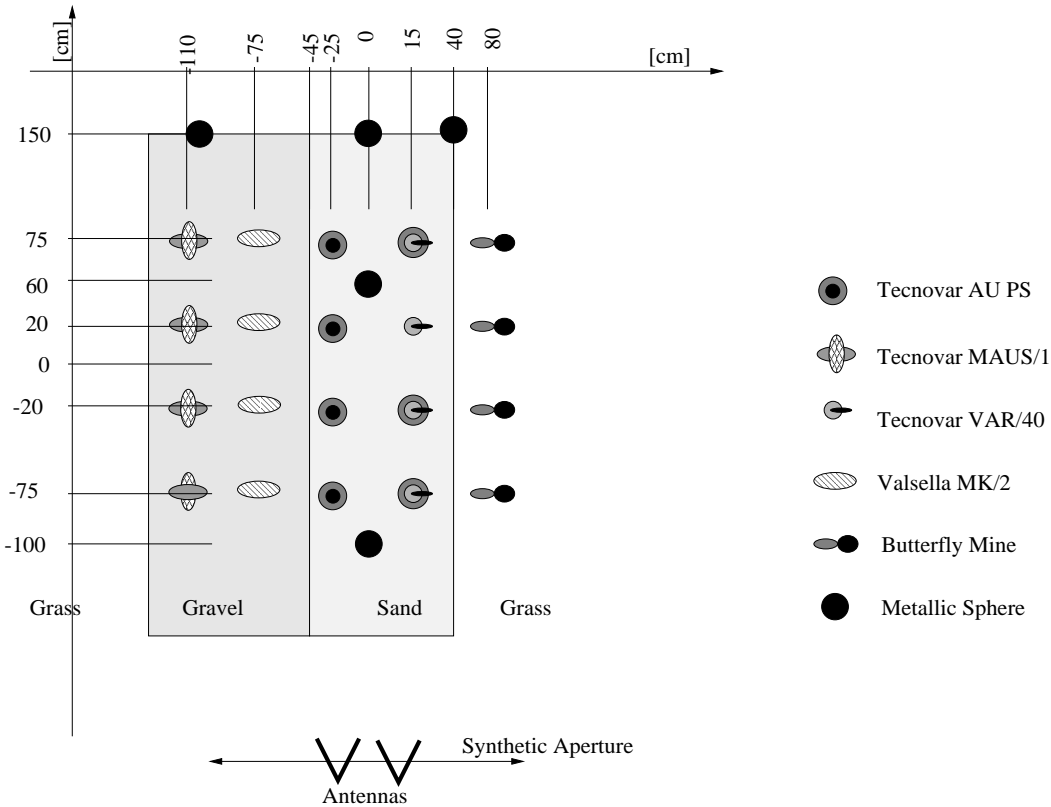
Figure 5.1: Sketch of the target for the landmine SAR experiment

SAR Amplitude Images

From these data SAR images have been created [FS94]. The resulting SAR images are shown in figures 5.2 and 5.3. The displayed SAR images show the hh-polarised data for both experiment set-ups. For a better interpretation of the image the positions of the mines are marked with a "x", and the positions of the spheres with an "o". These markings will be shown in all following images. For the given resolution cell size, which is in free space a rectangular of 64 by 61 square millimeters, an identification of the mines based on the shape of the mine is not possible. Under good conditions, a typical anti-personal mine would fill hardly more than three complete resolution cells. The mines used in this experiment were all of different size, the largest used mine was the "Tecnovar AU PS", with a diameter of 107 mm and a height of 47 mm plus 20 mm for the detonator. The smallest mines used were the "Tecnovar VAR/40" with a diameter of 80 mm and a height of 15 mm plus

Parameter	Value
Start frequency	2 GHz
Stop frequency	6 GHz
Frequency step size	10 MHz
Number of frequency points	401
Transmit polarisation	Horizontal and vertical linear
Receive polarisation	Horizontal and vertical linear
Transmit power	10 dBm
Linear aperture length	4000 mm
Aperture step size	25 mm
Number of aperture points	161
Incidence angle at 0/0	54.0°
Calibration distance	3250 mm
Calibration procedure	Disc, empty room, dihedral 0° and 45°
Resolution in range	64 mm
Resolution in cross-range	61 mm

Table 5.1: Summary of the measurement parameters for the landmine SAR experiment

25 mm for the detonator. All mines were without any metal content, as the detonators were removed from the mines[1].

In these images 5.2 and 5.3 most of the mines can be detected as long as they are surface laid. The detection of the buried mines is almost impossible without any prior knowledge of their positions. Furthermore, the buried mines appear displaced due to their true position. This effect is caused by the different velocity of the electromagnetic waves in the soil.

Polarimetric Properties of the Data

In order to evaluate the polarimetric information content of the data, the polarimetric gain for the data has been calculated. Figure 5.6 shows the histogram of the polarimetric gain. It can be noted, that this gain is very low. The average gain for the polarimetric information is in the order of 10 %. The maximum value hardly exceeds 30 %. Also the trend of both histograms

---

[1]Still the metal content of the detonators is limited to a very small metallic pin
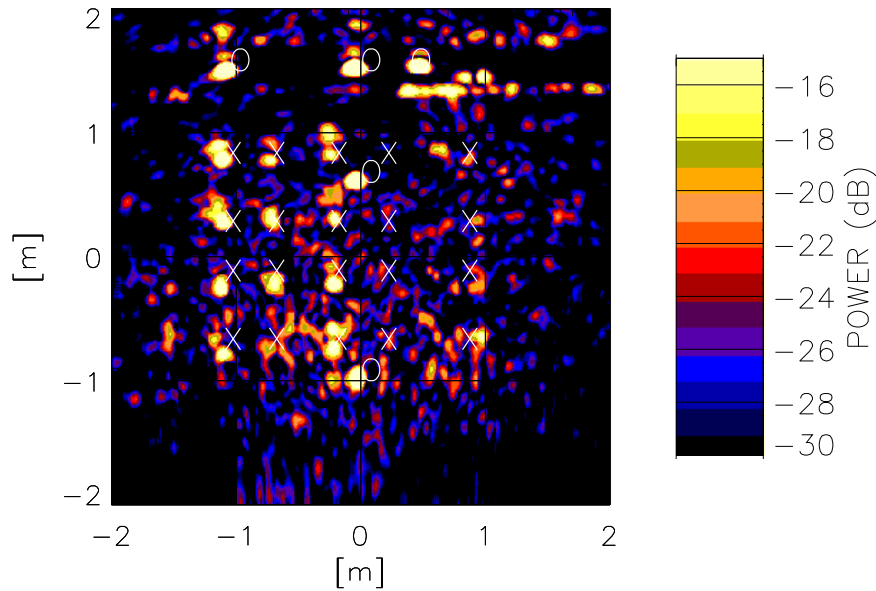
Figure 5.2: SAR image of the experiment. Surface laid mines, hh-polarisation

is very similar, so that a polarimetric property of the mines different to the polarimetric properties of the surface is not to be expected.

In order to verify this assumption, images of the polarimetric gain have been processed. These images are shown in figures 5.4 and 5.5, respectively.

Results of this Experiment

The interpretation of these images leads to the following conclusions:

- the polarimetric information of a mine on the surface is lower than the polarimetric information of the surface: in figure 5.4 most of the mines can be identified with prior knowledge of their positions by means of a very low polarimetric gain,

- the use of polarimetric radar might give advantages over a single po-larisation radar on the removal of the ground clutter rather than in the identification of the mine itself,
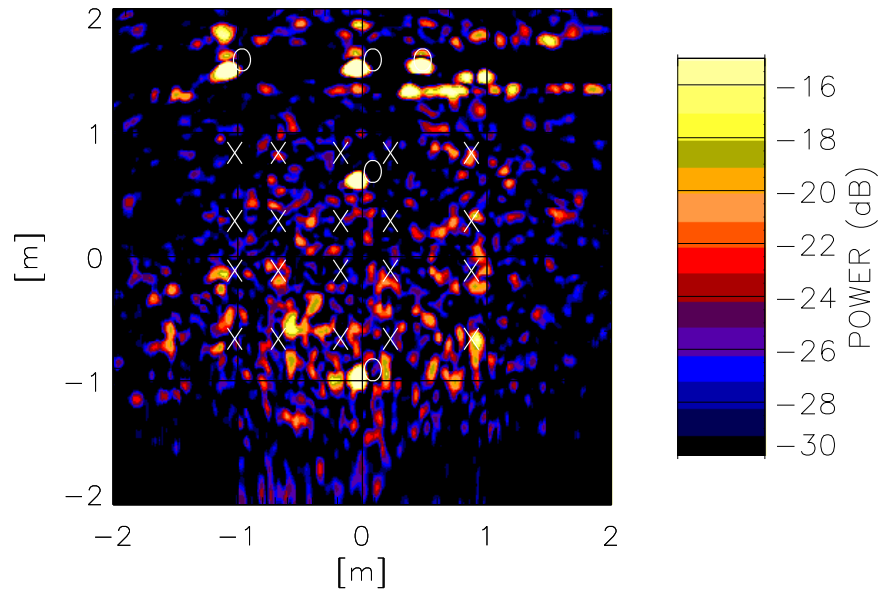
Figure 5.3: SAR image of the experiment. Mines buried, hh-polarisation

- the buried mines are very difficult to detect with the knowledge of a single polarised channel. Yet, radar polarimetry does not show any significant information content. The trend that the polarimetric gain is lower at positions of buried mines remains, but a classification based upon this result appears rather risky,

- the use of the polarimetric gain could help to analyse the image and to decide faster whether or not polarimetry is improving the analysis of the data. Furthermore it gives a clue that radar polarimetry might not be of significant help for detecting the single mine, but might be substantial for the removal of ground clutter. Thus improving the detection probability by reducing the number of false alarms.

Application of the Hilbert-scan

The automated classification of polarimetric data, based upon the H-α-algorithm, requires the calculation of the coherence. As stated in the pre-
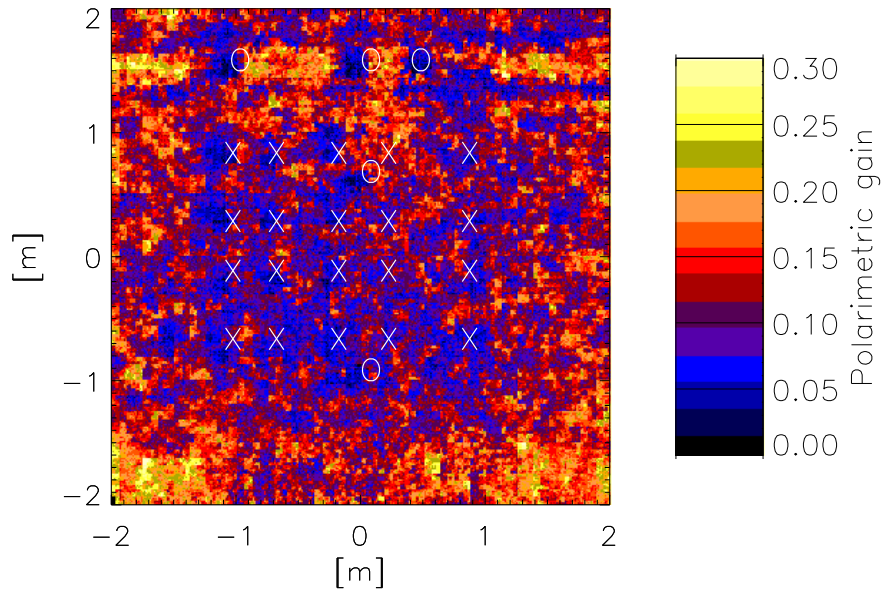
Figure 5.4: Image of the polarimetric gain, Surface laid mines

ceding chapter, the calculated coherence of two- or more-dimensional data depends on the path along which the coherence has been calculated. The Hilbert-scan maximises the coherence for normal distributed data [LZ86, Gil58]. For the experiment with the mines buried under the soil, is shown the distribution of the eigenvalues $\lambda_1, \lambda_2, \lambda_3$ in figure 5.7. On the left side is shown the histogram for the calculation with a conventional scan. The averaging was taken over 16 pixels, grouped in a box of 4 by 4 pixels. On the right hand side is shown the same histogram, for the eigenvalues of the coherence matrix, but with the ensemble-average being calculated along the Hilbert-curve over a vector of 16 elements. Though there is no visual difference between the histograms, a more detailed analysis reveals that the variance of the first eigenvalue λ_1 is diminished by 13 % to 17 %. The other two eigenvalues λ_2, λ_3 remaining practically unchanged. Such a decrease for the variance of the eigenvalues, causes the histogram to have a more pronounced mean-value. For polarimetric interferometry it has been shown [CP98] that
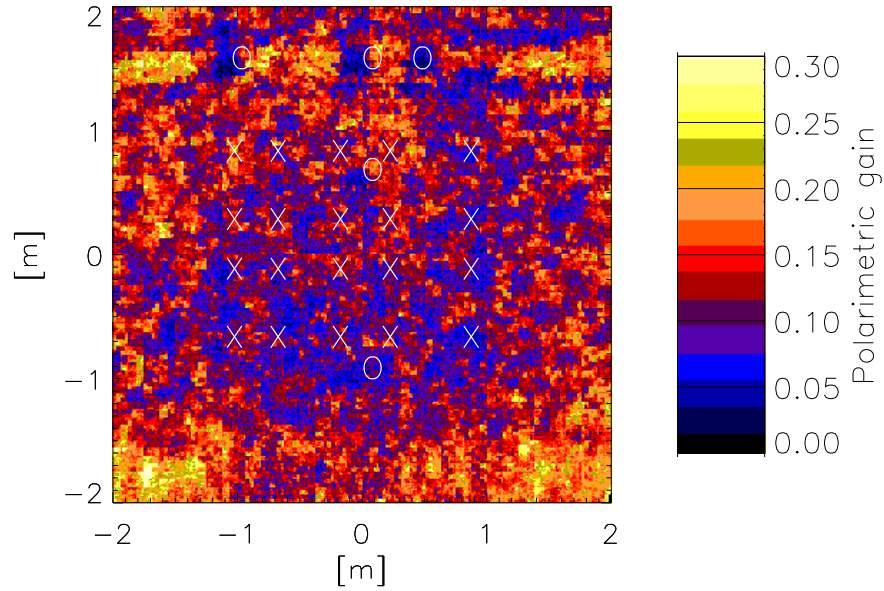
Figure 5.5: Image of the polarimetric gain, mines buried

less widely distributed eigenvalues will allow a more precise use of polarimetric interferometry. Figure 5.8 shows the equivalent histograms for the case of mines lying on the surface, the effect of narrowing the distribution of the first eigenvalue remains observable within a similar order of magnitude with regard to the data of the experiment with the buried mines.

The data of this experiment might not be suited for polarimetric interferometry, as none of the minor eigenvalues (λ_2 and λ_3) is as pronounced, as it is the dominant eigenvalue λ_1. Yet, the result shows that by use of an optimised scan, for calculation of the coherence matrix, the properties for further data processing can increase significantly.
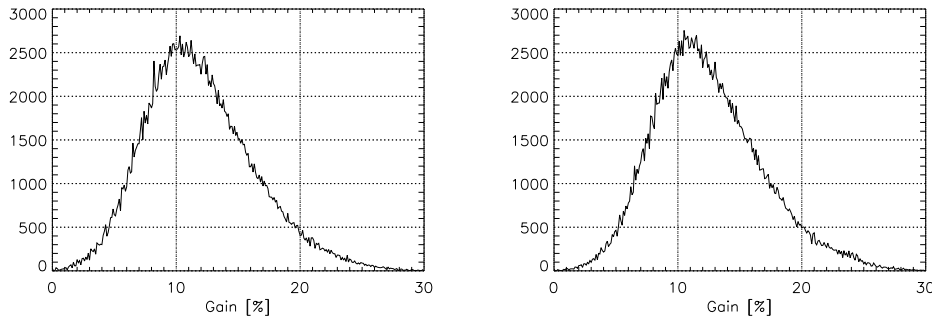
Figure 5.6: Histogram of the polarimetric gain. Surface laid mines (left), mines buried (right)
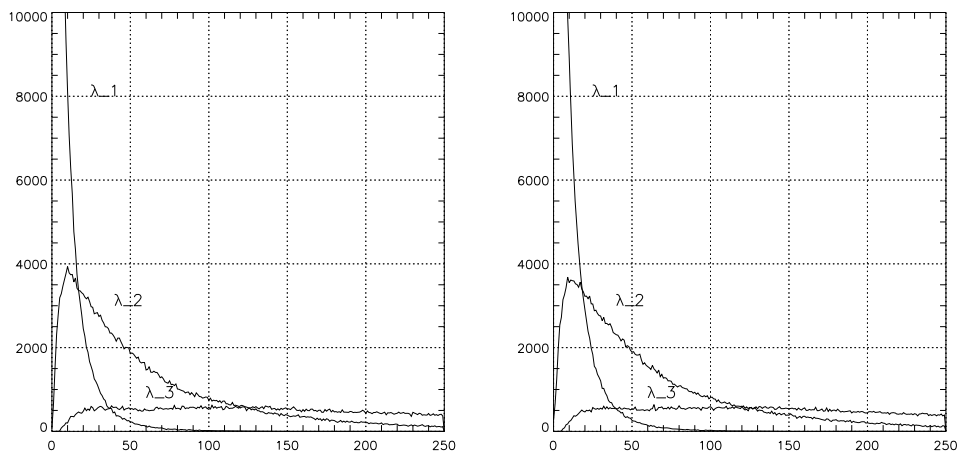
Figure 5.7: Histogram of the eigenvalues of the coherence matrix, for the measurement with buried mines. Hilbert-scan (left) and TV-like scan (right)

5.2 Interferometric Polarimetric SAR Experiment

The next data set is the result of a demonstration experiment for ground based SAR interferometry. The experiment was run in a full polarimetric measurement mode, though the emphasis was on interferometry [Tar99].

The scope of the experiment was to assess whether the use of synthetic aperture radar interferometry is a suitable means to detect and to monitor deformations in structures. With respect to conventional sensors, this approach would contain several advantages, such as the imaging capability and
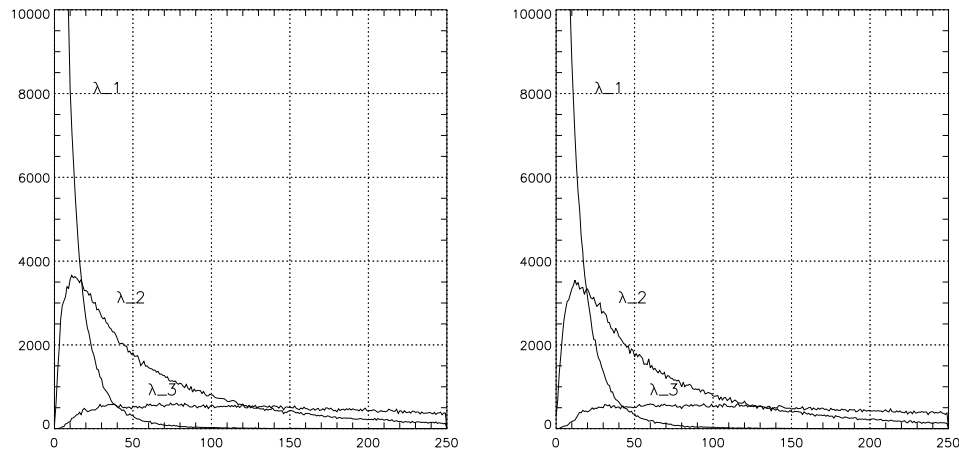
Figure 5.8: Histogram of the eigenvalues of the coherence matrix, for the measurement with surface laid mines. Hilbert-scan (left) and TV-like scan (right)

lesser sensitivity to specular reflections.

Experiment Set-up

The data has been collected using the outdoor portable SAR system *LISA* [Rud99a, RT99] of the Space Applications Institute. The target is the "Ridra-coli" barrage located in Romagna, Central Italy. This barrage is a double curved concrete structure. Its crest stands almost 100 meters above ground and it is about 400 meters long. At the base it has a depth of 28 meters and at the top of 7 meters. In the measurement arrangement the *LISA* system has been installed near the foot of the dam in order to be able to take radar images of approximately half of the structure, including the central upper portion and a part of the stable foundation rocks. Unfortunately the monitoring of the structure as a whole was not possible as the valley was rather narrow and no better suited position could be found. This resulted in a very wide-angular position for the radar. Figure 5.9 shows the position of the instrument with respect to the dam. The photo on the right side of figure 5.9 shows half of the dam and in the foreground the trailer with the *LISA* radar. It can be noticed that the target distance varies between 80 and 250 meters. Fully polarimetric measurements have been performed in

Figure 5.9: Top view of the test site, showing the measurement set-up. The dimensions of the *LISA*-instrument are exaggerated (left). Photo of the test-site (right)

the frequency band from 5.2 to 6. GHz using a synthetic aperture of about 4 m and exploiting the *LISA* scanning capabilities both in horizontal and vertical directions [RTS97, Rud99b]. In table 5.2 are summarised all measurement parameters.The 3D-capabilities of the instrument have not been explored, the synthetic aperture was either linear or circular. Measurements have been repeated periodically over a period from June to September, with a measurement repetition every 2 weeks, 7 measurement days in total.

Particular attention has been paid to the data calibration using a full polarimetric calibration procedure derived from measurements at a fixed point [WK91]. SAR images have been obtained using a dedicated SAR processor developed taking into account an existing digital elevation model (DEM) of the structure and the precise knowledge of the system position.

From all the data takes collected over the whole period of measurements, the results of the first data take will be presented in the following. For the chosen data take, the circular synthetic aperture was used.
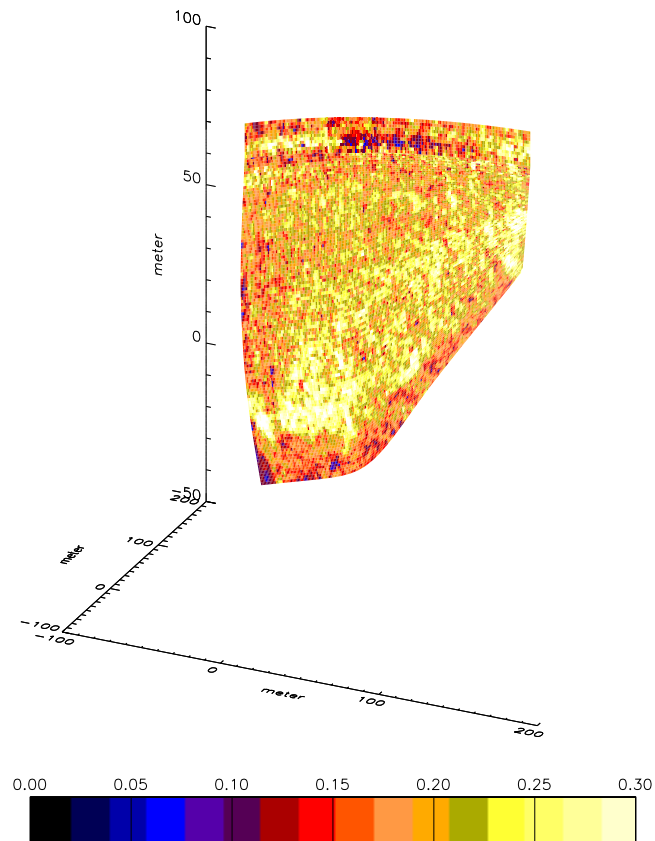
Figure 5.10: Image of the polarimetric gain for the Ridracoli experiment

Parameter	Value
Start frequency	5.2 GHz
Stop frequency	6.0 GHz
Frequency step size	500 kHz
Number of frequency points	1601
Transmit polarisation	Horizontal and vertical linear
Receive polarisation	Horizontal and vertical linear
Transmit power	30 dBm
Circular aperture angle	88°
Angular step size	0.5°
Number of angular points	177
Linear aperture length	4000 mm
Linear step size	20 mm
Number of linear points	201
Calibration distance	1118 mm
Calibration procedure	Disc, empty room, dihedral 0° and 45°
Target distance	80 m - 250 m
Resolution in range	37.5 mm
Resolution in elevation	720 mm - 2250 mm
Resolution in azimuth	500 mm - 1560 mm

Table 5.2: Summary of the measurement parameters for the interferometric SAR experiment

Polarimetric Information Content of the Data

The analysis of the polarimetric properties of this data take shows that the polarimetric information content in the data is relatively low. The additional information that is obtained by using radar polarimetry is in the order of 10 % to 20 %. It hardly exceeds 25 %. The statistics of the polarimetric gain are shown in the histogram of figure 5.11.

The uniform type of target promises also a uniform distribution of the polarimetric information over the target. Figure 5.10 shows the image of the polarimetric gain. In order to provide an image that is easier to analyse, the processed data has been focused on the digital elevation model of the dam. It can be noticed that the polarimetric gain depends solely on the incidence
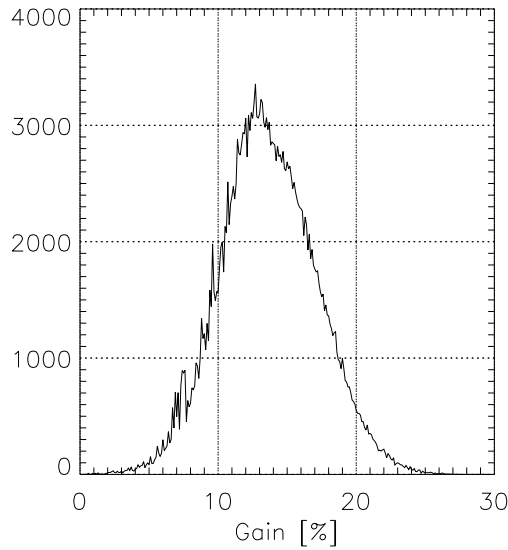
Figure 5.11: Histogram of the polarimetric gain for the Ridracoli experiment

angle with respect to the dam. This behaviour arises from the fact that on an interface of two electric different materials the reflection and transmission of electromagnetic waves is polarisation-dependent [Fun94, Sim89]. The only irregularities in the image can be noticed at the crown of the structure where on the left hand side of the dam the holes for the water overflow and on the right hand side of the dam huge trihedral-like concrete structures are formed. The polarimetric gain at these trihedral-structures can be observed to be even lower than in the remaining structure. This is in very good concordance with the theoretical behaviour that has been analysed in the preceding chapter, where it has been shown that the polarimetric gain of trihedral corner-reflectors is zero.

The data analysis was also applied to other data takes of this experiment and the results were comparable.

5.3   High Resolution 3D-Data

The use of radar remote sensing for retrieving forest parameters was discovered already in the early days of radar remote sensing [GR82]. The importance of polarisation was soon discovered [Sie85, RW86]. Despite all advances

in experimental measurements on vegetation [KF89, HMK89, Hir87], it was only recently that a fir tree was analysed in a three-dimensional high resolution measurement [FS99, FPL98, LS98]. The following polarimetric analysis is based upon this data. The data was collected in the *European Microwave Signature Laboratory* [Sie93, Nes94], the laboratory equivalent for the *LISA* outdoor radar. The importance of polarimetric high resolution data for a better understanding is also underlined in [BB99].

Experiment Set-up

The experiment was run with two synthetic apertures, allowing the creation of a three-dimensional radar image [For98]. The parameters for experiment are given in table 5.3. The tree was a 5 meters high Balsam fir tree (*Abies Nordmanniana*), being approximately 21 years old.

From the processed three-dimensional SAR data [FS99], a central cut in azimuth has been extracted in order to limit the amount of data. This cut represents a slice of the total data with an extension of 6 meters in elevation, 5 meters in range and of 150 millimeters, hence a single resolution cell in azimuth. Such a slice of the data is not equivalent to a two-dimensional SAR, as it is not a projection of all azimuth information onto a plane. This sub data comprises information on the trunk, the needles and on branches. Beyond that, it is also the data slice with the best ratio of target to surrounding air. A radar-image of the vv-polarisation of this slice and a photo of the tree, are given in figure 5.12.

SAR Amplitude Image

In this image 5.12 can be noticed the shape of the tree that is very similar to the optical impression in the photo, despite the fact that the ratio target to wavelength differs by many magnitudes. It is also interesting to see that, despite the use of frequencies upto 5.5 GHz the radar scattering does not only take place on the outer branches but that there are many strong scatterers inside the tree.

As the data has been taken using very wide aperture angles, both in azimuth and elevation, it is very unlikely that other than direct scattering will focus in the SAR-image. This arises from the fact, that double or multiple-

Parameter	Value
Start frequency	1.0 GHz
Stop frequency	5.5 GHz
Frequency step size	5.625 MHz
Number of frequency points	401
Transmit polarisation	Horizontal and vertical linear
Receive polarisation	Horizontal and vertical linear
Transmit power	30 dBm
Averaging factor	128
ISAR in azimuth	
Azimuth start angle	-12º
Azimuth stop angle	12º
Azimuth angular step	0.6º
Number of azimuth steps	41
SAR in elevation	
Elevation start angle	28º
Elevation stop angle	52º
Elevation angular step	0.3º
Number of elevation steps	81
Calibration distance	9560 mm
Calibration procedure	Disc, empty room, dihedral 0º and 45º
Center of target distance	9560 mm
Resolution in range	60 mm
Resolution in elevation	60 mm
Resolution in azimuth	150 mm

Table 5.3: Summary of the measurement parameters for the 3D SAR imaging of a fir tree
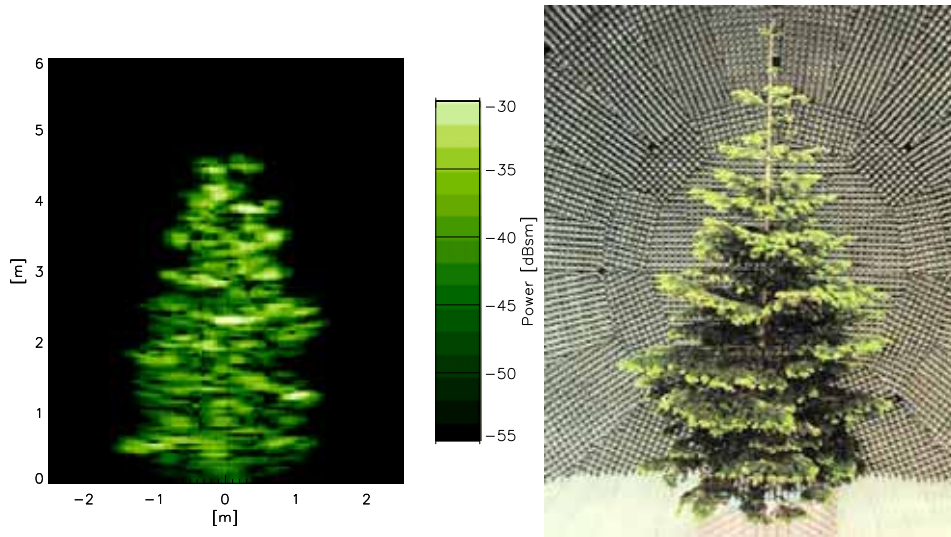
Figure 5.12: Radar-image of a central cut through the fir tree (vv-data). Photograph of the fir tree inside the anechoic chamber of the *EMSL*, front view

bounce scattering will not take place at exactly the same places while looking from varying angles on the target. Consequently the energy of the multiple-bouncing part of the received signal will be blurred all over the SAR image and only increase the noise level in the image.

The main contribution to this internal scattering is still given by needles and small branches. This conclusion is based on the fact that no trunk-like structure can be spotted in the image. This effect is surprising, as the trunk is electrically much larger than the needles.

Polarimetric Information Content

From this data slice, the polarimetric information content has been analysed. A histogram of the polarimetric gain for the data is given in figure 5.14. To the calculation of the gain has been added a threshold. This threshold will exclude all data with a power level below -90 dBsm. Thus, the data volume that is not filled with parts of the tree will not contribute to the histogram. As already noted in the other experiments, the average gain that is achieved
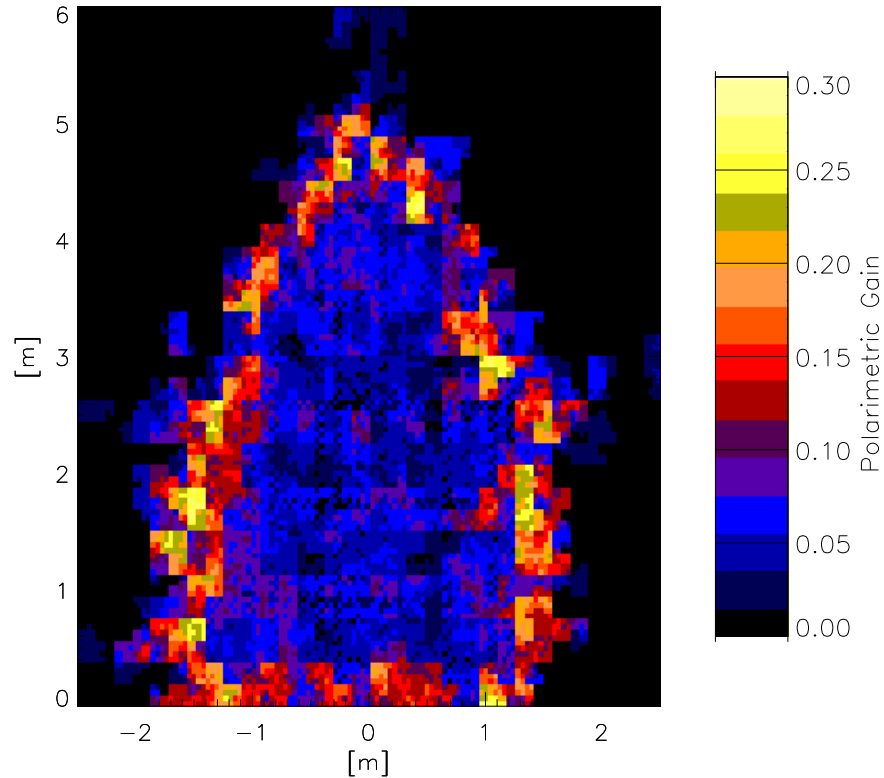
Figure 5.13: Image of the polarimetric gain for the balsam fir tree

by making use of the polarimetric information, instead of using only the hh-polarised channel, is in the order of 5 %. Despite this fairly low gain, there is also a significant part of a polarimetric gain of around 20 %. In order to evaluate the contribution of the different parts of the tree and to clarify whether the high information content is caused by a recognizable element of the tree, an image of the gain is given in figure 5.13.

In this image, the area of high polarimetric information can be spotted easily. The circumference of the tree has a significantly higher gain than has the rest of the tree. This fact allows the assumption that it is especially the
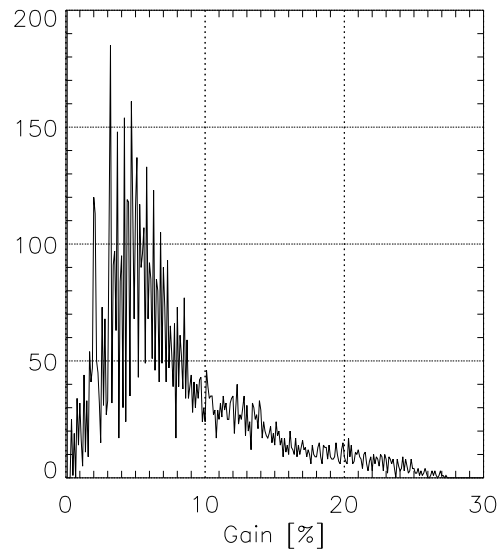
Figure 5.14: Histogram of the polarimetric gain for the balsam fir tree

needles that contribute to the polarimetric information. The polarimetric gain is in the same order not only on the lateral sides of the tree, but also on the bottom side of the circumference. This bottom side was not illuminated directly by the radar wave. Thus, the observed behaviour apparently is not due to the fact that the circumference gives the first scattering to the wave and for all further scattering the wave is already attenuated and loses many of its polarimetric properties.

The appearance of the polarimetric information on the circumference of the tree might be an indication, how polarimetric interferometry is able to distinguish between two different scattering centers on forests [CP98] and to measure the medium height of the trees from a satellite. A whole forest will show an integrated circumference of all its trees, such that only the upper layer of the crowns and the bottom layer of the trees together with the ground interaction contain considerable polarimetric information.

Results of the Experiment

Recapitulating the effects that have been observed by use of the polarimetric gain, the following conclusions can be drawn:

- the information that is obtained by using a full-polarimetric radar in-

stead of a single polarisation radar for high resolution measurements
on a balsam fir tree ranges from 5 % to 25 %,

- the highest polarimetric information content in the data could be iden-
tified with structures around the circumference of the tree, these struc-
tures could be the first layer of needles and the outer branches,

- even non-illuminated sides of circumference of the tree have a relatively
high polarimetric gain,

- this behaviour could prove that the scattering centers that can be sep-
arated with polarimetric interferometry correspond to the treetop and
to the height of the lowest branches.

5.4   Spaceborne Data

Up to now all radar remote sensing satellites make only use of a single polar-
isation. In 1994 two missions with the *SIR-C* ("Shuttle Imaging Radar C")
were flown [Eva93]. During these missions, the first full polarimetric radar
images of the earth were taken. The polarimetric data was taken in two dif-
ferent frequency bands, at L-band, corresponding to a frequency of 1.254 GHz
and at C-band or 5.304 GHz, respectively. Furthermore a third radar sensor
operating at X-band (9.68 GHz) was used in the shuttle. These X-band data
are not analysed in the following as they are only single polarisation data.
The typical resolution cells of the *SIR-C* data is 12 by 12 meters on the earths
surface. The measurement parameters for the *SIR-C* are listed in table 5.4

As first example of spaceborne polarimetric SAR-data has been chosen
data from the second flight of *SIR-C*. The data has been taken at 6:42 am on
October 1st 1994. The area of the data is around Ispra, a village on the east
shore of Lago Maggiore in Northern Italy. The geographic location of the
area has the latitude of 45º 49′ north and the longitude of 8º 37′ east. The
data take is named "Ötztal, Austrian Alps" and its data-ID is 014.20. On
the chosen data window are two lakes, the "Lago Maggiore" and the smaller
"Lago di Monate", a couple of smaller villages, cereal fields, mixed forests and
a former nuclear research center (now Joint Research Centre of the European
Commission, ex EURATOM) with two decommisioned reactors.

Parameter	Value
L-band frequency	1.254 GHz
L-band polarisation	hh, hv, vh, vv
Pulse repetition frequency	1736 Hz
C-band frequency	5.304 GHz
C-band polarisation	hh, hv, vh, vv
Pulse repetition frequency	1736 Hz
X-band frequency	9.68 GHz
X-band polarisation	vv
Pulse repetition frequency	1786 Hz
Site name	Ötztal, Austrian Alps
Site ID	014.20
Data segment	06
Date	October 1st 1994
Time	06:42:39
Latitude at image center	45.72º N
Longitude at image center	8.62º E
Swath width	30,290 m
Incidence angle	35.96º
Resolution	12.5 m × 12.5 m
Geodetic altitude	229,890 m
Orbital direction	Ascending

Table 5.4: Summary of the *SIR-C* instrument parameters and the parameters of the processed scene
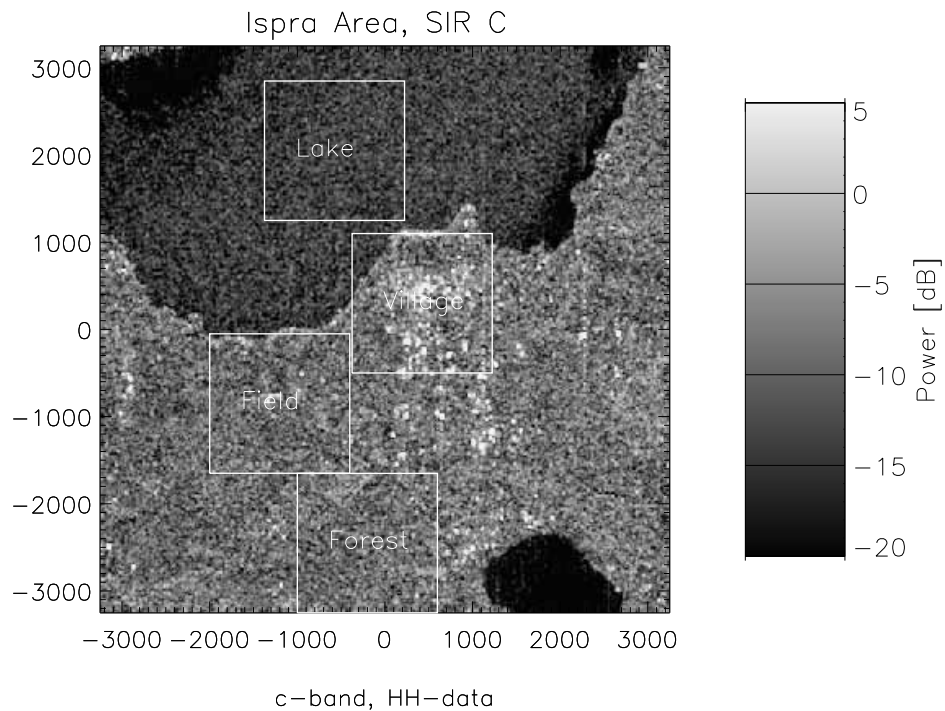
Figure 5.15: *SIR-C* image of the Ispra area, northern Italy (C-band, hh-data)

Polarimetric Decomposition

By the use of coherent decomposition techniques for polarimetric radar images, different scattering mechanisms can be separated [CP96]. Applying the Cloude decomposition on the given data, the following results are obtained for L-band-data 5.16 and C-band-data 5.17, respectively. The results of the decomposition are given in a false colour plot, assigning red to sphere-like scattering, green to vertical dihedral-like scattering and blue to depolarising (45° tilted) dihedral-like scattering.

In both bands, no area of a dominant scattering mechanism can be detected. This might be already an indicator for little use of the polarimetric information in this data take.
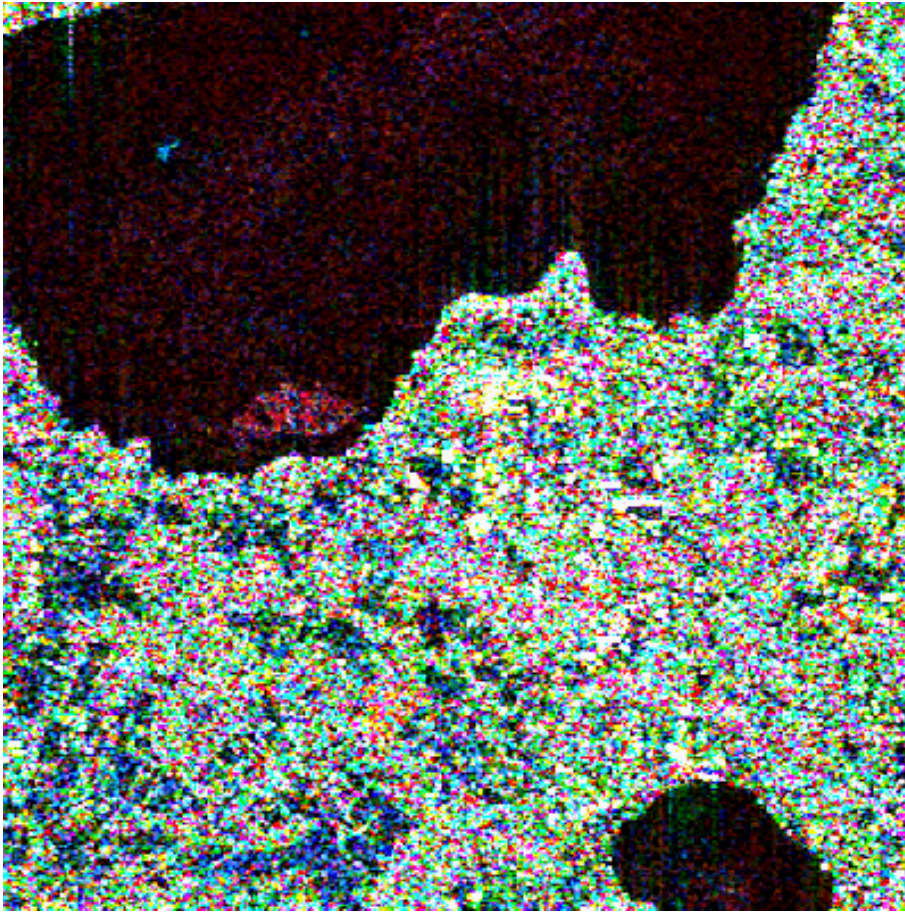
Figure 5.16: Cloude decomposition for L-band *SIR-C* data
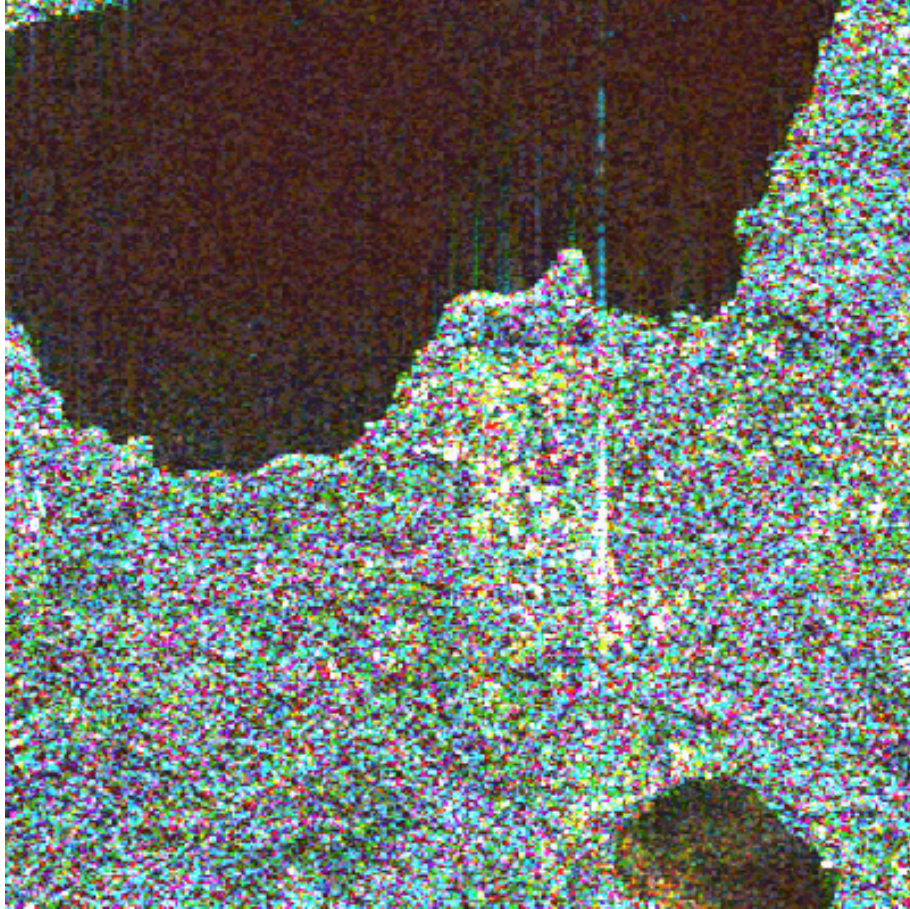
Figure 5.17: Cloude decomposition for C-band *SIR-C* data

Polarimetric Gain

In order to be able to evaluate the importance of the polarisation of the referring channel, all possible entropies as in figure 3.4 are calculated. These properties have been calculated for the whole scene and then for special areas of interest. These areas of interest have been selected in order to cover only a single type target. The size of the radar image was 128 by 128 pixels for the single landscape targets (e.g. lake, fields) and 512 by 512 pixels for the overall, mixed, scene. An image of the scattered power with the respective areas of interest is shown in figure 5.15.

From the above shown data it can be seen that the results for the polarimetric gain strongly depend on the basis polarisation that is chosen. This

Land use	Frequency	$H(hh)$	$H(hv)$	$H(vv)$	$H(hh, hv, vv)$
Lake	L-Band	6.885	6.863	7.285	13.984
Lake	C-Band	6.952	6.838	7.323	13.983
Fields	L-Band	6.067	6.688	6.972	13.968
Fields	C-Band	5.694	5.222	5.908	13.774
Forest	L-Band	6.175	6.186	6.916	13.938
Forest	C-Band	6.649	6.809	6.998	13.975
Village	L-Band	5.052	5.578	5.110	12.910
Village	C-Band	5.104	5.035	5.824	13.011
Mixed	L-Band	3.078	3.752	4.580	10.895
Mixed	C-Band	2.788	3.095	4.518	9.948

Table 5.5: Entropy values for the sample data

Land use	Frequency	$H(hh, hv)$	$H(hh, vv)$	$H(hv, vv)$
Lake	L-Band	12.441	13.059	12.992
Lake	C-Band	12.517	13.126	12.944
Fields	L-Band	12.112	12.354	12.730
Fields	C-Band	10.560	11.248	10.756
Forest	L-Band	11.827	12.392	12.386
Forest	C-Band	12.580	12.772	12.815
Village	L-Band	10.069	9.749	10.224
Village	C-Band	9.632	10.432	10.355
Mixed	L-Band	6.543	7.439	8.012
Mixed	C-Band	5.603	7.064	7.289

Table 5.6: Entropy values for the sample data (cont.)

result may delude, but it is important, as in this way a rule for the choice of a single polarisation system is given. For the above example, a single polarisation system would favorably work in vv-polarisation, as the gain with respect to vv-polarisation is the lowest.

As the polarimetric gain does not contain any information about the spatial distribution of the information, the local polarimetric gain for the data has been calculated. By this, not only the decomposition results, but also the polarimetric classification will be based on a more solid theoretic basis. Already from the classification, the polarimetric gain may be expected to be very low. In order to identify areas of high polarimetric potential, the local gain of the data has been calculated. Figures 5.18 and 5.19 show the

Land use	Frequency	g_{hh}	g_{hv}	g_{vv}
Lake	L-Band	1.04	1.04	0.92
Lake	C-Band	1.01	1.04	0.91
Fields	L-Band	1.30	1.09	1.00
Fields	C-Band	1.42	1.64	1.33
Forest	L-Band	1.26	1.25	1.02
Forest	C-Band	1.10	1.05	1.00
Village	L-Band	1.56	1.31	1.53
Village	C-Band	1.55	1.58	1.23
Mixed	L-Band	2.54	1.90	1.38
Mixed	C-Band	2.57	2.21	1.20

Table 5.7: Polarimetric gain for the sample data

plots of the local gain of the polarimetric data with respect to the hh-channel.

As expected, this gain is very low. The corresponding histograms in figure 5.20 show that in both frequency bands it hardly exceeds a value of 20 %. This explains the failures in polarimetric signal processing both for classification and for decomposition.

Results of the Data Analysis

In this experiment, the concept of the polarimetric gain as basis for a further analysis of the data are applied to polarimetric spaceborne data. In contrast to the preceding experiments as described in sections 5.1, 5.2 and 5.3 the resolution of the data is much coarser. This implies that each resolution cell being approximately 12.5 by 12.5 meters in size, represents the coherent integration of many scatterers. In this context, radar polarimetry's role is more important than it is with high resolution data, as high resolution allows the identification of targets already by means of the amplitude whereas in low resolution data polarimetric information can play an important role for the identification of targets.

The given *SIR-C* data are analysed with traditional tools of radar polarimetry such as coherent decomposition techniques [CP96]. For both L- and C-band-data, the obtained results give no particular polarimetric property of the data. The use of the concept of the polarimetric gain proves this result. Beyond the calculation of the overall polarimetric gain for the whole scene and for sub-scenes with comparable targets, the local polarimetric gain
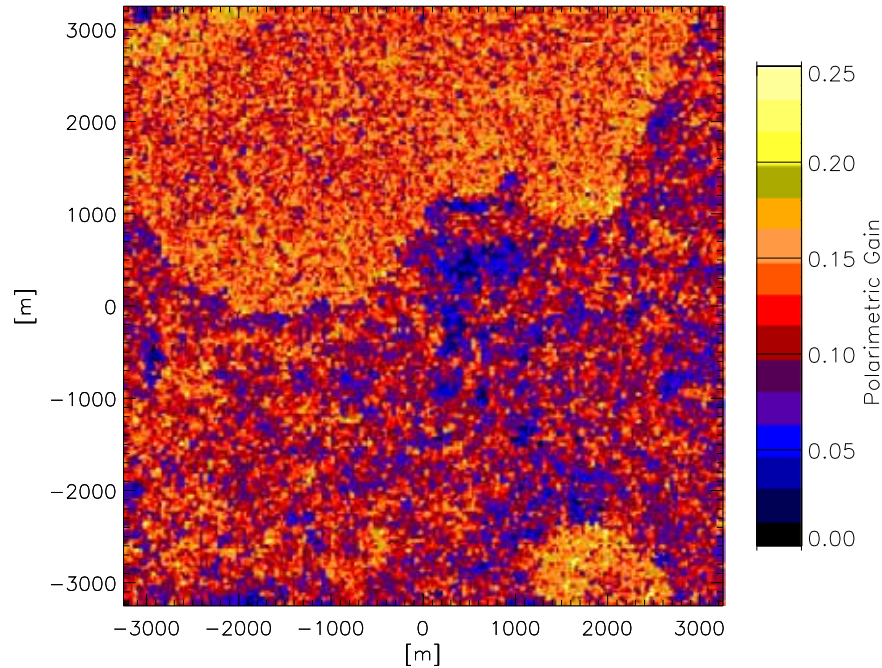
Figure 5.18: Polarimetric gain for L-band data

is displayed as an image.

The analysis of the polarimetric gain shows slight differences in the obtained gain, depending on the target type. Interestingly, the polarimetric gain hardly depends on the reference polarisation. A major drawback of this approach is the fact that the number of pixels used for the calculation of the entropies influences strongly the result and generally the gain is enhanced with a higher number of pixels. This disappointing result is due to the fact that the chosen sub-scenes are not homogeneous enough to give a similar polarimetric response. Therefore the local gain proves to be a much more powerful tool for the analysis of the data. In particular, the analysis of the polarimetric gain shows that the data is of little polarimetric information content, and most of this polarimetric information is concentrated on the
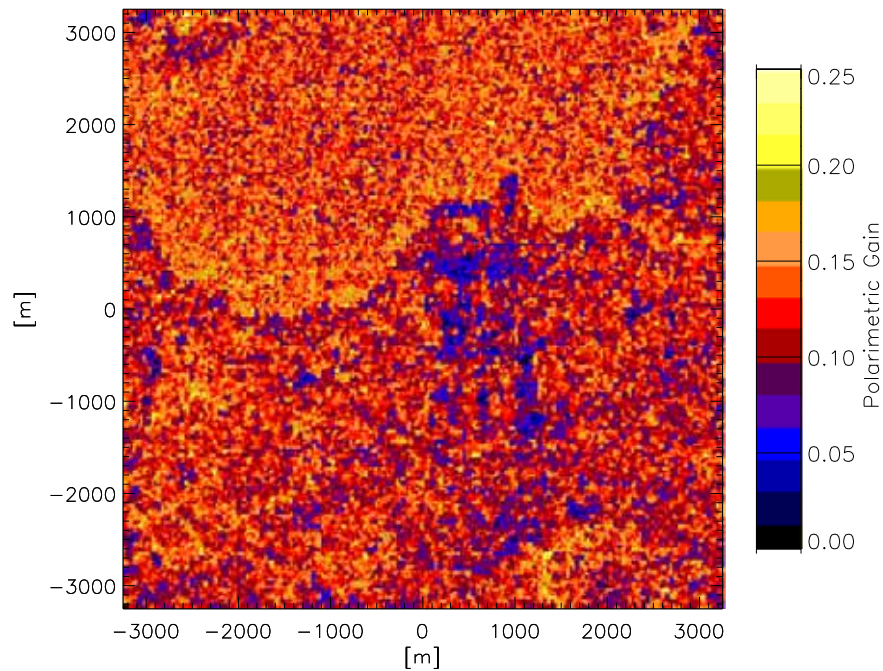
Figure 5.19: Polarimetric gain for C-band data

water surface of a lake where no other targets than water are present. This behaviour confirms the use of radar polarimetry for the detection of marine objects such as ships [BWS93, RBSK70]. Due to the higher homogeneity of the lake's surface its properties change less with a varying number of pixels involved in the averaging process.

Finally the dependence of the calculation of ensemble averages upon the used path to scan the data is shown. The advantages of using a coherence maximising scan-path [NP92] over a traditional scan are shown. This result is not only important for the determination of the entropies for the calculation of the polarimetric gain, but also all other techniques based on statistical methods, such as the H-α-classifier [CP97], could benefit from this result.
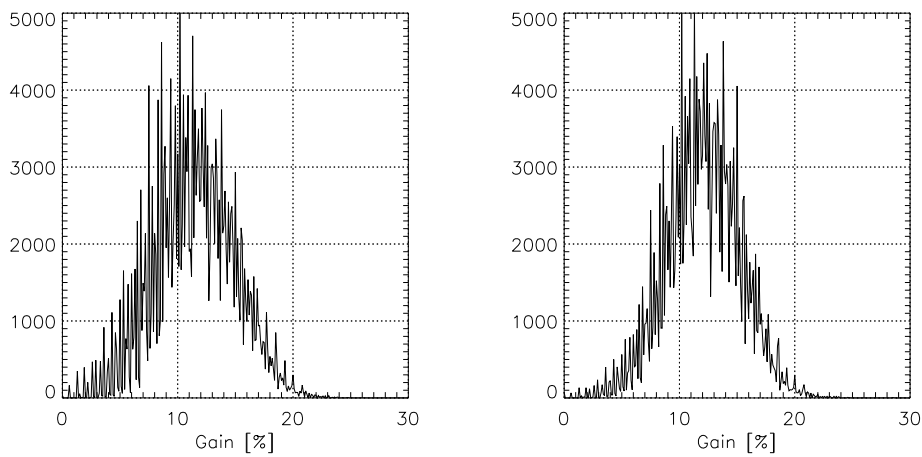
Figure 5.20: Histogram of the local gain for L- and C-band data, respectively
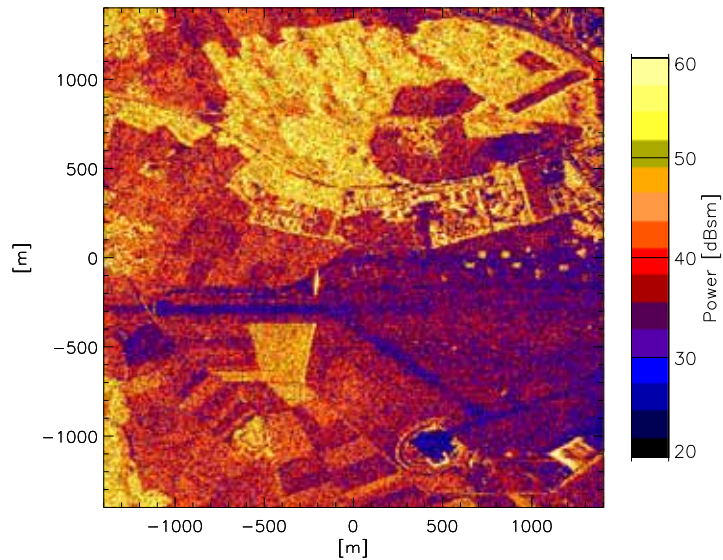
Figure 5.21: *E-SAR* image of the Oberpfaffenhofen airfield, Germany

5.5   High Resolution Airborne Radar

A result of the preceding paragraphs is that the use of polarisation in radar systems increases with the increase of resolution. This is due to the fact that
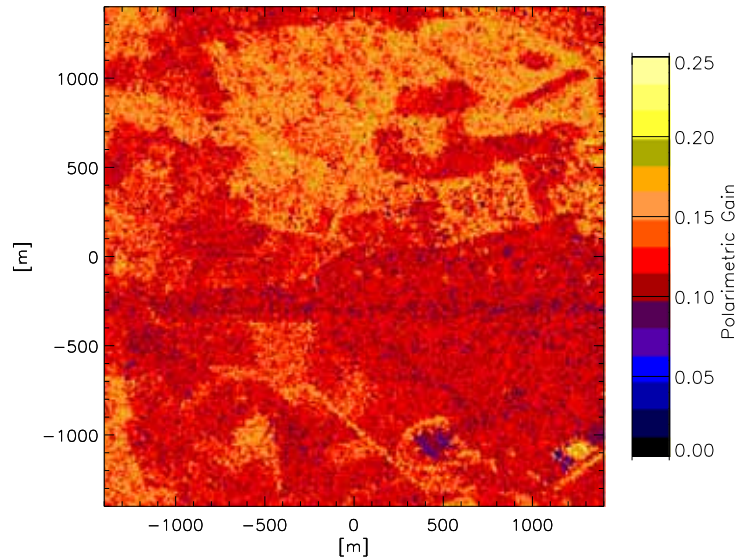
Figure 5.22: Image of the polarimetric gain for the Oberpfaffenhofen data

in high resolution radar systems the polarising effects of single scatterers are not leveled by other objects in the resolution cell.

The *E-SAR* system from the Deutsche Forschungsanstalt für Luft- und Raumfahrt e. V. (DLR) is a multi-frequency synthetic aperture radar mounted on board of Dornier Do-228 aircraft. The radar is working at present in P-, L-, C- and X-band. Further information on the system and applications can be found in [Hor96, Pap98].

The data used in the following is L-band data. The scene of the radar image is the airfield in Oberpfaffenhofen, Germany. The characteristics of the sensor and the data take are summarised in table 5.5.

Figure 5.21 shows the processed SAR image. This image shows the amplitude of the hh-channel. The airfield in Oberpfaffenhofen can clearly be detected, as well as several taxi-ways. On the right-hand side of the image are several buildings of the airfield and the DLR, whereas on the left-hand side the area is untilled and covered with low vegetation, especially grass and

Parameter	Value
L-band frequency	1.3 GHz
L-band polarisation	hh, hv, vh, vv
Pulse repetition frequency	400 Hz
Transmit power	360 W
Receiver noise figure	8.0 dB
Azimuth beamwidth	18°
Elevation beamwidth	35°
System bandwidth	100 MHz
Test site	Oberpfaffenhofen, Germany
Date	Summer 1998

Table 5.8: Summary of the *E-SAR* instrument parameters and the parameters of the processed scene

cereals. On the upper side of the image above the buildings, is a forest. On the lower side of the image can also be detected a heliport of circular shape.

Polarimetric Gain

The determination of the polarimetric gain, reveals in the histogram 5.23a polarimetric gain of maximum 20 %. Two different areas can be observed, one area with a mean gain of around 12 % and relatively many image cells and another area with a higher gain of around 15 % but with fewer pixels.

These two different areas may be divided easily by analysing the image of the polarimetric gain as shown in figure 5.22. A large area of the 12 % gain can be identified as the low growing vegetation with grass and cereals. The polarimetric gain finds its minimum on the ways of the airfield infrastructure, such as the runway, the taxiways and the heliport. Both the wooded zone and the buildings on the airfield show a high polarimetric gain. Parts of the fence around the airfield being invisible in the amplitude image can also be detected in the lower parts of the polarimetric gain image.

Results of the Data Analysis

The application of the polarimetric gain to high resolution radar images reveals several properties of the scene. Objects with a single wave - target interaction (single-bounce) show a low polarimetric gain. In recognition of these
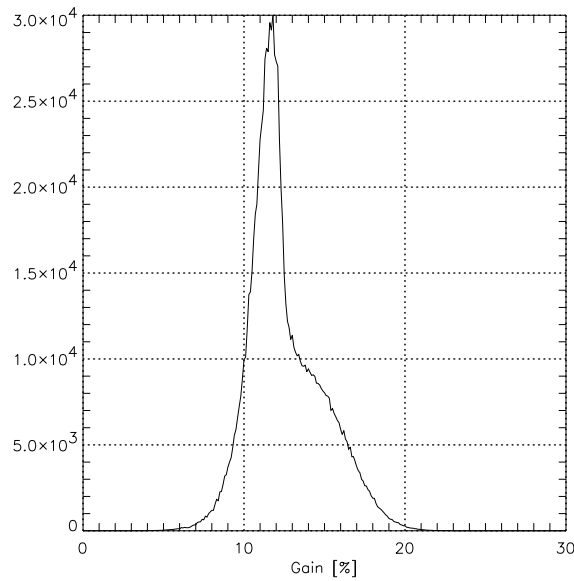
Figure 5.23: Histogram of the polarimetric gain for the Oberpfaffenhofen data

objects, such as the runway, grass fields, etc. radar polarimetry contributes little to a better detection. Objects with distributed scattering centers, such as trees, show a high polarimetric gain. This is in concordance with the results elaborated in paragraph 5.3. A similar high polarimetric gain can be observed in man-made structures. This is basically due to the appearance of 90° angles. This behaviour is not only present at relatively large structures, such as buildings, but also for smaller structures, such as the fence. Again, the theoretical derivation of the polarimetric gain for dihedrals explains this behaviour.

Chapter 6

Conclusion and Outlook

The determination of a quantitative measure for the polarimetric information content of radar data is an important step for an optimised information extraction. The present work contributes to a better understanding of the use of polarimetry for radar and to the establishment of a systematic extraction of the information in polarimetric radar data.

These investigations are embedded into a growing development of sensors and applications of radar polarimetry. This development of polarimetric radar sensors takes place in applications, diverse as remote sensing and mine detection. Applications for polarimetric radar data have been identified for forest growth mapping, biomass estimation, soil moisture measurements and the derivation of snow and ice parameters. The present work links the sensors to the applications.

This link is established by a rigorous application of information theory. This leads to the definition of the polarimetric gain. The polarimetric gain yields a concept, where the advantages of a full polarimetric radar over a single polarisation radar can be expressed in quantitative terms. The definition of the polarimetric gain considers also the statistics of the target area, as it is a relative rather than an absolute measure. As the polarimetric gain suffers, as all statistical methods, by the number of data involved in the statistics and the path that is used for calculating the statistics, a recommendation for the number of pixels is given and an optimised scan path is shown.

The concept has been applied first to canonical targets, such as spheres, dihedrals and random scatterers, where the polarimetric gain could be calculated explicitly and second to real data. These data comprise experiments

on anti-personnel mines, an interferometric demonstration test on a dam for water supply, a high resolution three-dimensional radar image of a fir tree, satellite data from the *SIR-C* experiment in L- and C-band and finally high resolution airborne data from the *E-SAR* system.

The evaluation of the results of these experiments led to two major conclusions. First, the differentiation of different targets is possible by just evaluating the polarimetric gain. Areas of high polarimetric gain correspond generally to targets, where the traditional tools for interpretation of polarimetric information have shown potential for radar polarimetry. These areas comprised targets like water surfaces, ground clutter removal or the outer layer of needles of a fir tree. This fact implies that the evaluation of the polarimetric gain is a useful method for a systematic approach to an optimised extraction of the spatial information in full polarimetric data. Second, on average the gain of a full polarimetric radar is in the order of 10 % to 30 %. On one hand, this value has to be compared to the additional hardware that is used for a full polarimetric radar which approximately doubles. On the other hand, the result gives no hint about the quality of this extra 10 % of information. Eventually, these data contain the only information of interest to the user.

The application of the Hilbert-scan to the data yields not only advantages in the evaluation of the information content, but also well established signal processing, such as the classification based on the polarimetric entropy benefit from this scan, as the coherence in the data is maximised along the scan.

These results underline the possibility of using the concept of the polarimetric gain for a first and fast scan of the data. With this scan it is already possible to identify regions where radar polarimetry contributes to an increased information. This enables a more economic use of the subsequent steps of information extraction. The polarimetric gain might play an important role in integrating the polarimetric radar data into a sophisticated system of data mining.

The presented concept could be used as a basis for a systematic integration of data from resources other than (polarimetric) radar. In fact, the presented approach seams to be easily extendable to a general approach for identifying the information in data fusion concepts. Another aspect of this

work, whose investigation promises useful results for the signal processing of radar data, is the use of the Hilbert-scan for other purposes. These purposes could cover problems from phase unwrapping for interferometric data, where the Hilbert-scan could reduce the two-dimensional problem to a one-dimensional problem, to compression of the data, where again the characteristic of the Hilbert-scan to maximise the coherence is exploited. It is also data compression, where the obtained number of maximum distinguishable classes may play a role, as it is also an indicator of the maximum obtainable compression that the data may undergo.

Finally, the observed properties of the distribution of the polarimetric gain over the fir tree could help to validate and to develop models for the scattering behaviour of conifers. Furthermore it might be a source of explanation for the detection of tree heights and the occurring errors in polarimetric interferometry.

Appendix A

List of Symbols

A	Arm length
α	Anisotropy
c	Velocity of light
C	Capacity
D	Real antenna aperture
δ	Cross-range resolution
E	Expectation value
$\vec{E}$	Electric field vector
f_p	Pulse repetition frequency (PRF)
Δf	Bandwidth
g_{hh}	Polarimetric gain referred to the hh-channel
g_i	Element of the Stokes-vector
G	Antenna-gain
h	Cartesian coordinate, horizontal
$\vec{h}$	Unity vector in h-direction
hh	Horizontal transmitted and horizontal received
hv	Vertical transmitted and horizontal received
H	Entropy as defined by S. Cloude and E. Pottier in [CP97]
$\mathcal{H}$	Elements of the Hilbert-curve
$H(X)$	Entropy of the random variable X
i^{hh}	Additional information with respect to the hh-channel
I	Information
j	imaginary unit
κ	Wavenumber

L	Synthetic aperture length
λ	Wavelength
λ_i	Eigenvalue
n	Number of steps
N	Noise power
$p_X(x)$	Probability density function
P	Power
φ	Phase
r	Spherical coordinate (radius)
R	Distance
ΔR	Range resolution
ρ	Depolarisation ratio
S	Signal power
$\mathbf{S}$	Scattering matrix
$\underline{\sigma}$	Radar cross section
σ^0	Differential radar cross section
σ	Standard deviation
t	Time
$\mathbf{T}$	Coherence matrix
θ	Spherical coordinate (angle)
Θ	Antenna beamwidth
τ	Spherical coordinate (angle)
τ	Pulse-length
v	Cartesian coordinate, vertical
$\vec{v}$	Unity vector in v-direction
vh	Horizontal transmitted and vertical received
vv	Vertical transmitted and vertical received
x	Cartesian coordinate for image coordinates
X	Random variable (input)
$\mathcal{X}$	Alphabet for elements of X
y	Cartesian coordinate for image coordinates
Y	Random variable (output)
$\mathcal{Y}$	Alphabet for elements of Y
z	Cartesian coordinate, $z = h \times v$

Appendix B

Useful Formulas

In this appendix a short list of useful formulas, other than those already emerged earlier in this work, in radar polarimetry is presented.

Sometimes the antennas used in polarimetric radar systems use a circular rather than a linear basis. These equations describe the Stokes-space in righthand- and lefthand circular coordinates

$$
\begin{pmatrix} g_0 \\ g_1 \\ g_2 \\ g_3 \end{pmatrix} = \begin{pmatrix} E_r E_r^* + E_l E_l^* \\ E_l E_r^* + E_r E_l^* \\ j\left(E_r E_l^* - E_l E_r^*\right) \\ E_r E_r^* - E_l E_l^* \end{pmatrix} = \begin{pmatrix} r \\ h \\ v \\ z \end{pmatrix}
\tag{B.1}
$$

For converting the vector basis form linear to circular, or vice versa,

$$
\begin{pmatrix} E_l \\ E_r \end{pmatrix} = \begin{pmatrix} \frac{1}{\sqrt{2}} & \frac{j}{\sqrt{2}} \\ \frac{1}{\sqrt{2}} & \frac{-j}{\sqrt{2}} \end{pmatrix} \begin{pmatrix} E_h \\ E_v \end{pmatrix}
\tag{B.2}
$$

$$
\begin{pmatrix} E_h \\ E_v \end{pmatrix} = \begin{pmatrix} \frac{1}{\sqrt{2}} & \frac{1}{\sqrt{2}} \\ \frac{j}{\sqrt{2}} & \frac{-j}{\sqrt{2}} \end{pmatrix} \begin{pmatrix} E_l \\ E_r \end{pmatrix}
\tag{B.3}
$$

The explicit expression for the coherence matrix results as:

$$
< \mathbf{T} >= \vec{S} \cdot \vec{S^*}^T =
\tag{B.4}
$$

$$
< \begin{pmatrix} (S_{hh} + S_{vv})(S_{hh} + S_{vv})^* & (S_{hh} + S_{vv})(S_{hh} - S_{vv})^* & 2(S_{hh} + S_{vv})S_{hv}^* \\ (S_{hh} - S_{vv})(S_{hh} + S_{vv})^* & (S_{hh} - S_{vv})(S_{hh} - S_{vv})^* & 2(S_{hh} - S_{vv})S_{hv}^* \\ 2S_{hv}(S_{hh} + S_{vv})^* & 2S_{hv}(S_{hh} - S_{vv})^* & 4S_{hv}S_{hv}^* \end{pmatrix} >
$$

Appendix C

Polarimetric on Receive Radar

To follow the request for cheap and lightweight sensors, especially for satellite use, many of the future remote sensing satellites are only on the receiver side polarimetric 1.2. These radars are transmitting as conventional radars only a single polarisation (e.g. horizontal polarisation), whereas the receiver is capable of receiving the transmit and its orthogonal polarisation. Such a design requires significantly less weight and power, but still is capable of receiving two out of three independent elements of the scattering matrix.

In this appendix is shown a method that describes the maximum number of distinguishable received signals with polarimetry for a polarimetric on receive radar. This number is equivalent to the maximum obtainable gain for such a radar.

The received signal of a polarimetric on receive radar is well suited for representation on the Poincaré-sphere [Wan88, Ger99]. Any single received polarisation will appear as a point on the surface of the Poincaré-sphere. If the received polarisation suffers disturbances, the single point will spread out and a cloud of points can be observed on the Poincaré-sphere. This effect limits the maximum number of distinguishable polarisations, as only a limited number of points will fit on the Poincaré-sphere.

An ergodic process will be assumed, such that the mean observed polarisation will converge to the transmit polarisation citepapoulis. Due to this spread, the number of distinguishable points on the Poincaré-sphere that can be observed in a finite time is limited.

In order to evaluate the maximum number of distinguishable polarisations, it has to be shown how many of these scattering clusters can be placed

101

on the sphere. This depends of course on the amount of depolarisation. It is assumed that the noise is distributed equally on the sphere. In order to prove that the Poincaré-sphere is "white", changes in all of the spherical coordinates have to be considered.

A rotation of the antenna system in the h-v-plane and with an angle of β [Wie92, Mly91], in other words a rotation of the Poincaré-sphere

$$
\begin{aligned}
\begin{pmatrix} E_h^{'} \\ E_v^{'} \end{pmatrix} &= \mathbf{R}(\beta) \begin{pmatrix} E_h \\ E_v \end{pmatrix} \\
&= \begin{pmatrix} \cos\beta & \sin\beta \\ -\sin\beta & \cos\beta \end{pmatrix} \begin{pmatrix} E_h \\ E_v \end{pmatrix}
\end{aligned}
\tag{C.1}
$$

results in coordinates $r^{'}, 2\tau^{'}$ and $2\theta^{'}$ as[1]

$$
\begin{aligned}
r^{'} &= r \tag{C.2} \\
2\theta^{'} &= 2\theta + 2\beta \tag{C.3} \\
2\tau^{'} &= 2\tau \tag{C.4}
\end{aligned}
$$

For changes in the other direction, it is practical to rotate first the coordinate system around the h-axis. This leads to spherical coordinates $r, 2\xi, 2\chi$

$$
\begin{aligned}
2\xi &= \tan^{-1} \frac{z}{h} \tag{C.5} \\
2\chi &= \sin^{-1} \frac{v}{r} \tag{C.6}
\end{aligned}
$$

Concentrating on circular rather than linear polarised antennas simplifies this proof, Similar to the above described proof, also these antennas will be rotated,

$$
\begin{pmatrix} E_r^{'} \\ E_l^{'} \end{pmatrix} = \mathbf{R}(\beta) \begin{pmatrix} E_r \\ E_l \end{pmatrix}
\tag{C.7}
$$

and a new coordinate system $r^{'}, 2\xi^{'}, 2\chi^{'}$ with

$$
\begin{aligned}
r^{'} &= r \tag{C.8} \\
2\chi^{'} &= 2\chi \tag{C.9} \\
2\xi^{'} &= 2\xi - 2\beta \tag{C.10}
\end{aligned}
$$

---

[1]This is easily proven by calculation of the polarisation ratio $\rho^{'}$ and the relation $\tan^{-1} x + \tan^{-1} y = \tan^{-1} \frac{1-xy}{x+y}$

These two results show, that any motion on the Poincaré-sphere does not affect the distances to other polarisations. Hence it has been shown that the polarisations are distributed equally on the sphere. This enables to concentrate the concentration on one transmit polarisation. This transmit polarisation is chosen as H polarisation, as the mathematics involved will simplify significantly. Another simplification consists in introducing a coordinate system $2\alpha, \varphi, r$ that measures directly the distances of any point on the sphere, starting at h-polarisation [Clo97].

$$2\alpha \quad = \quad \cos^{-1} \frac{E_h^2 - E_v^2}{E_h^2 + E_v^2} \tag{C.11}$$

$$\varphi \quad = \quad \varphi_x - \varphi_y \tag{C.12}$$

and r as defined before, a measure for distances on the Poincaré-sphere (2α) is obtained.

The coordinates of the point of h-polarisation result as $2\alpha = 0$ and any φ. The distance of any polarisation to h-polarisation is 2α, with a

$$2\alpha = \cos^{-1} \frac{1 - |\rho|^2}{1 + |\rho|^2} \tag{C.13}$$

it is obvious, that the factor $|\rho|$ describes the purity of the signal. Assuming a gaussian distribution for $|\rho|$ with a σ being the sum of both noise and depolarisation power $\sigma = N + D$

$$f_{|\rho|}\left(|\rho|\right) = \frac{1}{\sigma\sqrt{2\pi}} \exp^{-\frac{\rho^2}{2\sigma^2}} \tag{C.14}$$

the distribution for 2α can be expressed [CT90] as

$$f_{2\alpha}\left(2\alpha\right) \quad = \quad \frac{1}{|f'(\rho)|} f_{|\rho|}(|\rho|) \Bigg|_{|\rho|=f^{-1}(2\alpha)}$$

$$= \quad \frac{1 + \tan^2 \alpha}{2\sigma\sqrt{2\pi}} \exp^{-\frac{\tan^2 \alpha}{2\sigma^2}} \tag{C.15}$$

In figure C.1 this distribution for 2α is plotted on the Poincaré-sphere. For this plot a $\sigma = 10$ was chosen, as for a better signal to noise ratio the distribution atop of the sphere is hardly visible. Integrating over this distribution, a pseudo numerical solution

$$\int_0^\xi f_{2\alpha}\left(2\alpha\right) \sigma\left(2\alpha\right) = Erf\left(\frac{\tan\frac{\xi}{2}}{\sqrt{2}\sigma}\right) \tag{C.16}$$
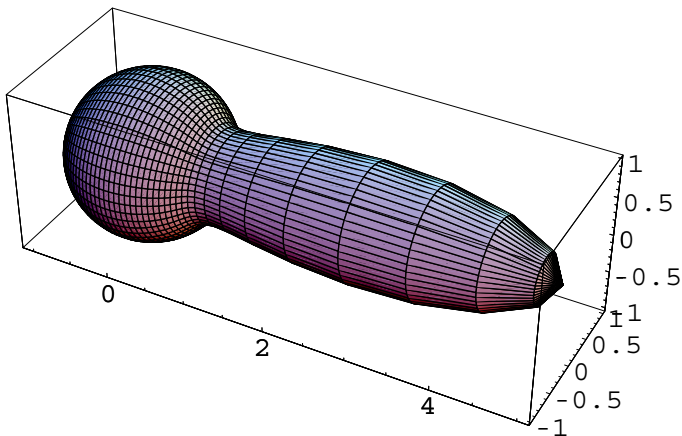
Figure C.1: Distribution of noise (S/N = 10 dB) on the Poincaré-sphere

gives the probability, that a number of points will be inside a given radius around the transmit polarisation. In particular it is possible to express quantile radii for standard probability values.

Quantile	Radius 2α
90%	$2\tan^{-1}\left(1.64485\,\sigma\right)$
95%	$2\tan^{-1}\left(1.95996\,\sigma\right)$
98%	$2\tan^{-1}\left(2.32635\,\sigma\right)$

Table C.1: Probability and quantile radii

For reasonable depolarisation energy, the following approximation may be used $\tan^{-1}\alpha \approx \alpha$ for simplification. Having now calculated these radii,
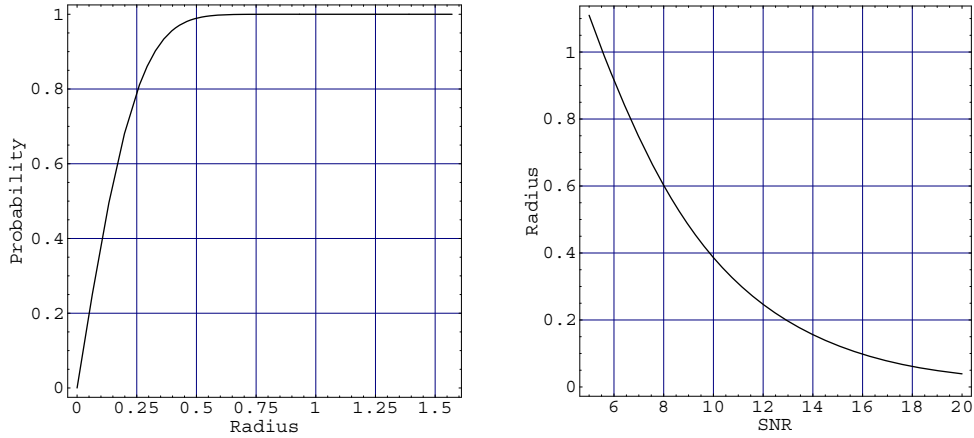
Figure C.2: Probability of detection (S/N = 10 dB) and quantile-radius for a 95 %-quantile

it is straightforward to express, how many of these circles may fit on the Poincaré-sphere. S being the radius of the Poincaré-sphere, the number of circles results as

$$
\begin{aligned}
\Pi &= \frac{4\pi S^2}{2\pi \left(2\alpha\right)^2} \\
&= \frac{1}{2}\left(\frac{S}{p_0\sigma}\right)^2
\end{aligned}
\tag{C.17}
$$

Bibliography

[AH95]   H. Anys and D. He. Evaluation of textural and multipolariza-
             tion radar features for crop classification. *IEEE Transactions
             on Geoscience and Remote Sensing*, 33(5):1170 − 1181, 1995.

[Bal82]   Constantine Balanis. *Antenna Theory: Analysis and Design*.
             John Wiley & Sons, 1982.

[Bal89]   Constantine Balanis. *Advanced Engineering Electromagnetics*.
             John Wiley & Sons, 1989.

[BB99]   Sarah Brown and John Bennett. High-resolution microwave
             polarimetric imaging of small trees. *IEEE Transactions on
             Geoscience and Remote Sensing*, 37(1):48 − 53, January 1999.

[BDPS96]   A. Broquetas, Ramir De Porrata, and Lluis Sagués. A circu-
             lar synthetic aperture radar system for ground-based applica-
             tions. In Giuseppe Nesti, editor, *Proceedings of 1st EMSL User
             Workshop*, EUR Report 17326 EN, pages 57 − 65, 1996.

[Bea94]   A. Beaudoin *et al.* Retrieval of forest biomass from SAR data.
             Int. J. Remote Sensing, 15:2777 − 2796, 1994.

[Boe97]   Wolfgang Boerner*, et al. Manual of Remote Sensing*, chap-
             ter Polarimetry in Radar Remote Sensing: Basic and Applied
             Concepts. America Society for Photogrammetry and Remote
             Sensing, 3 edition, 1997.

[Bro60]   John Brown. On the cross correlation between two noisy chan-
             nels. *IRE Transactions on Information Theory*, page 54, March
             1960.

[BS89]   I. Bronštein and K. Semendjajew. *Taschenbuch der Mathematik.* Harri Deutsch, 24 edition, 1989.

[BWS93]   Wolfgang Boerner, M. Walther, and A. C. Segal. Development of the polarimetric contrast enhancement optimization (OPEC-Filter) procedure and its application to sea surface scatter in pol-sar image analysis. In *Proceedings of IGARSS '93*, pages 33 – 36, August 1993.

[Clo97]   Shane Cloude. Radar polarimetry. Course presented at Joint Research Centre Ispra, October 1997.

[CM91]   J. Curlander and R. McDonough. *Synthetic Aperture Radar - Systems and Signal Processing.* John Wiley & Sons, 1991.

[Col83]   A. J. Cole. A note on space filling curves. *Software - Practice and Experience*, 13:1181 – 1189, 1983.

[Col91]   A. J. Cole. Halftoning without dither or edge enhancement. *The Visual Computer*, pages 232 – 246, 1991.

[Cov72]   Thomas Cover. Broadcast channels. *IEEE Transactions on Information Theory*, IT-18(1):2 – 14, January 1972.

[CP96]   Shane Cloude and Eric Pottier. A review of target decomposition theorems in radar polarimetry. *IEEE Transactions on Geoscience and Remote Sensing*, 34(2):498 – 518, March 1996.

[CP97]   Shane Cloude and Eric Pottier. An entropy based classification scheme for land applications of polarimetric SAR. *IEEE Transactions on Geoscience and Remote Sensing*, 35(1):68 – 78, January 1997.

[CP98]   Shane Cloude and Kostas Papathanassiou. Polarimetric SAR interferometry. *IEEE Transactions on Geoscience and Remote Sensing*, 36(5):1551 – 1565, 1998. Part 1.

[CT90]   Fancesco Carassa and Guido Tartara. *Introduzione ai processi casuali.* clup Milano, 1990.

[CT91]   Thomas Cover and Joy Thomas. *Elements of Information The-
           ory.* Wiley Series in Telecommunication. Wiley & Sons, 1991.

[DEFvZ92] P. C. Dubois, Diane Evans, Anthony Freeman, and Jacob van
           Zyl. Approach to derivation of sir-c science requirements for
           calibration. *IEEE Transactions on Geoscience and Remote
           Sensing*, 30:1145 − 1149, 1992.

[DGdGLS94] Gianfranco De Grandi, Hugo de Groof, Carlo Lavalle, and
           Alois J. Sieber. Fully polarimetric classification of the Black
           Forest MAESTRO 1 AIRSAR data. *In. J. Remote Sensing*,
           15:2755 − 2775, 1994.

[Dob95]   M. C. Dobson *et al.* Estimation of forest biomass character-
           istics in Northern Michigan with SIR-C/X-SAR data. *IEEE
           Transactions on Geoscience and Remote Sensing*, 33:877 − 894,
           1995.

[Eva88]   Diane Evans *et al.* Radar polarimetry: Analysis tools and
           applications. *IEEE Transactions on Geoscience and Remote
           Sensing*, 26(6):774 − 789, 1988.

[Eva93]   Diane Evans *et al.* The shuttle imaging radar-C and X-band
           synthetic aperture radar (SIR-C/X-SAR) mission,. *Eos Trans-
           actions*, 74(13), 1993.

[EvZ90]   Diane Evans and Jacob van Zyl. Polarimetric imaging radar:
           Analysis tools and applications. In Jin Au Kong, editor, *Radar
           Polarimetry*, volume 3. Elsevier Science Publishing, 1990.

[FMY94]   G. Foody, M. McCulloch, and W. Yates. Crop classification
           from C-band polarimetric radar data. *Int. J. Remote Sensing*,
           15:2871 − 2885, 1994.

[For98]   Joaquim Fortuny. An efficient 3-D near-field ISAR algo-
           rithm. *IEEE Transactions on Aerospace and Electronic Sys-
           tems*, 34(4):1261 − 1270, October 1998.

[FPL98]   Ann Franchois, Yolanda Piñero, and Roger Lang. Complex permittivity measurements of two conifers. *IEEE Transactions on Geoscience and Remote Sensing*, 36, September 1998.

[Fre92a]   Anthony Freeman. SAR calibration: An overview. *IEEE Transactions on Geoscience and Remote Sensing*, 30(6):1107 − 1121, 1992.

[Fre92b]   Anthony Freeman *et al.* Calibration of stokes and scattering matrix format polarimetric SAR data. *IEEE Transactions on Geoscience and Remote Sensing*, 30(3), 1992.

[FS94]   Joaquim Fortuny and Alois J. Sieber. Fast algorithm for a near-field synthetic aperture radar processor. *IEEE Transactions Antennas Propagation*, 42:1458 − 1460, 1994.

[FS99]   Joaquim Fortuny and Alois J. Sieber. Three-dimensional synthetic aperture radar imaging of a fir tree: first results. *IEEE Transactions on Geoscience and Remote Sensing*, 37(2):1006 − 1014, March 1999. Part 2.

[Fun94]   Adrian Fung. *Microwave Scattering and Emission Models and their Applications*. Artech House, 1994.

[Ger99]   Anne-Laure Germond. *Théorie de la polarimétrie radar en bistatique*. PhD thesis, IRESTE, Université de Nantes, 1999.

[Gil58]   E. Gilbert. Gray codes and the paths on the n-cube. *Bell System Technical Journal*, 37:815 − 826, May 1958.

[GKV89]   C. Gerthsen, H. Kneser, and H. Vogel. *Physik*. Springer, 16 edition, 1989.

[Gne62]   B. Gnedenko. *Lehrbuch der Wahrscheinlichkeitsrechnung*. Akademie-Verlag Berlin, 3 edition, 1962.

[Gol81]   Leslie Goldschlager. Short algorithms for space-filling curves. *Software - Practice and Experience*, 11:99 − 100, 1981.

[GR82]   G. Graf and B. Röde. Radar scattering from a solitary fir tree. In *IGARSS Proceedings*, 1982.

[Gri77]   Ulrich Grigull. *Technische Thermodynamik.* Walter de Gruyter, 3 edition, 1977.

[Gri86]   J. G. Griffiths. An algorithm for displaying a class of space-filling curves. *Software Practice and Experience*, 16(5):403 – 411, May 1986.

[Hil91]   David Hilbert. Über stetige Abbildungen einer Linie auf ein Flächenstück. *Math. Annln,*, 38:459 – 460, 1891.

[Hir87]   H. Hirosawa*, et al.* Measurement of backscatter from conifers in the C and X bands. *International Journal of Remote Sensing*, 11(8):1687 – 1694, 1987.

[HMK89]   H. Hirosawa, Y. Matsuzaka, and O. Kobayashi. Measurement of microwave backscatter from cypress with and without leaves. *IEEE Transactions on Geoscience and Remote Sensing*, 27:698 – 701, November 1989.

[Hor96]   Ralf Horn. The DLR airborne SAR project E-SAR. http://www.dlr.de/ne-hf/projects/ESAR/, July 1996.

[Huy70]   Jean Richard Huynen. *Phenomenological Theory of Radar Targets.* PhD thesis, Technische Hogeschool Delft, 1970.

[IEE90]   IEEE. Standard 686 - 1990, 1990.

[Käh92]   Daniel Kähny. *Modellierung und meßtechnische Verifikation polarimetrischer, mono- und bistatischer Radarsignaturen und deren Klassifizierung.* PhD thesis, Universität Karlsruhe, 1992.

[KF89]   M. A. Karam and Adrian K. Fung. Leaf-shape effects in electromagnetic wave scattering from vegetation. *IEEE Transactions on Geoscience and Remote Sensing*, 27:687 – 697, November 1989.

[KK92]   K. Kammeyer and Kristian Kroschel. *Digitale Signalverar-beitung.* Teubner, 2 edition, 1992.

[Kla89]   Helmut Klausing. *Realisierbarkeit eines Radars mit synthetis-cher Apertur durch rotierende Antennen.* PhD thesis, Univer-sität Karlsruhe, 1989.

[KMB59]   J. Keilson, N. Mermin, and P. Bello. A theorem on cross cor-relation between noisy channels. *IRE Transactions on Infor-mation Theory*, pages 77 – 79, June 1959.

[Kon86]   Jin Au Kong. *Electromagnetic Wave Theory.* Wiley & Sons, 1986.

[Kro86]   Kristian Kroschel. *Statistische Nachrichtentechnik: Sig-nalerkennung und Parameterschätzung*, volume 1. Springer, 2 edition, 1986.

[Kro88a]   Heinz Kronmüller. *Methoden der Meßtechnik.* Schnäker, 3 edition, 1988.

[Kro88b]   Kristian Kroschel. *Statistische Nachrichtentechnik: Signal-schätzung*, volume 2. Springer, 2 edition, 1988.

[Kro91]   Kristian Kroschel. *Datenübertragung.* Springer, 1991.

[Kro93]   Ernst Krogager. *Aspects of Polarimetric Radar Imaging.* PhD thesis, Danmarks Tekniske Højskole, 1993.

[LS98]   Juan Manuel López Sánchez, *et al.* Validation of the backscat-tered frequency correlation function for the inversion of bio-physical parameters from natural targets. In *IGARSS Pro-ceedings*, volume 5, pages 2390 – 2391, 1998.

[LSFSC98]   Juan Manuel López Sánchez, Joaquim Fortuny, Alois J. Sieber, and Shane Cloude. Esperimental validation of an entropy-based classification scheme using a wide-band polarimetric radar. In Ann Franchois, editor, *Proceedings of the PIERS Workshop on Advances in Radar Methods*, EUR Report 18662 EN, pages 208 – 210, July 1998.

[Luk98]   Konstantin Lukin. Advanced noise radar technology. In Ann
            Franchois, editor, *Proceedings of the PIERS Workshop on Ad-
            vances in Radar Methods*, EUR Report 18662 EN, pages 137 –
            140, July 1998.

[LZ86]   Abraham Lempel and Jacob Ziv.   Compression of two-
            dimensional data. *IEEE Transactions on Information Theory*,
            IT-32(1):2 – 8, January 1986.

[Mac98]   David MacKay. Information theory, pattern recognition and
            neural networks.
            http://wol.ra.phy.cam.ac.uk/mackay/itprnn/, 1998.

[Mac99]   David MacKay. Information theory, inference and learning al-
            gorithms.
            http://wol.ra.phy.cam.ac.uk/mackay/itprnn/book.d.ps.gz,
            1999.

[Max54]   James Clerk Maxwell. *A treatise on electricity and magnetism*,
            volume 1 - 2. Dover, 3 edition, 1954.

[Men91]   Dean Mensa. *High Resolution Radar Cross Section Imaging*.
            Artech House, 2 edition, 1991.

[Mly91]   Dieter Mlynski. Skriptum zur Vorlesung: Elektrodynamik.
            Universität Karlsruhe, 1991.

[MT98]   Mahta Moghaddam and Robert Treuhaft. Limitations in the
            number of parameters estimated with polarimetric interferome-
            try. In Ann Franchois, editor, *Proceedings of the PIERS Work-
            shop on Advances in Radar Methods*, EUR Report 18662 EN,
            pages 163 – 165, July 1998.

[Nes94]   Giuseppe Nesti, *et al.* Recent advances at the european mi-
            crowave signature laboratory. *SPIE Proceedings, Microwave
            Instrumentation and Satellite Photogrammetry for Remote
            Sensing of the Earth*, 2315:56 – 67, September 1994.

[NP92]   Marco Negretto and Luisa Portoni. Esperimenti con alcune
            tecniche di compressione di immagini angiocardiografiche sec-
            ondo il cammino di Peano-Hilbert. Master's thesis, Politecnico
            di Milano, 1992.

[NYKL92]   S. V. Nghiem, S. H. Yueh, R. Kwok, and F. K. Li. Symme-
            try properties in polarimetric remote sensing. *Radio Science*,
            27(5):693 – 710, 1992.

[Oly98]   Frank Olyslager, *et al.* Techniques based on the wideband time
            response to detect anti-personnel mines. In Ann Franchois,
            editor, *Proceedings of the PIERS Workshop on Advances in
            Radar Methods*, EUR Report 18662 EN, pages 177 – 179, July
            1998.

[PAB68]   Edward Patrick, Douglas Anderson, and F. K. Bechtel.
            Mapping multidimensional space to one dimension for com-
            puter output display. *IEEE Transactions on Computers*, C-
            17(10):949 – 953, October 1968.

[Pap91]   A. Papoulis. *Probability, Random Variables and Stochastic
            Processes*. Mc Graw Hill, 3 edition, 1991.

[Pap98]   K. P. Papathanassiou *et al.* Airborne polarimetric SAR in-
            terferometry. In *Proceedings of IGARSS '98*, volume 4, pages
            1901 – 1903, 1998.

[Pea90]   Giuseppe Peano. Sur une courbe, qui remplit toute une aire
            plaine. *Math. Annln.*, 36:157 – 160, 1890.

[PJS92]   Heinz-Otto Peitgen, Hartmut Jürgens, and Dietmar Saupe.
            Chaos and Fractals, New Frontiers of Science. Springer, 1992.

[Pot95]   Eric Pottier. Fondements mathématiques de la polarimétrie
            radar. IRESTE Université de Nantes, 1995.

[Pri98]   Corinna Prietzsch. *Vergleichende Analyse von SAR-Daten für
            die Regionalisierung des Wassergehalts im Oberboden*. PhD
            thesis, Universität Potsdam, 1998.

[PTVF92]   W. Press, S. Teukolsky, W. Vertterling, and B. Flannery. *Numerical Recipes in C: The Art of Scientific Computing*. Cambridge University Press, 2 edition, 1992.

[RBSK70]   T. Ruck, E. Barrick, D. Stuart, and K. Krichbaum. *Radar Cross Section Handbook*. Plenium Press, 1970.

[RNF95]   H. Rott, T. Nagler, and Floricioiu. Snow and glacier parameters derived from single channel and multiparameter SAR. In *Proc. Symposium on Retrieval of Bio- and Geophysical Parameters from SAR Data for Land Applications, Toulouse*, pages 479 − 488, 1995.

[Ros96]   Friedhelm Rostan. *Dual polarisierte Microstrip-Patch-Arrays für zukünftige satellitengestützte SAR-Systeme*. PhD thesis, Universität Karlsruhe, 1996.

[RS94]   J. Ranson and G. Sun. Northern forest classification using temporal multifrequency and multipolarimetric SAR images. *Remote Sensing Environment*, 47:142 − 153, 1994.

[RT99]   Hans Rudolf and Dario Tarchi. LISA - the linear SAR instrument. Technical Note No. I.99.126, Joint Research Centre, 1999.

[RTS97]   Hans Rudolf, Dario Tarchi, and Alois J. Sieber. Combination of linear and circular SAR for 3-D features. In *International Geoscience and Remote Sensing Symposium, IGARSS ´97*, volume 4, pages 1551 − 1553. IEEE, August 1997.

[Rud98]   Hans Rudolf. RoCoCo: Data analysis for the low band monostatic data. Technical Note No. I.98.74, Joint Research Centre, 1998.

[Rud99a]   Hans Rudolf, *et al.* A mobile and versatile SAR system. In *IGARSS Proceedings*, volume I, pages 592 − 594, 1999.

[Rud99b] Hans Rudolf, *et al.* A parallelogram shaped arm for improving circular SARs. In *IGARSS Proceedings*, volume I, pages 553 – 555, 1999.

[RW86] Sebastian Riegger and Werner Wiesbeck. Coherent polarimetric RCS measurements on trees. In *IGARSS Proceedings*, volume SP-254, pages 883 – 887, 1986.

[RW89] Sebastian Riegger and Werner Wiesbeck. Wide-band polarimetry and complex radar cross section signatures. *Proceedings of the IEEE*, 77(5):649 – 658, May 1989.

[RW91] Sebastian Riegger and Werner Wiesbeck. A complete error model for free space polarimetric measurements. *IEEE Transactions on Antennas and Propagation*, 39(8):827 – 844, August 1991.

[Sch98] Robert Schneider. *Modellierung der Wellenausbreitung für ein bildgebendes Kfz-Radar*. PhD thesis, Universität Karlsruhe, 1998.

[SG96] Wolfgang Sauer-Greff. Skriptum zur Vorlesung: Einführung in die Informations- und Codierungstheorie. Universität Kaiserslautern, 1996.

[Sha48] Claude Shannon. A mathematical theory of communication. *The Bell System Technical Journal*, 27(3):379 – 423, July 1948.

[Sha49] Claude Shannon. Communication in the presence of noise. *Proceedings of the I.R.E.*, 37(1):10 – 21, January 1949.

[Sie85] Alois J. Sieber. Forest signatures in imaging and nonimaging microwave scatterometer data. *ESA Jornal*, 9:431 – 448, 1985.

[Sie93] Alois J. Sieber. The european microwave signature laboratory. *EARSel Advances in Remote Sensing*, 2(1):195 – 204, January 1993.

[Sie95]   Alois J. Sieber, editor. *International Workshop and Study on the Knowledge for the Localisation and Identification of Anti-Personnel Mines*, EUR Report 16329 EN, August 1995.

[Sie96]   Alois J. Sieber. Localisation and identification of anti-personnel mines: The JRC study report. In Giuseppe Nesti, editor, *1st EMSL User Workshop Proceedings*, EUR Report 17326 EN, pages 87 − 90, 1996.

[Sie98]   Alois J. Sieber, editor. *Proceedings: Demining Technology - International Exhibition, Workshop and Training Courses*, EUR Report 18682 EN, September 1998.

[Sim89]   K. Simonyi. *Theoretische Elektrotechnik*. VEB Deutscher Verlag der Wissenschaften, 9 edition, 1989.

[Sko81]   Merrill Skolnik. *Introduction to Radar Systems*. Electrical Engineering Series. McGraw-Hill, 2 edition, 1981.

[Smi99]   Steven W. Smith. The scientist and engineer's guide to digital signal processing. http://www.DSPguide.com, 1999.

[Sti83]   George Stimson. *Introduction to Airborne Radar*. Hughes Aircraft Company, 1983.

[Stu93]   Warren Stutzman. *Polarization in Electromagnetic Systems*. Artech House, 1993.

[Tar99]   Dario Tarchi, *et al.* SAR interferometry for structural changes detection: A demonstration test on a dam. In *IGARSS Proceedings*, volume III, pages 1522 − 1524, 1999.

[UE90]   Fawwaz Ulaby and Charles Elachi. *Radar Polarimetry for Geoscience Applications*. Artech House, 1990.

[UF98]   Lars Ulander and P.-O. Frolind. Ultra-wideband SAR interferometry. *IEEE Transactions on Geoscience and Remote Sensing*, 36(5):1540–1550, September 1998.

[UMF81]   Fawwaz Ulaby, R. Moore, and Adrian Fung. *Microwave Remote Sensing: Microwave Remote Sensing Fundamentals and Radiometry*, volume 1. Artech House, 1981.

[UMF82]   Fawwaz Ulaby, R. Moore, and Adrian Fung. *Microwave Remote Sensing: Radar Remote Sensing and Surface Scattering and Emission Theory*, volume 2. Artech House, 1982.

[UMF86]   Fawwaz Ulaby, R. Moore, and Adrian Fung. *Microwave Remote Sensing: From Theory to Applications*, volume 3. Artech House, 1986.

[vdH57]   H. C. van de Hulst. *Light Scattering by Small Particles*. Dover, 1957.

[vZ90]   Jacob van Zyl. Calibration of polarimetric radar images using only image parameters and trihedral corner reflector responses. *IEEE Transactions on Geoscience and Remote Sensing*, 28(3):337 – 348, 1990.

[vZZ90]   Jakob van Zyl and Howard Zebker. Imaging radar polarimetry. In Jin Au Kong, editor, *Radar Polarimetry*, volume 3 of *Progress in Electromagnetic Research*. Elsevier Science Publishing, 1990.

[vZZ91]   Jakob van Zyl and Howard Zebker. Imaging radar polarimetry: A review. *Proceedings of the IEEE*, 79:1583 – 1606, 1991.

[Wan88]   Gerd Wanielik. *Signaturuntersuchungen an einem polarimetrischen Pulsradar*. PhD thesis, Universität Karlsruhe, 1988.

[Wen89]   Siegfried Wendt. *Nichtphysikalische Grundlagen der Informationstechnik*. Springer, 1989.

[Wie90]   Werner Wiesbeck. Skriptum zur Vorlesung: Hochfrequenztechnik I. Universität Karlsruhe, 1990.

[Wie92]   Werner Wiesbeck. Skriptum zur Vorlesung: Hochfrequenztechnik II. Universität Karlsruhe, 1992.

[WK91]   Werner Wiesbeck and Daniel Kähny. Single reference three tar-
           get calibration and error correction for monostatic polarimetric
           free space measurements. *Proceedings of the IEEE*, 79:1551 –
           1558, October 1991.

[WM91]   Geoff Wyvill and Craig McNaughton. *Scientific Visualiza-
           tion of Physical Phenomena*, chapter Three Plus Five Makes
           Eight: A Simplified Approach to Halftoning, pages 379 – 392.
           Springer, 1991. This book contains the Proceedings of the
           9th International Conference of Computer Graphics Society,
           CG International '91, June 26-28, 1991, Cambridge, Mas-
           sachusetts.

[Woo53]   P. M. Woodward. *Probability and Information Theory, with
           Applications to Radar*. Pergamon Press, 1953.

[Woo75]   Michael Woodroof. *Probability with Applications*. McGraw
           Hill, 1975.

[WW83]   Ian Witten and Brian Wyvill. On the generation and use of
           space-filling curves. *Software Practice and Experience*, pages
           519 – 525, 1983.

[Zeb91]   Howard Zebker *et al.* Calibrated imaging radar polarimetry:
           Technique, examples, and applications. *IEEE Transactions on
           Geoscience and Remote Sensing*, 29(6):942 – 961, 1991.

Index

anisotropy, 12

calibration, 44, 71
coherence matrix, 12, 68, 99

data processing inequality theorem, 16

entropy, 14
    chain rule, 15, 16, 30
    Cloude, 12
    conditional, 14, 30
    joint, 14
    scattering matrix, 27, 30, 32, 38, 40, 42

gain
    polarimetric, 31, 32, 37, 40, 41, 64, 73, 77, 84, 86, 91

Hilbert-curve, 33, 34, 66

information
    mutual, 15, 29
    polarimetric, 31

Jones-vector, 8, 9

Mueller-matrix, 11

Peano-Hilbert-curve, *see* Hilbert-curve
Poincaré-sphere, 9, 101, 103

polarisation ellipse, 9

radar
    cross-range resolution, 20, 52, 54, 56
    cross-range unambiguity, 22, 56
    equation, 17, 51
    range resolution, 19, 50
    range unambiguity, 20
RCS matrix
    sphere, 36
reciprocity theorem, 28–30

scattering coefficient
    differential, 18
scattering matrix, 11, 101
    dihedral, 38
Stokes-vector, 9, 99
synthetic aperture
    circular, 55, 71
    linear, 53, 71

wave equation, 7

Curriculum Vitae

Date of birth:	December 13th, 1968
Place of birth:	Bochum / Germany
Marital status:	single
Nationality:	German

Education

1975 - 1979	Carl-Zuckmayer primary school Mainz
1979 - 1988	Rabanus-Maurus grammar school Mainz

Military duty

1988 - 1989	basic military service in Hammelburg and Mainz

University

1989 - 1991	University of Kaiserslautern
	electrical and electronic engineering
1991 - 1994	University of Karlsruhe
	electrical and electronic engineering
	with emphasis on radio frequency techniques

Professional life

1995 - 1996	Daimler-Benz Research and Technology
1996 - 1999	grant of the Joint Research Centre
	of the European Commission in Ispra (Italy)
	Space Applications Institute
since 1999	Siemens Information and Communications Mobile